DISSERTATION ZUR ERLANGUNG DES
DOKTORGRADES DER FAKULTÄT FÜR CHEMIE UND
PHARMAZIE DER
LUDWIG-MAXIMILIANS-UNIVERSITÄT MÜNCHEN

Measurement and Analysis of the First Assembly Steps in Protein Polymerization

---

Maria HOYER

geboren in

Berlin, Deutschland

2021

Erklärung

Diese Dissertation wurde im Sinne von §7 der Promotionsordnung vom 28. November 2011 von Herrn Prof. Don C. Lamb, Ph.D., betreut.

Eidesstattliche Versicherung

Diese Dissertation wurde eigenständig und ohne unerlaubte Hilfe erarbeitet.

München, 22.11.2021 Maria Hoyer

Dissertation eingereicht am:	31.03.2021
1. Gutachter:	Prof. Don C. Lamb, Ph.D.
2. Gutachter:	Prof. Dr. Philip Tinnefeld
Mündliche Prüfung am:	30.04.2021

Abstract

Measurement and Analysis of the First Assembly Steps in Protein Polymerization

by Maria HOYER

Proteins play a crucial role throughout all phyla of life. Many proteins build long filamentous structures by assembling many globular single proteins, the monomers. This process is both associated with physiological functions in the organism and with pathological malfunctions, resulting in disease. Although filament elongation has been extensively studied, the mechanism of filament nucleation remains often unclear. High background from the micromolar concentrations needed for filament formation have prevented direct observation of the nucleation dynamics using microscopy or spectroscopy methods. To directly monitor the early steps of filament assembly, I have used the attoliter excitation volume of zero-mode waveguides (ZMW). Thereby, a tethering protein on the bottom of the ZMW is used to bind the monomers, which start assembling after the start of the measurement. The resulting data is presented as a step-wise increase in intensity over time, each step indicating the binding of a monomer.

Now that it is possible to obtain step-wise, single-filament data, adequate analysis methods need to be developed. Here, I present two new analysis methods for single-filament data, the visitation analysis and the average rate analysis. These methods, as well as the classic dwell-time analysis often used for the analysis of microscopic association and dissociation rates, have been tested and compared using simulations of filament nucleation. Furthermore, the limitations of each analysis method have been explored along the lines of the signal-to-noise ratio, the sampling rate, the labeling efficiency and the photobleaching rate of the fluorescent dyes used in single-molecule fluorescence experiments. The results of these simulations allow one to analyze and interpret single-filament data in a meaningful way and to plan the experimental conditions according to the kinetics and maximum labeling efficiency of the assembling protein of interest.

The developed analysis methods have been applied to experimental data of actin nucleation. Using single tethering proteins attached to the bottom of the ZMW, the actin filament nucleation process could be visualized using

different actin nucleators. For pointed-end actin growth on gelsolin, two distinct populations depending on the stability of the actin dimer were found, of which only one lead to stable filament elongation. Furthermore, barbed-end actin growth was monitored using the nucleators cappuccino and spire. Whereas cappuccino was found to nucleate efficiently, leading to stable growing oligomers, spire was found to not be sufficient for actin nucleation. Using actin-binding compounds like Latrunculin A, which inhibits the flattening of the actin monomers occurring during filament formation, flattening was determined to be a key requirement for the formation of stable elongating filaments. Miuraenamide A, another actin-binding compound was found to stabilize oligomers and reduce the critical concentration needed for filament formation.

Contents

Chapter 1

Introduction

Across all biological organisms, proteins are not only used for their ability to catalyze reactions in a remarkable efficient and flexible way, but also as scaffolding material for stability, motility and transport. Individual globular proteins assemble to larger structures spanning several orders of magnitude in size, ranging from small oligomers in the nm range to several μm-long filaments. The assembly and disassembly of these structures is highly regulated by associated proteins and *vice versa*, the state of the filament structure has an effect on important decisions in the cell (Lee and Dominguez, 2010). While protein polymerization is indispensable for the organization of living organisms, it is also associated with pathological processes. For example, the aggregation of misfolded proteins is associated with Alzheimer's disease or type II diabetes mellitus (Knowles, Vendruscolo, and Dobson, 2014).

The vital importance of the cytoskeleton and its association with disease, along with the emerging field of nanobiotechnology, where self-assembling proteins or DNA are being used to structure materials (Kuzyk, Laitinen, and Törmä, 2009), has increased the interest in the mechanisms of protein self-assembly over the past two decades. While the structure of the monomeric proteins as well as the assembled filaments is typically known, the conformations and kinetics of the oligomers is more challenging to study due to the ever-changing nature of the system.

Over the past decade, more and more proteins were shown to form oligomers or even filaments (Dick et al., 2016 Lu et al., 2014). The assembly mechanism, however, is not fully understood for most proteins. This is, in part, due to the challenging biochemical handling of many of these proteins, but also due to the lack of appropriate experimental methods that enable the observation of the assembly process on a single-molecule level. The assembly process often

involves the formation of many different oligomers that grow and shrink dynamically and even undergo conformational changes (Kelly, 1998). Much progress has been made using kinetic analysis of bulk methods (Michaels et al., 2017; Grazi, Ferri, and Cino, 1983), however, the details of these processes cannot be elucidated via bulk measurements due to the many different species involved. Therefore, efforts have been made to study oligomerization processes in smaller volumes (Horrocks et al., 2015) and even on the single molecule level (Horrocks et al., 2016; Andrecka et al., 2016).

Single molecule techniques provide direct, real-time measurements of single monomer association and dissociation events during oligomerization (Andrecka et al., 2016; Hoyer et al., 2018). In this thesis, single molecule fluorescence techniques have been combined with zero-mode waveguides (ZMW) (Levene et al., 2003) to directly observe the first steps during oligomer assembly of actin (Hoyer et al., 2018). Through their nanostructure, ZMW create thousands of individual measurement volumes in the attoliter range. The extremely small volume allows for concentrations of labeled proteins in the μm-range while keeping single-molecule sensitivity. Thus, ZMW provide the possibility to extend the reach of single molecule fluorescence microscopy techniques towards the high concentrations of labeled protein needed for successfull polymerization (Samiee et al., 2005). Independently, a scattering technique was developed that can measure individual binding and dissociation events of unlabeled monomers (Young et al., 2018). In both cases, a single monomer or a nucleator protein is biochemically bound at the surface and the signal of the binding monomers diffusing in from the surrounding solution is detected.

Another possibility to obtain information about the early stages of the assembly process is to use the average information of many oligomers attached to surface-bound nucleator proteins. This provides the possibility to synchronize the starting point of the oligomerization process and thereby reduce the complexity of the data in comparison to conventional bulk techniques, where a multitude of different oligomers in different conformations occur at the same time. This type of data can be obtained, for example, by using total-internal reflection microscopy (TIRFM) (Liang, Lynn, and Berland, 2009), circular dichroism (Uratani, Asakura, and Imahori, 1972) or other spectroscopy methods (Kirkitadze, Condron, and Teplow, 2001 Zhai et al., 2012 Ramachandran et al., 2014). Only filaments growing on the nucleator protein of interest

are measured, excluding spontaneous oligomerization events occurring in solution.

New methods provide a new type of data. Therefore, it is necessary to test existing analysis tools for their applicability or to develop new analysis tools that can extract the information hidden in the data. It is essential to chose the analysis and the experimental design according to the question of interest. For example, single-molecule data of oligomer assembly provide, in theory, the microscopic kinetic rates of all assembly and disassembly steps, i.e. the complete information about the assembly mechanism. Extracting these rates is a nontrivial task and the classic waiting time analysis used in many applications (Floyd, Harrison, and van Oijen, 2010) has to be evaluated carefully, as will be shown in this thesis. Therefore, for the question about the microscopic assembly mechanisms involved, I developed analysis tools to provide more reliable data by not using the microscopic rates, but by looking at the distribution of oligomer sizes over time.

In this thesis, I measured the assembly of fluorescently labeled actin monomers using ZMW and TIRFM. In ZMW measurements, monomer binding events correspond to a step-wise increase of the intensity of the signal over time, and dissociation events manifest themselves as downward steps. In my master thesis (Hoyer, 2014), I tested different step-finding algorithms for the reliable extraction of these upward and downward steps from the noise-overlaid signal. In this thesis, I further improved the experimental protocol and developed and tested analysis tools that reveal the assembly mechanism hidden in the measured up and down steps of the intensity traces and are at the same time robust towards the experimental complexities like the signal to noise ratio (SNR) or the sampling time. For fluorescently labeled samples, also the labeling efficiency and photobleaching has to be taken into account.

By applying the developed analysis tools as well as the classical dwell time analysis to experimental data of actin growing in ZMW or on a plane surface using total internal reflection microscopy (TIRFM), I was able to obtain new insights regarding actin assembly. I measured actin growing on the nucleator proteins gelsolin, cappuccino and spire, thereby covering different classes of actin nucleators. Additionally, I used the actin binding compounds Latrunculin A (LatA) and Miuraenamide A (MiuA) to gain information on the conformational change occurring during actin assembly in the case of LatA

and to elucidate the effect of MiuA on actin oligomerization. For the measurements with MiuA, confocal microscopy was used as a solution-based method in combination with fluorescence correlation spectroscopy (FCS) and a spike analysis to quantify the occurrence of large oligomers.

In this thesis, I will first give an overview of the involved principles and methods regarding the employed fluorescence techniques and the biological principles of protein assembly, in particular actin nucleation and polymerization. Then, the developed analysis methods and simulations of protein oligomerization will be described, followed by a description of the performance and applicability of the analysis methods under varying conditions. The last chapter is dedicated to the experimental measurements of actin oligomerization using ZMW, TIRFM and confocal microscopy.

Chapter 2

Principles and Methods

2.1 The Principle of Fluorescence

Fluorescence was beginning to interest modern scientists in the middle of the 19^{th} century (Herschel, 1845; Stokes, 1852). Like other forms of luminescence, it occurs when molecules in an electronically excited state emit photons upon relaxation into the ground state. Depending on the nature of the excited state, either fluorescence with lifetimes on the nanosecond range or the much slower phosphorescence with lifetimes in the order of milliseconds to seconds occurs. Fluorescence is much faster than phosphorescence because of the spin orientation of the excited state. In the case of phosphorescence, the spin of the triplet excited state is in a parallel orientation to the singlet ground state. That causes the transition to the ground state to be forbidden, following the quantum mechanical selection rules that forbid singlet-triplet transitions.

One of the main feature of fluorescence is the Stokes shift. It describes the spectral shift between the excitation light and the fluorescence emission, a phenomenon that is exploited to separate the fluorescent signal of fluorophores from the exciting light in every fluorescence microscope. The Stokes shift can be explained by looking at a representation of the electronic states of fluorophores (Fig. 2.1). When a photon with the appropriate energy is absorbed, the fluorophore is excited from the singlet ground state S_0 to an excited state S_1. Part of the energy is absorbed into vibrations of the molecule via internal conversion, bringing the system to the lowest S_1 state in a few picoseconds (Lakowicz, 2006). Internal conversion is the cause for the fact that the emission spectrum is independent of the excitation wavelength for most dyes, known as "Kasha's rule" (Kasha, 1950, Vavilov 1926). Upon relaxation back to an excited vibrational state in the S_0 state, a photon of less energy is released,

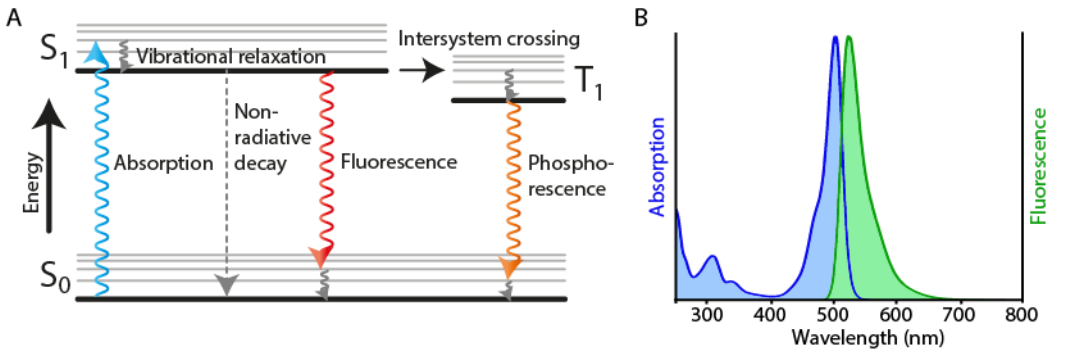

FIGURE 2.1: A: Jablonski diagram showing various processes that occur during fluorescence. Absorption of a photon excites the system to an excited state of the S_1 state. After vibrational and rotational relaxation, either a non-radiative decay process, fluorescence or intersystem crossing to the T_1 state can occur. From the T_1 state, phosphorescence leads to the relaxation to the ground state. All transition are vertical because the transitions are in the femtosecond range and the nuclei do not change position in this time (Born-Oppenheimer approximation). B: absorption and fluorescence emission spectrum of the fluorescent dye atto488.

thus leading to a red-shift in the fluorescence spectrum. Because electronic excitations do not have much effect on the nuclear geometry, the spacings of the vibrational states are similar in the S_0 and in the S_1 state, leading to a similarity of the excitation and emission spectra, the "mirror effect" (Fig. 2.1 B).

In addition to relaxation via photon emission, the system can also transfer the energy into non-radiative decay processes or can enter the T_1 state during intersystem crossing. The slow, because quantum mechanically forbidden transition from the T_1 to the S_0 state causes phosphorescence.

Fluorescent dyes are constantly evolving for tailor-made uses in fluorescence applications. Besides spectral and biological considerations, three main characteristics are the extinction coefficient ϵ, the fluorescence lifetime τ and the quantum yield Q, which describes the relation between the number of emitted photons and the number of absorbed photons, which is the probability of emitting a fluorescence photon after excitation. The fluorescence lifetime is defined as the time the molecule stays in the excited state prior to transitioning to the ground state. For the description of the quantum yield, we look at the intrinsic rate constant for fluorescence emission k_{fl} and the rate of all other decay processes k_{nr}:

$$Q = \frac{k_{fl}}{k_{fl} + k_{nr}} \tag{2.1}$$

The proportion of decay via fluorescence with respect to all other decay processes describe the quantum yield. Together with the extinction coefficient, the quantum yield is a measure for the brightness of the fluorophore. The extinction coefficient describes the ability of the fluorophore to absorb light and transition into the excited state. Via the Lambert-Beer law, the extinction coefficient is often used to determine the concentration of the fluorophore or the labeled species:

$$A = \epsilon \cdot c \cdot l \tag{2.2}$$

where c is the concentration of the fluorophore, l is the length of the light traveling in the solution and A is the absorbance, which describes the fraction of the intensity of the light that was absorbed by the fluorophore.

Finally, the measured lifetime is defined as the inverse of the decay rates:

$$\tau = \frac{1}{k_{fl} + k_{nr}} \tag{2.3}$$

Hence, the measured lifetime is also influenced by other processes like quenching or energy transfer and not necessarily related to the intrinsic fluorescence lifetime.

2.2 Fluorescence Microscopy

Fluorescence methods have become widely used in microscopy imaging in the last three decades. The ability to specifically label biomolecules with fluorescent proteins or organic dyes has allowed biological and medical researchers to identify cellular pathways on the single-cell level as well as in larger cellular structures. By using fluorescence methods with the ability to detect single molecules like total-internal reflection microscopy (TIRFM) for surface-immobilized molecules, or confocal microscopy for freely diffusing molecules, even the conformational changes of individual proteins can be elucidated. In the search of ever better, clearer images with enhanced signal and reduced background, a multitude of excitation and detection techniques has been developed.

A universally used feature is the separation of excitation light and fluorescence by a dichroic mirror, whose transmission is dependent on the wavelength of light. As light sources, lasers have become widely used because of their emission wavelength profile and the practicability of a collimated beam like the possibility to couple it into a single-mode fiber, which produces a clean beam profile. For detection, electron-multiplied charge coupled devices (EMCCDs) or more recently, scientific complementary metal–oxide–semiconductor (sCMOS) have become widely used for image-based detection, or avalanche photo diodes (APDs) for confocal detection.

2.2.1 Fluorescent probes for Fluorescence Microscopy

For investigating nonfluorescent biological samples in a fluorescence microscope, the samples of interest have to be labeled with a fluorescent dye. There are several options spanning from fluorescent proteins like the green-fluorescent protein (GFP) over quantum dots to organic dyes. For the labeling of proteins and DNA for single-molecule applications, mostly organic dyes are used due to their smaller size and increased brightness and photostability compared to fluorescent proteins. For the attachment to the proteins or DNA, different labeling strategies have been developed using mostly covalent bonds to specific amino acids inside the proteins. A typical labeling strategy is to target cysteins in the proteins with maleimide groups attached to the fluorophore (Toseland, 2013). Targeting cysteins has the advantage that, due to its low abundance, it results in a high site-specificity of the labeling. Another possibility is to target the amine groups of lysines or the N-terminus, in which case succinimidyl-esters or isothiocyanates can be used.

Depending on the labeling strategy, the result can be a specifically labeled protein, where each protein has zero or one dye molecule attached, or a stochastically labeled protein, where more than one label can be attached to the same protein. Stochastic labeling results in a Poisson distribution of dye molecules per protein, according to $P(k) = e^{-\lambda}\lambda^k/k!$, where k is the number of dyes per protein and λ is the average number of fluorophores per protein or the labeling efficiency.

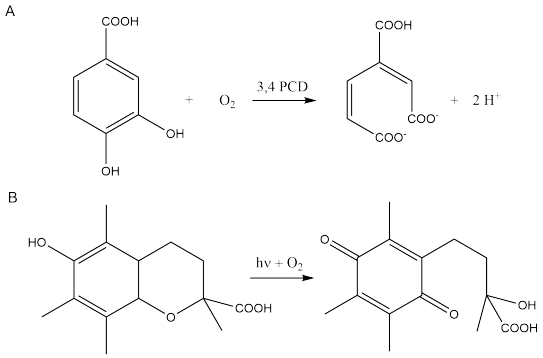

FIGURE 2.2: A: PCA oxidation catalyzed by PCD reduces free oxygen in the solution. B: Trolox activation to trolox-quinone through UV-light.

2.2.2 Reduction of Blinking and Photobleaching

For the use of fluorescent probes for single-molecule applications, the requirements of fluorescent dyes are increasing. The measurable fluorescence signal should occur in the seconds to minute timescale and be as stable as possible in terms of blinking and photobleaching. Blinking describes fast intensity fluctuations in the millisecond range. During blinking or photobleaching, the molecule enters a dark state transiently or permanently, respectively. These dark states or their precursors could be triplet states, conformational isomers or radical ions (Aitken, Marshall, and Puglisi, 2008). Upon entering dark states, molecular oxygen present in aqueous solutions plays a major role. Triplet oxygen reacts efficiently with the triplet states of dyes. Thereby, the triplet states get quenched and singlet oxygen is formed, which is much more reactive and oxidizes the dye rapidly, leading to permanent photobleaching and impairing fluorescence. Thus, while blinking is prevented due to triplet state quenching, photobleaching is enhanced by the presence of dissolved oxygen. Therefore, oxygen scavanging systems are used to decrease the concentration of dissolved oxygen. This leads to longer lived triplet states, and hence, more blinking. To prevent blinking, chemical additives are added to the solution.

The oxygen scavanging system that proved best for the experiments in this thesis is the combination of protocatechuic acid (PCA) and protocatechuate-3,4-dioxygenase (PCD) (Aitken, Marshall, and Puglisi, 2008). PCD catalyzes the oxidation of PCA using molecular oxygen, thereby decreasing the oxygen concentration (Fig. 2.2 A). To prevent blinking, trolox (6-hydroxy-2,5,7,8-tetramethylchroman-2–carboxylic acid) is added. Photo-activated trolox forms trolox-quinone (Kim et al., 2007) (Fig. 2.2 B). It quenches the triplet state

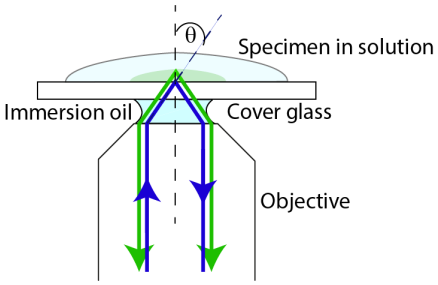

FIGURE 2.3: In objective-type TIRFM, an objective with a high numerical aperture is illuminated off-center to achieve an incidence angle θ above the critical angle for total internal reflection. The fluorescent signal is collected through the same objective and later separated from the excitation light by a dichroic mirror.

via electron transfer and recovers the S_1 state via the complementary redox reaction (Cordes, Vogelsang, and Tinnefeld, 2009; Lambert and Kochevar, 1997).

2.2.3 Total Internal Reflection Microscopy

Total internal reflection microscopy aims to enhance the signal-to-noise ratio (SNR) of labeled molecules close to the surface by decreasing the signal from freely diffusing molecules in the solution. To that aim, only the exponentially decaying evanescent field of the laser beam is used to excite the fluorescent labels, thereby limiting the depth of the excitation volume to about 100 nm to 200 nm along the z-axis. The evanescent field is obtained by tilting the incidence angle of the laser beam onto the cover glass such that total reflection is achieved between the cover glass and the aqueous solution and all propagating modes are reflected. Only the evanescent field penetrates into the solution, exciting fluorescent labels only at or near the surface of the cover glass.

Total internal reflection occurs when light hits the interface between two media with different indices of reflection n_1 and n_2 at or above a critical angle $\theta > \theta_c$ (Fig. 2.3). Thereby, the light has to travel from a medium with higher index of refraction, like a cover glass, to a medium with lower index of refraction, like water or buffer. The critical angle is defined as

$$\theta_c = arcsin(n_1/n_2) \tag{2.4}$$

where n_1 and n_2 are the refractive indices of the liquid and the solid, respectively. For angles above θ_c, the light is reflected back into the solid and only the evanescent field reaches into the liquid phase, whose intensity I(z) decays exponentially in the z-direction according to

$$I(z) = I(0)e^{z/d} \tag{2.5}$$

with

$$d = \frac{\lambda_0}{4\pi} \frac{1}{\sqrt{n_3^2 sin^2\theta - n_1^2}}. \tag{2.6}$$

where λ_0 is the wavelength of the incident light. The penetration depth d depends on the polarization and is on the order of a fraction of λ_0. For the work presented here, the penetration depth is around 100 - 200 nm.

TIRFM can be implemented in two main configurations, prism-type TIRF and objective-type TIRF. Here, objective-type TIRF was used (Fig. 2.3, 2.4). Thereby, a microscope objective with a high numerical aperture (NA) is focused off-axis at the back focal plane to obtain a large angle θ (Fig. 2.3) when hitting the cover glass.

2.2.4 Experimental Setup

In the following, the TIRFM setup is presented that has been used for the described experiments.

The experimental setup has been mainly used with blue (488 nm) or red (642 nm) excitation (Cobolt 06-MLD, Cobolt AB) (Fig. 2.4). In some cases, instead of the blue 488 nm laser, a 561 nm laser (Cobolt 06-DPL, Cobolt AB) has been used. Each laser beam was controlled individually via a shutter (SHB025T, Thorlabs) and coupled into a single-mode fiber (SM450, Thorlabs). After the fiber, a telescope expanded the beam by 10x using a system with two lenses (lens 1: d = 8.0 mm, fl = 10.0 mm, AC080-010-A-ML, Thorlabs, lens 2: d = 25 mm, fl = 100 mm, Thorlabs). By fixing a mirror and a tube lens on a movable stage (grey box in Fig. 2.4), the setup could be used both in TIRF mode and in wide-field mode for ZMW illumination. The light is guided into the objective (60x 1.45 NA oil immersion objective Plan Apo TIRF 60x, Nikon) via a dichroic mirror (zt405/488/561/640rpc, F73-410, AHF Analysentechnik) and onto the specimen, which is excited either in bright

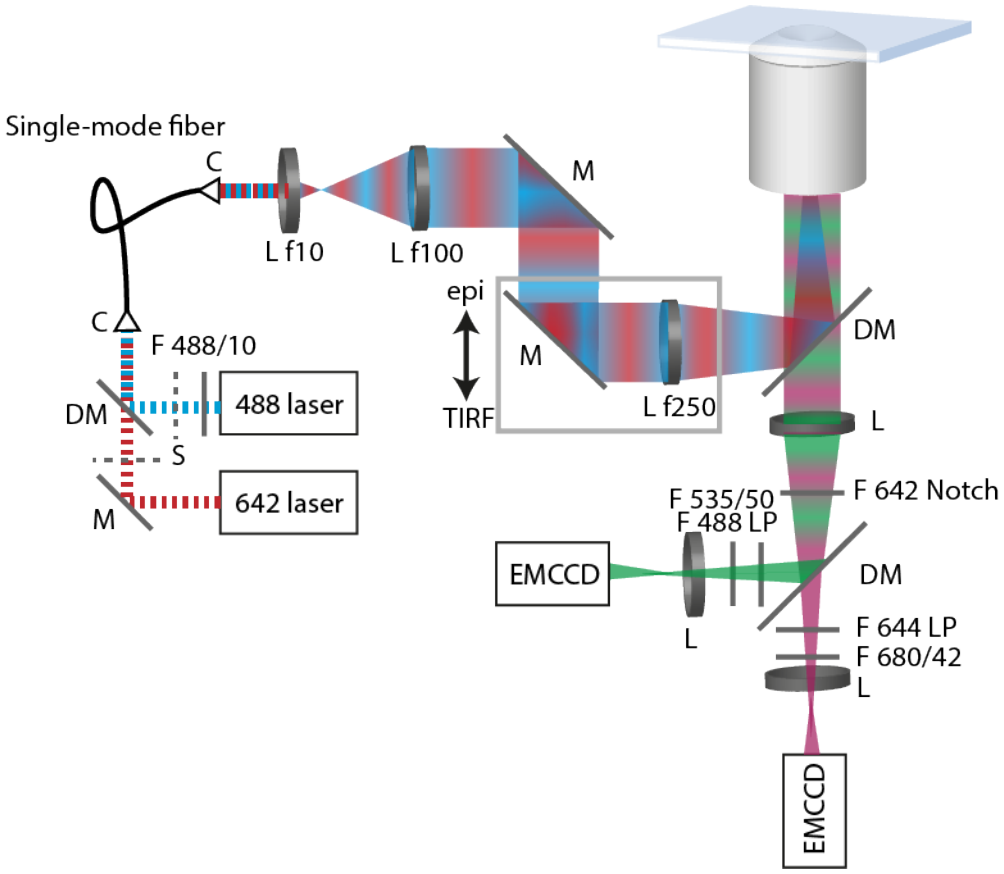

FIGURE 2.4: Schematic of the experimental setup. The grey box indicates a movable stage for switching between conventional bright field and TIRF mode. Abbreviations: M: mirror, DM: dichroic mirror, C: collimator, L: lens, F: filter.

light mode or in TIRF mode. The fluorescence light is then collected by the same objective and transferred through a 642 Notch filter (642 Notch, AHF Analysentechnik) onto a dichroic mirror (FF580-FDi01 as part of the TuCam, Andor Technology) to separate green and red fluorescence. The green fluorescence emission passed through two fluorescence emission filters (535/50 and 488 LP, AHF Analysentechnik) because of the high reflection intensity of the laser light caused by the aluminum surface of the ZMW. Red fluorescence passed through a 680/42 (AHF Analysentechnik) and a 680 LP (AHF Analysentechnik). The signal was recorded by two EMCCD cameras (Andor iXon Ultra 888, Andor Technology) with 1024x1024 pixels per chip.

2.2.5 Slide preparation for TIRFM

For TIRFM, the sample has to be immobilized on the surface of the cover glass. For functionalization of the glass surface and to provide a closed measurement chamber, two different ways of creating a flow chamber on the cover glass

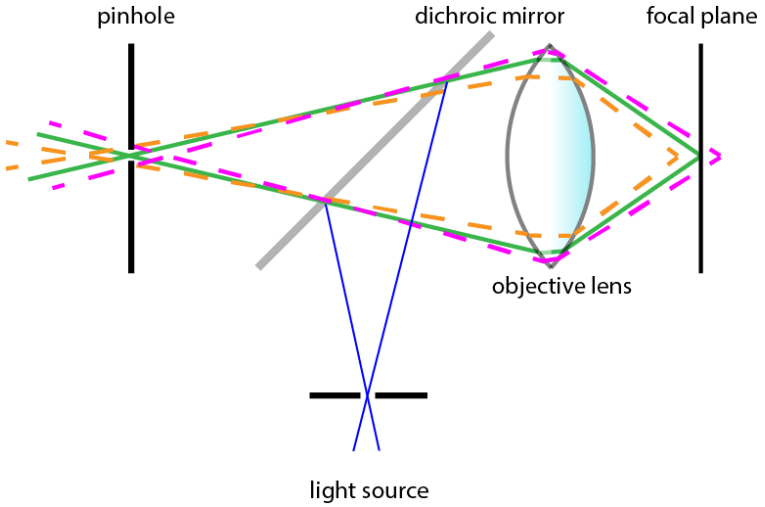

FIGURE 2.5: The principle of confocal microscopy. Light from outside the focal plane is rejected by a pinhole placed in the image plane in front of the detector. In modern confocal microscopes, the light is re-collimated after the pinhole using a lens to include optical filters without disturbing the beam path and then focused again onto the detector.

have been used. For measurements using actin filaments, a microscope slide was heated to 70°C and two pieces of parafilm were placed with a 5 mm wide gap between them. A cover glass was added on top and the assembly was cooled down to room temperature. The glass surface was functionalized using BSA and biotinylated BSA (bBSA) in a ratio of 1:10. A solution with 10% BSA was incubated on the cover glass for 10 minutes. After thorough washing with phosphate buffered saline (PBS) buffer including a 5 minute incubation time, streptavidin (0.3 mg/mL, Sigma-Aldrich, USA) was incubated for 5 minutes. After washing again, the biotinylated tethering protein (gelsolin, cappuccino, spire or another actin binding protein) has been added and again incubated for 5 minutes. After washing with G-buffer, actin was added and filament growth on the nucleator proteins were imaged.

For imaging of actin oligomerization and other single-molecule measurements, the surface was functionalized using PEG/bPEG silane (Nanocs Inc., USA) and the flow chamber was assembled using a cover glass and a microscope slide with two holes for inlet and outlet tubes.

2.2.6 Confocal Microscopy

While TIRFM limits the excitation volume to the solution very close to the cover glass, confocal microscopy goes one step further and just detects fluorescence from a small ellipsoidal volume in the solution. By using a pinhole at a focal plane in front of the detector, the signal originating from outside the focus is suppressed and the focal plane in the solution and on the detector are aligned (con-focal) (M., 1961, Fig. 2.5). Thus, the signal-to-noise ratio increases as Raman scattered light from the solvent and emission from impurities in the solvent or the buffer do not reach the detector to the same extent. Often, a second pinhole is placed in the illumination pathway to improve the beam profile of the excitation source.

The focal point itself is not infinitesimally small, but diffraction-limited. The minimum distance d_{min} between two point objects where they are still distinguishable using an optical system was defined by Rayleigh:

$$d_{min} = 1.22\frac{\lambda}{2NA} \tag{2.7}$$

where λ is the wavelength of the excitation light and NA is the numerical aperture of the objective. The NA is defined as the product of the index of refraction n of the medium between the objective and the sample and the sine of the angle θ, which is the half-angle of the cone of light that enters the objective:

$$NA = n \cdot \sin\theta \tag{2.8}$$

Objectives with high numerical apertures have been developed by maximizing the acceptance angle θ and by the use of immersion oils and cover glasses with a high refractive index. However, since the NA is limited, the focal point will always have a finite dimension according to equation 2.7. The resulting pattern, a spot with maximum brightness in the middle and concentric rings around it, is called the Airy disk or the point spread function (PSF), which describes the excitation volume produced by a point source of light. The PSF is usually assumed to be a 3D Gaussian. The intensity profile is then given by

$$PSF(x,y,z) \propto exp^{-2(\frac{x^2+y^2}{\omega_r^2}+\frac{z^2}{\omega_z^2})} \tag{2.9}$$

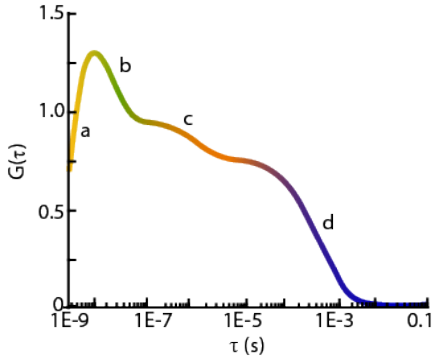

FIGURE 2.6: Autocorrelation function (ACF) of freely diffusing fluorophores. Different processes observable in the ACF are highlighted. a: photon antibunching, b: rotational diffusion and dynamics, c: photophysics of the dye and d: translational diffusion.

with ω_r and ω_z describing the dimensions in lateral and axial direction, respectively, from the center to the position where the signal decreased by a factor of $1/e^2$. The axial direction is always more extended. Typical values are about 200 nm for ω_r and 1 μm for ω_z.

When a confocal pinhole is used, the PSF has to be corrected for the cutoff:

$$PSF_{confocal} = PSF_{excitation} \cdot PSF_{detection} \tag{2.10}$$

The product of two Gaussian functions is again a Gaussian function, but with a narrower width. Precisely, the standard deviation and therefore the width of the Gaussian is narrower by a factor of $\sqrt{2}$. This could be used to resolve cellular structures with a better resolution than in conventional widefield microscopy using scanning confocal microscopy, however, the loss in intensity hinders this approach for lateral resolution.

2.2.7 Fluorescence Correlation Spectroscopy

Fluorescence correlation spectroscopy (FCS) is used here as a solution-based method. It is used to extract information from the fluctuations in intensity. Freely diffusing molecules, i.e. proteins or DNA labeled with a fluorescent dye are measured with a confocal microscope with an observation volume of approximately 1 fl in solution. When a dye or a labeled protein diffuses through the observation volume, it gives a signal dependent on its position and thus, the time. The decay over time of the autocorrelation function $G(\tau)$

of the intensity fluctuations (Equ.2.11) depends on the properties of the dye, the setup and the diffusion constant of the measured molecule.

$G(\tau)$ is defined as

$$G(\tau) = \frac{\langle \delta F(t) \delta F(t+\tau) \rangle}{\langle F(t) \rangle^2} = \frac{\langle F(t) F(t+\tau) \rangle}{\langle F(t) \rangle^2} - 1 \tag{2.11}$$

with τ the lag-time and $\delta F(t) = F(t) - \langle F(t) \rangle$, i.e. the fluctuation of the fluorescence intensity F. Thereby, $G(0)$ is inversely proportional to the average number of dye molecules inside the observation volume $\langle N \rangle$ as $G(0) = \gamma / \langle N \rangle$. The factor γ will be described below.

The fluorescence intensity F depends on the concentration and properties of the fluorophore (quantum yield Q and absorption cross-section σ) and on the properties of the setup. These include the detection efficiency for the emitted photons, q, and the profile of the observation volume. The characteristics of a fluorophore and the setup are often conveniently described by the brightness $B = q\sigma Q$. The observation volume is assumed as a 3D Gaussian as in equation 2.9.

Predominantly, FCS is used to measure the translational diffusion coefficient D of the labeled species. With a 3D Gaussian observation profile, the autocorrelation function with a diffusion term is given by:

$$G(\tau) = \frac{\gamma_{FCS}}{\langle N \rangle} \cdot \left(\frac{1}{1 + \frac{\tau}{\tau_D}} \right) \cdot \left(\frac{1}{1 + \left(\frac{\omega_r}{\omega_z} \right)^2 \cdot \frac{\tau}{\tau_D}} \right)^{\frac{1}{2}} \tag{2.12}$$

where γ_{FCS} is a geometrical factor accounting for the shape of the observation volume and τ_D is the diffusion time, given by:

$$\tau_D = \frac{\omega_r^2}{4D} \tag{2.13}$$

where D is the diffusion constant.

γ_{FCS} is $2^{-3/2}$ for one-photon excitation. The effective volume, considering the γ_{FCS} factor, is given by:

$$V_{eff,\gamma} = \pi^{3/2} \omega_r^2 \omega_z \tag{2.14}$$

Using equations 2.13 and 2.12, the dimensions of the observation volume can be calibrated before the measurement of the sample of interest. ω_r and ω_z are typically determined experimentally by using a freely diffusing dye in solution with a known diffusion constant D.

The γ_{FCS} can also be included in the effective volume as

$$V_{eff} = \left(\frac{\pi}{2}\right)^{3/2} \omega_r^2 \omega_z \tag{2.15}$$

Either way, the measured concentration of the labeled species is identical. However, the molecular brightness $\epsilon = \langle F \rangle / \langle N \rangle$ of the measured dye has to be interpreted differently. When γ_{FCS} is included in the effective volume, ϵ corresponds to the average brightness in the observation volume. When γ_{FCS} is included in the autocorrelation function, it corresponds to the peak brightness of the fluorophore in the center of the observation volume.

The autocorrelation function contains information about the diffusion behavior of the labeled species as they diffuse in and out of the observation volume, thereby inducing fluctuations in the measured fluorescence intensity. However, the autocorrelation function of fluorescent dyes is also influenced by photophysics of the dye, conformational dynamics of the sample when they affect the fluorescence properties of the dye and photon antibunching. Due to the different time scales of these processes, they appear at different time lags in the autocorrelation function (Fig. 2.6).

2.3 Zero-mode Waveguides

Zero-mode waveguides in the form as described here have been developed about 15 years ago and are now mainly used for parallel sequencing applications (Levene et al., 2003; Garoli et al., 2019). They contain thousands of apertures with diameters typically in the range of 30 to 200 nm, formed by holes in metal deposited on fused silica (Fig. 2.7, 2.8). The main motivation for developing these structures for biophysical research can be found in the physiological concentrations of biological samples. For many proteins, the concentration of their reaction partners in the cell is in the micromolar range, as their dissociation constants indicate (Moran-Mirabal and Craighead, 2008). Also for successfull polymerization, a critical concentration has to be reached.

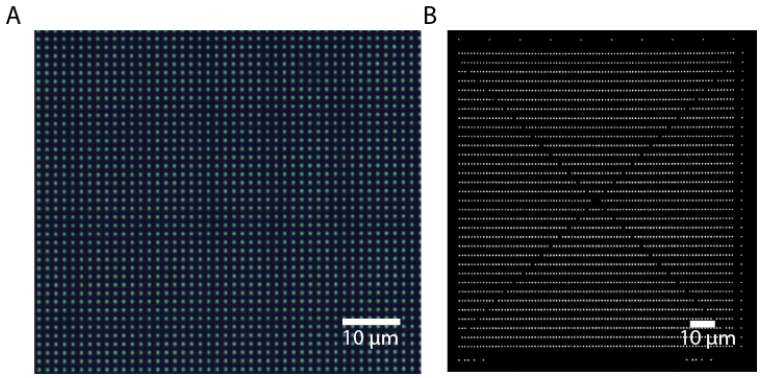

FIGURE 2.7: Bright field images of ZMWs. A: ZMW array fabricated by Kherim Willems at the University of Leuwen, Belgium. B: ZMW array commercially bought from Pacific Biosciences, USA.

For actin, the critical concentration is in the several hundred nM range (Bugyi and Carlier, 2010, Pollard, 1986). For fluorescence microscopy methods, these concentrations are to high for single-molecule sensitivity. For confocal microscopy for example, only pico- to nanomolar concentrations of labeled molecules are suitable, otherwise more than one molecule will diffuse through the observation volume at a time and the single-molecule sensitivity will be lost. Zero-mode waveguides confine the observation volume to the attoliter range (Fig. 2.8), thereby allowing concentrations of the labeled species up to the micromolar range.

ZMW are fabricated by depositing a layer of about 100 nm of metal, often aluminum, onto the surface of a microscope cover glass (Levene et al., 2003). The apertures are formed for example by focused ion beam drilling and have a diameter of about 100 nm. When the apertures are hit by a laser beam through the cover glass, an evanescent field is created as the dimensions of the apertures only allow the zero mode to pass through. Thereby, there is a cut-off wavelength above which no propagating modes are allowed inside the apertures (Levene et al., 2003). The cut-off wavelength λ_c for circular apertures with diameter d is at $\lambda_c = 1.7d$. Light with a wavelength longer than λ_c is evanescent inside the apertures and its intensity $I(z)$ decays exponentially in z:

$$I(z) = I(0)e^{\frac{z}{\Lambda}} \tag{2.16}$$

with

$$\frac{1}{\Lambda} = 2\sqrt{\frac{1}{\lambda_c^2} - \frac{1}{\lambda_m^2}} \tag{2.17}$$

where Λ is the decay constant, and λ_m is the wavelength of the incoming laser beam (Levene et al., 2003). Here, the diameter of the apertures was 140 nm, which results in a decay constant Λ of 136 nm with λ_m = 488 nm.

The geometry of ZMW has been shown to influence the kinetics of biomolecules measured in the apertures. In some experiments using ZMW, kinetic rates have been decreased by up to an order of magnitude (Christensen et al., 2016; Uemura et al., 2010). The arrival rates of freely diffusing species to the surface-bound receptors was affected, which caused the authors to increase the concentration to more than 20x the concentration used in bulk assays (Uemura et al., 2010).

For the experiments carried out here, a biotinylated nucleator protein was bound at the bottom of the ZMW. Thereby, it is essential to avoid the binding of multiple proteins per well, so that the recorded intensity traces contain only the information of one growing filament. The occupancy of the apertures by the biotinylated nucleator protein is assumed to follow Poissonian statistics (Uemura et al., 2010) of the form

$$P(k) = e^{-\lambda}\frac{\lambda^k}{k!} \tag{2.18}$$

where λ is the mean occupancy and k is the number of molecules in the aperture. In a typical experiment 600 to 700 apertures showed any signal from a total of 3000 apertures. Hence the average occupancy λ was at 0.22 ± 0.02. The probability that there are two or more molecules ($k \geq 2$) in a single aperture is then 0.020 ± 0.003. This means that of the traces that show a signal, 10% to 12% would originate from two or more nucleator proteins in one aperture. For every experiment, the number of wells that showed any intensity was monitored carefully, so that λ was always at 0.22 or lower.

2.3.1 Fabrication and Functionalization of ZMW

ZMW were commercially obtained from Pacific Biosciences (smartChips, Pacific Biosciences, USA) or were produced by Kherim Willems, PhD, at the University of Leuven, Belgium. The fabrication involves the sputtering of a

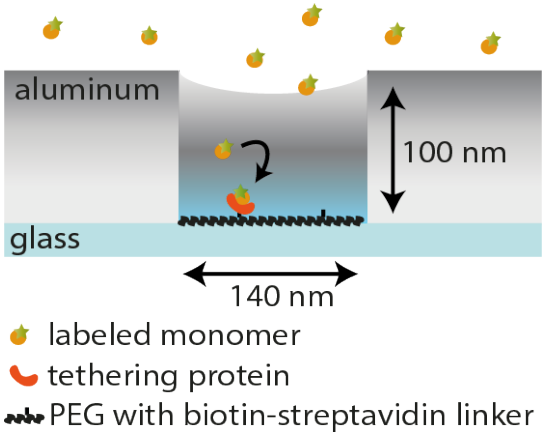

FIGURE 2.8: ZMW schematic. Holes in the aluminum layer deposited on a cover glass form apertures. Inside the apertures, an evanescent field is created when the structure is illuminated from below. The light cannot propagate, hence the term "zero-mode" waveguide. The bottom of the ZMWs are functionalized with PEG and biotinylated PEG, that allows the binding of a biotinylated tethering protein via a biotin-streptavidin link. Fluorescently labeled monomers bind to the tethering protein and the assembly process begins.

100 nm aluminum layer onto a cover glass. The holes that will later function as zero-mode waveguides are produced via chemical etching. The process is described in more detail in chapter 5. The commercial waveguides had already a surface functionalization according to (Korlach et al., 2008). The self-produced waveguides were functionalized using 2% polyvinylphosphonic acid (PVPA) (2 min., 90 °C) to passivate the plasma cleaned aluminum surface and prevent binding of the proteins to the walls of the apertures. Afterwards, the ZMW have been incubated for 4 h in polyetheleneglycole (PEG) (6-9 units) and biotinylated PEG in toluene at 55 °C. The functionalized ZMW have been stored in the desicator and used within 4 days.

2.4 Principles of Protein Assembly

The formation of oligomers and structured protein aggregates in the form of filaments is a common mechanism in biology. It is used to achieve a gain or modification of function that can be of regulatory, enzymatic or structural nature. The oligomerization process is, in itself, highly regulated by associated proteins, allowing the cell to adjust to external and internal changes in a fast and efficient way (Machesky and Insall, 1999).

The principle of regulated protein assembly and disassembly is most abundantly used in the cytoskeleton. It provides structure and the ability for

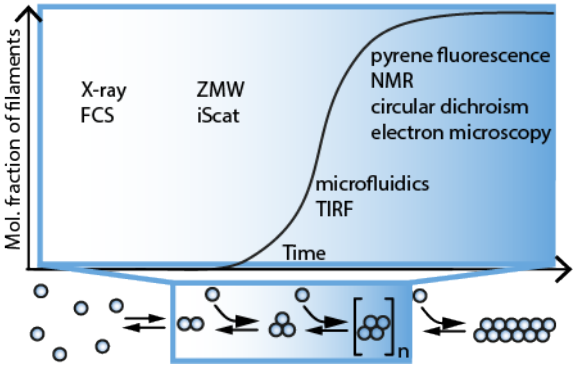

FIGURE 2.9: Protein assembly and applicable methods for the different stages of the assembly process. Assembly is visualized as the molar fraction of protein inside fibrillar structures. In the beginning, small oligomers form and disassemble dynamically leading to the so-called lag-phase. For single monomers, X-ray or FCS data are applicable methods. Once the thermodynamic barrier has been overcome and stable oligomers formed, polymerization is fast and the fibrillar protein content increases quickly until an equilibrium is reached. For the study of stable oligomers and fibrillar strucutures, a pyrene assay or the other methods listed on the right side yield interesting insights. For the study of small oligomers and their fast kinetics, ZMW or iScat can be used.

cytokinesis, but is also involved in intracellular transport, regulation and intercellular contacts (Machesky and Insall, 1999; Jamora and Fuchs, 2002). Its components, actin, microtubulin and intermediate filaments are each composed of globular monomeric proteins of a few nanometers in size, which assemble together to form filaments that can reach the micrometer range in length. While the cytoskeleton is crucial for the cell, other proteins can self-assemble into large fibrils that are associated with diseases such like Alzheimer's, diabetes or Parkinson's (Chiti and Dobson, 2006). Remarkably, all these different proteins form very similar fibrillar structures (Chiti and Dobson, 2006).

While the structure of the monomeric proteins as well as the assembled filaments is known in most cases, the conformations and kinetics of the oligomers is more challenging to study due to the ever-changing nature of the system (Fig. 2.9). However, some microscopic principles of protein self-assembly have been identified. In the early studies, bulk measurements of the assembly process were used to monitor the increase of filamentous protein over time using a pyrene assay. This assay is based on the increased pyrene fluorescence inside fibrillar structures (Cooper, Walker, and Pollard, 1983). Thereby, actin monomers are labeled with N-(1-pyrene)-iodoacetamide at the only surface cystein. In the monomeric form, the labeled actin fluoresces weakly at 384 nm,

but, in its filamentous form, the fluorescence is increased by a factor of 20 due to a change in the local environment of the pyrene. This measurement technique is widely used but only provides information about the total polymer mass without revealing any details about individual oligomer species and their dynamics.

Together with electron microscopy, circular dichroism and NMR studies, these bulk measurements provide good insight into the assembly process on a stage where stable structures have already formed (Fig. 2.9) (Pollard and Mooseker, 1981; Cohen et al., 2012; Xue, Homans, and Radford, 2008). On the monomer level, crystallography data and fluorescence correlation spectroscopy can shed light on the protein structure and binding behavior. The measurement of individual small oligomers is most challenging due to the unstability of the early oligomers and the fast growing of the stable oligomers. Recently, fluorescence microscopy techniques have been employed with the aim of measuring small oligomers using TIRFM and microfluidics (Horrocks et al., 2016; Horrocks et al., 2015). However, microfluidics with pyrene fluorescence as a read-out signal provides a signal after the first polymers have formed already. For the study of individual oligomers and their kinetics, iScat and ZMW have been used (Andrecka et al., 2016; Hoyer et al., 2018).

The simplest form of protein self-assembly into filaments can be imagined by the sequential addition of monomers. This process results in a slow primary nucleation phase where oligomers assemble and disassemble (Fig. 2.9) (Michaels et al., 2017; Arosio, Knowles, and Linse, 2015), followed by a polymerization phase where monomers are added or removed according to the association and dissociation kinetics of the filament. The slow nucleation step in the beginning is responsible for the so-called lag-phase observed in bulk experiments measuring the filamentous protein content (Fig. 2.9). The existence of the primary nucleation step indicates a thermodynamic barrier for the formation of small oligomers, which are unstable and easily dissociate into monomers. With formation of the smallest stable structure, the nucleus, this barrier is overcome and the faster polymerization kinetics take over. Actin and tubulin are considered to follow a primary nucleation mechanism (Kasai, Asakura, and Oosawa, 1962; Johnson, 1976).

During primary nucleation, a conformational conversion of the oligomers is sometimes required for successful polymerization (Cremades et al., 2012; De et al., 2019; Shammas et al., 2015). For example, the tau protein was found to

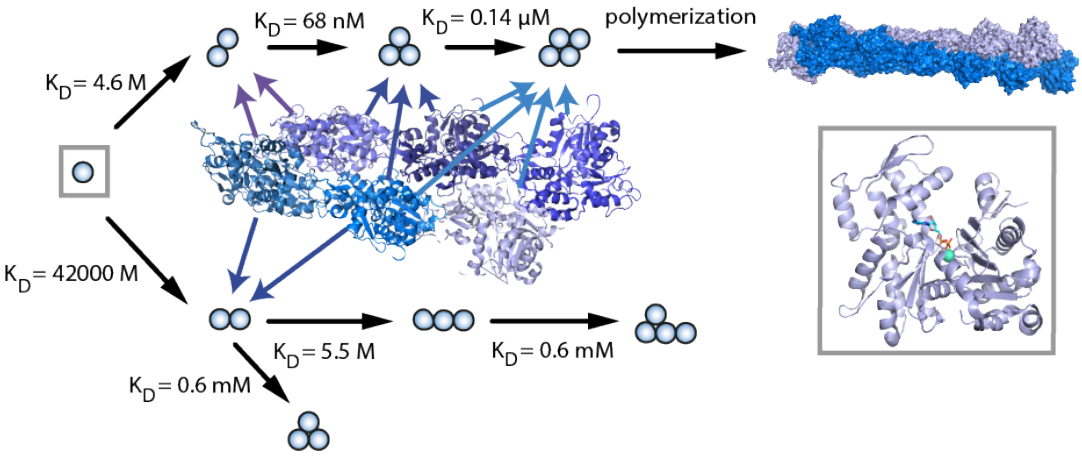

FIGURE 2.10: On- and off-pathway events during spontaneous actin nucleation. Of the two possible dimers, one leads to a stable trimer, the nucleus, with high probability. The other one can restructure itself into the nucleus or continue off-pathway. Other trimers and tetramers are possible (Qualmann and Kessels, 2009; Sept and McCammon, 2001). The structure of the monomer is depicted on the right (PDB structure 3HBT). Filament structure PDB 3G37 (upper right), pointed end assembly PDB 2Y83 (middle).

first assemble into non-polymerizable oligomers, which undergo a structural change and subsequently start polymerizing (Shammas et al., 2015).

In contrast to primary nucleation, secondary nucleation depends on pre-formed filaments that serve as a new oligomer source through fragmentation or heterogeneous nucleation (Michaels et al., 2017; Arosio, Knowles, and Linse, 2015). This highly accelerates filament formation, as the slow primary nucleation step is circumvented. Secondary nucleation is predominantly found for disease-related protein assembly (Knowles et al., 2009; Hortschansky et al., 2005; Meisl et al., 2014; Buell et al., 2014, but also for actin (Wegner, 1982; Wegner and Savko, 1982; Schmoller et al., 2011).

2.4.1 Actin Self-assembly

Actin and actin-like proteins are ubiquitous in biological systems (Dominguez and Holmes, 2011). The actin cytoskeleton in eukaryotes is linked to many cellular functions, including cell division, endocytosis and cell motility (Blanchoin et al., 2014). The many cellular functions of actin are directly linked to its ability to self-assemble into filaments (Blanchoin et al., 2014). G-actin is composed of two major subunits, whose interface form the nucleotide binding pocket (Fig. 2.10 right panel) (Kabsch et al., 1990). The nucleotide binding cleft has a closed conformation in the ATP- and ADP-P_i-bound states and

opens after P_i is released (Pfaendtner et al., 2009). Whereas G-actin hydrolyses ATP over the time course of hours (Rould et al., 2006), F-actin does so several orders of magnitude faster (0.3 s^{-1}) (Blanchoin and Pollard, 2002).

Actin filaments are double stranded filaments arranged in a head-to-tail manner (Fig. 2.10 middle) (Fujii et al., 2010). The monomers within the filament lattice have a different conformation than those free in solution. A relative twist of the two major actin subunits of about 20° results in a flat conformation. Upon polymerization, this flattening of the monomers results in a more stable filament structure (Oda et al., 2009, Otterbein, Graceffa, and Dominguez, 2001). This conformational change brings the residue coordinating the attacking water molecule closer to the ATP, explaining the higher ATP-hydrolysis rate in F-actin (Vorobiev et al., 2003; Graceffa and Dominguez, 2003; Otterbein, Graceffa, and Dominguez, 2001).

The conformational change of the actin monomers during polymerization is inhibited by certain molecules like latrunculins, which show a macrolide-based structure (Fig. 2.14). Latrunculin A (LatA) binds to monomeric actin above the ATP binding site, thereby preventing ATP-hydrolysis and the rotation of the actin subdomains (Morton, Ayscough, and McLaughlin, 2000; Rennebaum and Caflisch, 2012). As a consequence, LatA disrupts actin filaments when added to cells (Spector et al., 1983) by preventing the formation of new filaments (Coué et al., 1987).

G-actin in buffer self-assembles spontaneously into filaments via a nucleation-elongation mechanism (Fig. 2.10) (Sept and McCammon, 2001, Frieden, 1983). In this model, a very fast dissociation rate (106-108 s^{-1}) of the dimer and the trimer (103 s^{-1}) hinder the formation of tetramers that, once formed, will elongate until an equilibrium is reached with the solution (Sept and McCammon, 2001). In the literature, there are some hints that actin can assemble into two different dimers, the upper or parallel and the lower or antiparallel dimer (the two dimers in Fig. 2.10) (Mockrin and Korn, 1983; Millonig, Salvo, and Aebi, 1988; Bubb et al., 2002; Graceffa, Lee, and Stafford, 2013; Grintsevich et al., 2010; Qu et al., 2015). The terms parallel and antiparallel refer to the relative orientation of the two actin monomers. Whereas the upper dimer is a potent nucleator (Mockrin and Korn, 1983), the lower dimer can be transiently incorporated into filaments, but is thought to hinder nucleation and polymerization (Millonig, Salvo, and Aebi, 1988; Grintsevich et al., 2010). The instability of the dimers and trimers leads to a so called lag phase in actin

polymerization assays, i.e. the filament mass starts to increase after a certain waiting time at the beginning of the self-assembly process (Fig. 2.9).

The two ends of the actin filament have different properties and are referred to as the barbed end and the pointed end, according to the orientation of the monomers in the filament structure. The polarity of actin filaments has first been observed using electron microscopy, where the two ends have been identified by decoration with myosin "arrowheads" (Huxley, 1963; Pollard and Mooseker, 1981). The faster elongation rate at the barbed end leads to treadmilling *in vitro*, where monomers dissociate from the pointed end and bind to the barbed end (Wegner, 1976). Polymerization rates for barbed end and pointed end elongation are 11.6 $\mu M^{-1}s^{-1}$ and 1.3 $\mu M^{-1}s^{-1}$, respectively (Pollard, 1986). The difference arises from the addition of ATP-actin monomers predominantly at the barbed end. After incorporation, ATP is hydrolysed and the phosphate is released. The resulting ADP-actin is transferred to the pointed end of the filament through more incorporation of monomers at the barbed end and more dissociation of monomers at the pointed end. It then dissociates at the pointed end of the filament. Afterwards, ADP is exchanged for ATP and the actin monomer can get incorporated again at the barbed end.

As for all multistranded filaments, actin polymerization occurs above a critical concentration C_c (Fig. 2.11):

$$C_c = \frac{k_{off}}{k_{on}} \tag{2.19}$$

Below C_c, the polymerization rate is negative and the filaments are shrinking. Because of the different polymerization rates for barbed end and pointed end growth in actin, there are two critical concentrations for each end (Fig. 2.11). Around the critical concentration, slight changes in the available monomer numbers lead to drastic changes in filament length, allowing for cellular regulation of actin filament length by monomer sequestering proteins (Howard, 2001).

2.4.2 Actin Nucleators

The lag phase observed in actin polymerization assays (Fig. 2.9) can be circumvented by actin nucleators. In the cell, the very small number of actin nuclei

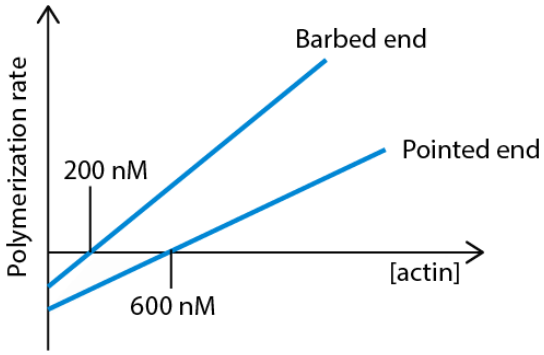

FIGURE 2.11: Kinetics and critical concentration of pointed end and barbed end growth. Critical concentrations are different for barbed-end and pointed-end growth and mark the concentration above which filaments are growing, i.e. the polymerization rate is positive. The y-intersect corresponds to the dissociation rate.

(0.1 nM) allows for tight regulation by nucleating proteins, which have a stabilizing effect on actin dimers or trimers (Howard, 2001; Campellone and Welch, 2010). There are three classes of actin nucleators: the actin-related protein 2/3 (Arp2/3) complex, formins and WH2-domain (Wiskott-Aldrich syndrome protein-homology 2-domain) containing proteins (Campellone and Welch, 2010). Whereas the Arp2/3 complex causes actin to form branched networks at cell membrane protrusions or invaginations, formins promote unbranched filament nucleation and elongation. WH2-domain containing proteins contain multiple WH2 domains, i.e. a small peptide that binds actin monomers and faciliates nucleation (Renault, Bugyi, and Carlier, 2008, Fig. 2.12). Based on the amount of protein needed to promote filament formation, nucleators are loosely defined as strong or weak (Dominguez, 2009).

In the following, three actin nucleators studied in this thesis will be described: the formin cappuccino as a strong nucleator, the WH2-domain containing protein spire, and a protein with a weak nucleation function, gelsolin .

Cappuccino and Spire

Spire and Cappuccino were first discovered at the same time in a Drosophila screen for mutations affecting oocyte polarity (Manseau and Schuepbach, 1989). The phenotype showed a reduction in the actin filament formation rate (Manseau, Calley, and Phan, 1996), which was explained when Cappuccino was found to encode an actin nucleator of the formin class (Manseau, Calley, and Phan, 1996) and Spire a protein with multiple copies of the WH2 motif, which binds actin monomers (Wellington et al., 1999, Fig. 2.12 C).

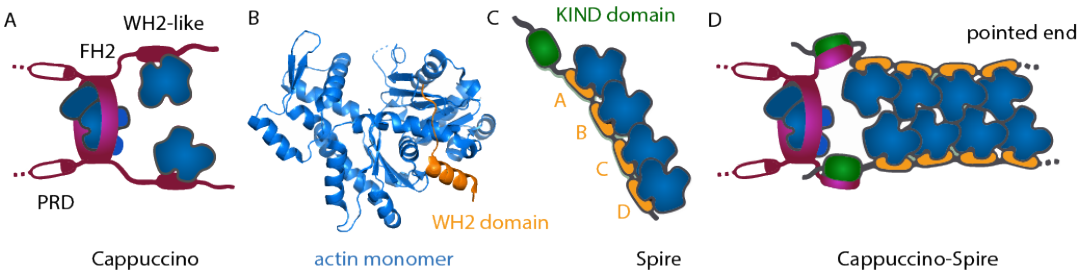

FIGURE 2.12: Actin nucleation by cappuccino and spire (Dominguez, 2016 Ducka et al., 2010 for structure 3MN5 pdb). A: schematic of actin nucleation by cappuccino. B: structure of monomeric actin with the WH2 binding motif highlighted in orange. C: schematic of actin binding to spire. The domains A, B, C and D bind monomeric actin. D: the interplay between cappuccino and spire during actin nucleation.

Formins form dimers that cap the barbed end and thereby stabilize the formation of an actin dimer (Xu et al., 2004). In solution, dimerized cappuccino is autoinhibited (Bor et al., 2012). After binding to cappuccino, the actin seed is able to elongate by the insertion of monomers between the formin cap and the barbed end of the filament (Fig. 2.12 A) (Baum and Kunda, 2005). As elongation takes place, the formin will step up processively at the filament tip as if climbing a growing spiral staircase (Baum and Kunda, 2005). As a result, formin-induced actin nucleation generates long, unbranched bundles of actin filaments.

The conserved protein spire belongs to a third class of actin nucleators. It has four WH2 repeats, which bind four actin monomers, which are thus brought into close proximity to one another (Fig. 2.12 D). This forms a novel single strand nucleus for barbed end filament elongation (Baum and Kunda, 2005). WH2-like motifs often occur in actin binding proteins involved in actin monomer sequestration, activation of the Arp2/3 complex, actin filament elongation and actin nucleation (Paunola, Mattila, and Lappalainen, 2002). WH2-containing proteins can be divided into two subclasses: those related to the Arp2/3 activator WASP (Wiskott-Aldrich-Syndrome protein) and those related to thymosin-β4, an actin monomer sequestering protein. The WH2 domain itself is an approximately 35 residue actin monomer binding motif that is highly conserved (Paunola, Mattila, and Lappalainen, 2002). The target sequence, LKKTET, on the surface of ATP-actin is itself highly conserved as well (Fig. 2.12 B).

In WASP-related proteins, the WH2 domain promotes actin filament formation by bringing actin monomers close to the Arp2/3 complex (Pollard and

Borisy, 2003). In contrast, in thymosin-β4-related proteins, it inhibits actin filament elongation by binding to and sequestering monomers (Paunola, Mattila, and Lappalainen, 2002). In the case of spire, the amino terminus that carries the WH2 repeats can nucleate actin filaments growing on the barbed ends as spire caps the pointed end of the filaments (Quinlan et al., 2005). Spire-mediated nucleation is proposed to work via binding of an actin monomer to the carboxy-terminal WH2 domain and then subsequently to the other domains (Fig. 2.12 C). This brings the monomers close together and forms a nucleation seed. Thereby, the carboxy-terminal WH2 domain caps the pointed end of the newly formed filament. As a result, spire generates unbranched filaments like cappuccino, that are resistant to pointed end disassembly (Quinlan et al., 2005).

Spire and cappuccino work together during Drosophila oogenesis (Quinlan, 2013; Dominguez, 2016). They form a 1:1 complex between the KIND domain of spire (Fig. 2.12) and the C-terminal tail of cappuccino, which competes with the autoinhibition of cappuccino (Vizcarra et al., 2011; Zeth et al., 2011; Bor et al., 2012). Whereas spire can bind actin monomers in this complex, the nucleation activity of cappuccino is inhibited (Quinlan et al., 2007; Vizcarra et al., 2011). Spire dimerizes upon binding to formins and its nucleation capacity is greatly enhanced (Quinlan et al., 2007; Vizcarra et al., 2011). This could be due to the duplication of the WH2 motifs upon dimerization, which would lead to the recruitment of actin subunits in the form of two parallel strands, as in the actin filament (Quinlan et al., 2007).

Gelsolin

Gelsolin is a Ca^{2+}-dependent pointed-end nucleator (Nag et al., 2013). It was first associated with the gel-sol transition of macrophage extracts (Yin and Stossel, 1979; Yin et al., 1981). It can cap and sever actin filaments, sequester G-actin and nucleate filaments *in vitro*. Gelsolin binds to the barbed-end of actin, thus allowing only pointed-end growth (Ditsch and Wegner, 1994).

The gelsolin structure adopts an inactive conformation until activated by Ca^{2+}-binding in the cytoplasma. In the inactive structure, the actin binding sites are occluded (Burtnick et al., 1997). Upon Ca^{2+} binding, large conformational changes result in the accessibility of the actin-binding sites. Gelsolin binds two actin monomers, forming a gelsolin-$(actin)_2$ (GA_2) complex (Coué and Korn, 1985; Bryan and Kurth, 1984). The first actin monomer binds to the C-terminal

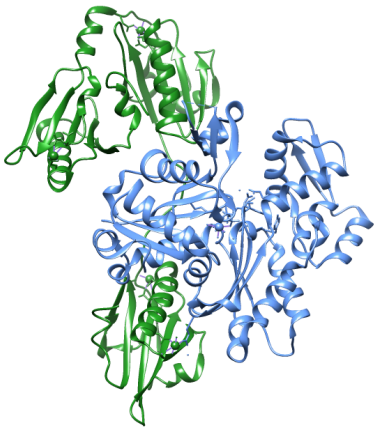

FIGURE 2.13: Structure of the gelsolin subdomains G1-G3 (green) bound to an actin monomer (blue). The structure of full-length Gelsolin (G1-G6) bound to an actin nucleus is not yet solved. PDB structure FFK3.

half of gelsolin and is easily exchangeable. It has a slow association rate constant of 0.015 to 0.07 $\mu M^{-1}s^{-1}$, dependent on the pH (Bryan and Kurth, 1984; Bryan, 1988; Khaitlina and Hinssen, 1997; Selve and Wegner, 1987). It can bind after the initial activation of gelsolin at 0.1. - 1 μM Ca^{2+} (Pope, Gooch, and Weeds, 1997; Kinosian et al., 1998; Lin, Mejillano, and Yin, 2000; Khaitlina and H., 2002).

The binding of the second actin monomer is independent of Ca^{2+}, however, a stable complex with two actin monomers needs Ca^{2+} concentrations above 10 μM (Khaitlina and H., 2002). The second monomer binds with a rate constant of 2 $\mu M^{-1}s^{-1}$ and has a dissociation rate of 0.02 s^{-1} (Schoepper and Wegner, 1991). It is believed that binding of the second actin needs further structural rearrangements of the C-terminal half of gelsolin that occur at high Ca^{2+} concentrations, possibly promoted by binding of the first monomer (Khaitlina and H., 2002; Khaitlina, Walloscheck, and Hinssen, 2004). The second actin monomer undergoes conformational changes in the GA_2 complex (Khaitlina and Hinssen, 1997).

The GA_2 complex was found in two different conformations (Hesterkamp, Weeds, and Mannherz, 1993; Doi, 1992). In one conformation, the actin dimer exists as the upper or parallel dimer (see above), whereas in the other conformation, the two actin monomers assume the lower or antiparallel conformation (Hesterkamp, Weeds, and Mannherz, 1993; Doi, 1992). The structural basis for the existence of the two GA_2 complexes can be found in the three actin binding sites of gelsolin that allow for different binding arrangements of

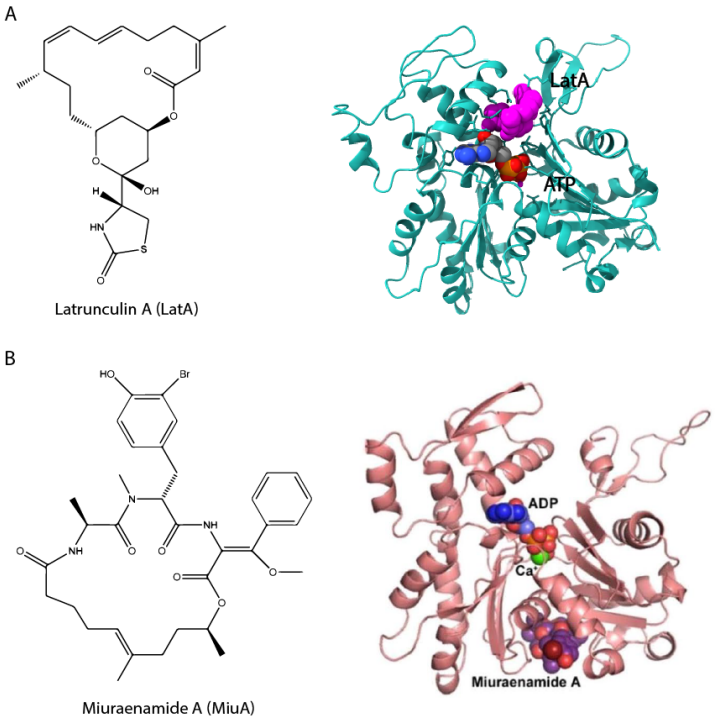

FIGURE 2.14: Latrunculin A (A) and Miuraenamide A (B) bound to actin. A: Structure of Latrunculin A (left) and structure of actin bound to LatA (purple) (right, pdb 1ijj). B: structure of Miuraenamide A (left) and structure of actin bound to Miuraenamide A (right) after 25 ns of a molecular dynamcis simulation (Wang et al., 2019). ADP is depicted in blue, Ca^{2+} in green and MiuA in purple. The image was taken from Wang et al., 2019 as part of the Creative Commons Attribution 4.0 International License (creativecommons.org).

the two actin monomers in the complex (Hesterkamp, Weeds, and Mannherz, 1993). It is believed that as long as the actin monomers in the GA_2 complex are in the antiparallel orientation, gelsolin does not act as a nucleator (Qu et al., 2015). Therefore, these complexes have to undergo a conformational change before polymerization can begin, which could be triggered by binding of the third actin monomer to the GA_2 complex (Qu et al., 2015). Accordingly, GA_2 acts only as a weak nucleator and its presence in actin polymerization assays does not abolish the lag phase (Coué and Korn, 1985).

2.4.3 Actin binding compounds

Actin binding compounds are widely used tools in cell biology to elucidate the interplay and function of actin and actin-binding proteins. Recently, actin binding compounds also became interesting for clinical use, as highly specific compounds have been discovered that bind differently to different actin isoforms, which allows targeting of muscular function via actin (Guhathakurta

et al., 2020). The structure and its specific binding site on the actin monomer define the function of the actin binding drug. Until now, many naturally occurring compounds have been found to alter actin function (Giganti and Friederich, 2003), either by destabilizing actin filaments, like Latrunculin A, or by stabilizing the filaments, like phalloidin. Phalloidin is a toxin from the mushroom *Amanita phalloides*. It binds tightly to actin filaments and stabilizes them (Wieland, Faulstich, and Fiume, 1978). In this work, phalloidin was used to stabilize the formed actin filaments inside ZMW to be able to measure the length of the filaments via photobleaching without depolymerization taking place during the measurement (chapters 3, 5).

Latrunculin A

Latrunculin A and B are toxins naturally occurring in the Red Sea sponge *Latrunculia magnifica*. They show a macrolide structure and reversibly disrupt the actin cytoskeleton when added to cells (Spector et al., 1983). They bind to monomeric actin and inhibit the formation of new filaments (Coué et al., 1987). Since its discovery, LatA has been widely used as a specific actin depolymerizing drug. LatA binds actin above the nucleotide binding cleft. Binding of the drug does not induce dramatic changes in the actin structure (Morton, Ayscough, and McLaughlin, 2000). It is thought to lock ATP in its binding cleft and inhibit the relative rotation of two actin subdomains, i.e. the flattening of the monomer structure which occurrs during polymerization (Fujii et al., 2010; Oda et al., 2009; Morton, Ayscough, and McLaughlin, 2000; Rennebaum and Caflisch, 2012).

Miuraenamide A

New actin binding compounds often mimic the binding of actin binding proteins, thereby interfering with the interplay between actin monomers, filaments and actin binding proteins. This addresses the challenge for new clinical drugs that lies in the importance of actin in biological functions. Therefore, a high specificity of the actin binding molecules, which could be used as clinical drugs, is needed.

Miuraenamide A (MiuA) is one of these newly investigated compounds for biological research tools or therapeutic options (Wang et al., 2019). It comes from a myxobacterium and is an actin filament stabilizing compound (Wang et al., 2019). It induces a tighter and stronger packing of the actin monomers

inside the filaments by shifting the D-loop, which is required for F-actin stabilization (Wang et al., 2019; Pospich et al., 2017).

Chapter 3

Data Analysis and Simulations

The goal of this thesis is to observe the individual steps of protein nucleation using fluorescence microscopy. Using ZMW or TIRFM, the intensity versus time traces of individual dye-labeled oligomers were measured. For the conversion of camera signal into monomer numbers, a series of analysis steps were applied (Fig. 3.1). First, the image series were corrected for lateral drift using a plugin for ImageJ as used in Tseng et al., 2011. Afterwards, I used TRacer, developed by Bässem Salem, to identify the bright ZMW spots in the image and calculate the background-corrected intensity versus time traces (Fig. 3.1 B). The step-wise increase in intensity was then fitted by a step-finding algorithm (Fig. 3.1 C). Afterwards, the resulting intensity steps were sorted into monomer number and the kinetics of each association or dissociation event were extracted. In the following, the analysis steps are depicted in more detail.

Furthermore, in this chapter, simulations of protein assembly will be described. Simulations have been performed to test the analysis methods under various conditions and to compare the experimental findings of the measurements of actin nucleation with a simulation of literature values. All software was written in Matlab (The MathWorks, USA).

3.1 From Camera Signal to Intensity

The intensity signal of the fluorescently labeled monomers binding to the nascent filament was recorded using an EMCCD camera (Andor iXON Ultra 888) and saved as grey value information in a time-series of tiff images. First, a drift correction was necessary in many cases because of the relatively long

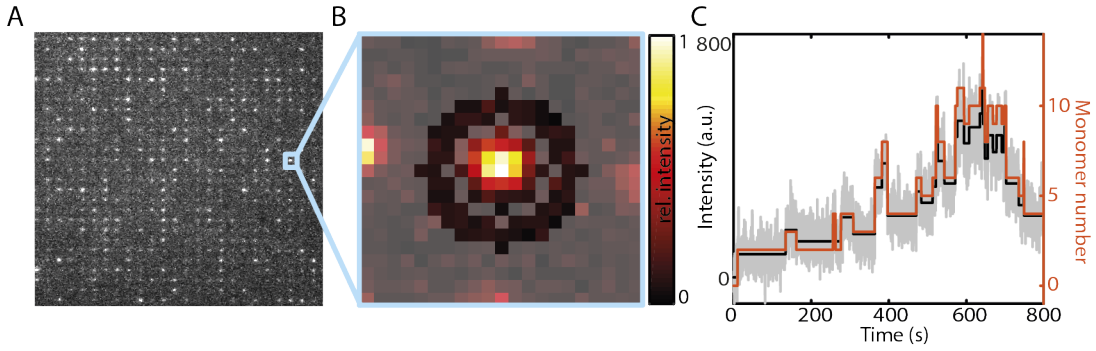

FIGURE 3.1: From the image to monomer numbers. A: An image of a ZMW array 400 s after the addition of actin-Cy5 to surface-bound biotinylated cappuccino. B: A zoom-in of a single waveguide showeing the cumulated intensity image with highlighted signal and background masks. C: background-corrected intensity trace (grey) with the result of the step-finding algorithm (black) and the resulting monomer trace (orange).

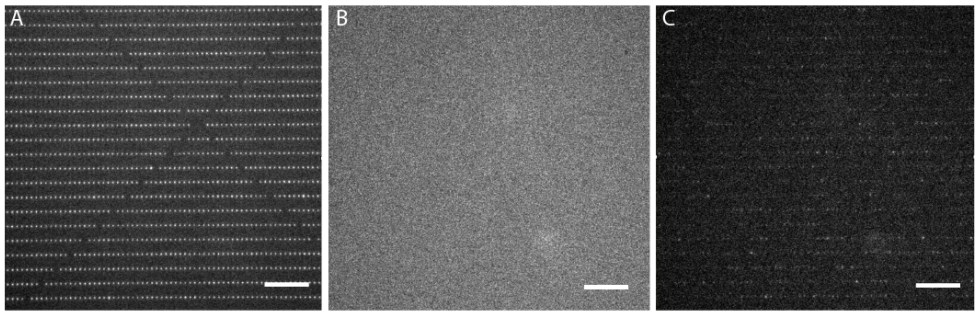

FIGURE 3.2: ZMW array before and after addition of actin. A: ZMW array illuminated by white light before beginning of the measurement. B: The same ZMW array without white light before addition of the actin. The apertures are not visible. C: The same array after addition of the actin monomers. Scale bar 10μm.

acquisition times of up to 20 minutes. Thereby, two difficulties arose: the appearance of fluorescent signal after the start of the movie made drift correction during the first frames a challenge, and second, the highly symmetric pattern of the ZMW image (Fig. 3.1 A) is a challenge for all drift correcting algorithms. Good results could be obtained using the ImageJ plugin Template_ matching, developed in Tseng et al., 2011, using the correlation coefficient on a subset of the image to avoid confusion by the pattern, and on a subset of frames to account for the different appearance of the images throughout the movie. The subsets of frames could then be aligned subsequently. Because of the small spot size of just a few pixels, subpixel registration was required.

Afterwards, the corrected .tiff files were loaded into TRacer, which identified

fluorescent spots by cumulating the pixel intensity values over the whole movie and identifying pixels with intensity above a threshold. By manually applying upper and lower grey value thresholds, the detection of fluorescent spots could be adjusted. After identifying the pixels that centered in high fluorescent intensity, a signal and a background mask were defined (Fig. 3.1). I optimized both masks for the use of ZMW, looking at the resulting SNR of the traces. Since the apertures had no effect on the pixel intensity before addition of the labeled monomers (Fig. 3.2), the intensity of the pixels corresponding to the signal mask was treated the same before and after the addition of the actin monomers. The intensity values of the traces were then calculated summing the pixels that belong to the signal mask in each frame (highlighted in Fig. 3.1 B). For background correction, the mean of the background mask around the signal was taken, averaged over 10 frames and multiplied by the number of pixels of the signal mask. Thus, intensity versus time traces were gained, which was then further analyzed.

3.2 Step-finding Algorithm

During the course of the experiment, fluorescently labeled monomers bind to the tethering protein at the bottom of the ZMW and dissociate again. This is visible in the intensity traces as upward and downward steps (Fig. 3.1 C). For the analysis of the binding and dissociation events, these steps have to be identified in the noise-overlaid intensity traces. Since the measurement depends on dye-labeled proteins, the laser intensity has to be optimized for the signal intensity as well as for photobleaching, which limits the achievable signal-to-noise ratio. To identify the steps in the intensity traces, different step-finding algorithms were evaluated and compared in my master thesis (Hoyer, 2014). The algorithm developed by Salapaka and coworkers (Aggarwal et al., 2012) yielded the best results for the ZMW data and will be described briefly in the following.

The aim of the algorithm is to identify true steps while minimizing the detection of false steps. The Salapaka algorithm tries to address these two criteria by optimizing a fit using a cost function. It is assumed that, in single-molecule data, the sampling rate is higher than the inter-arrival time of steps, thus, true steps are rare events in the data.

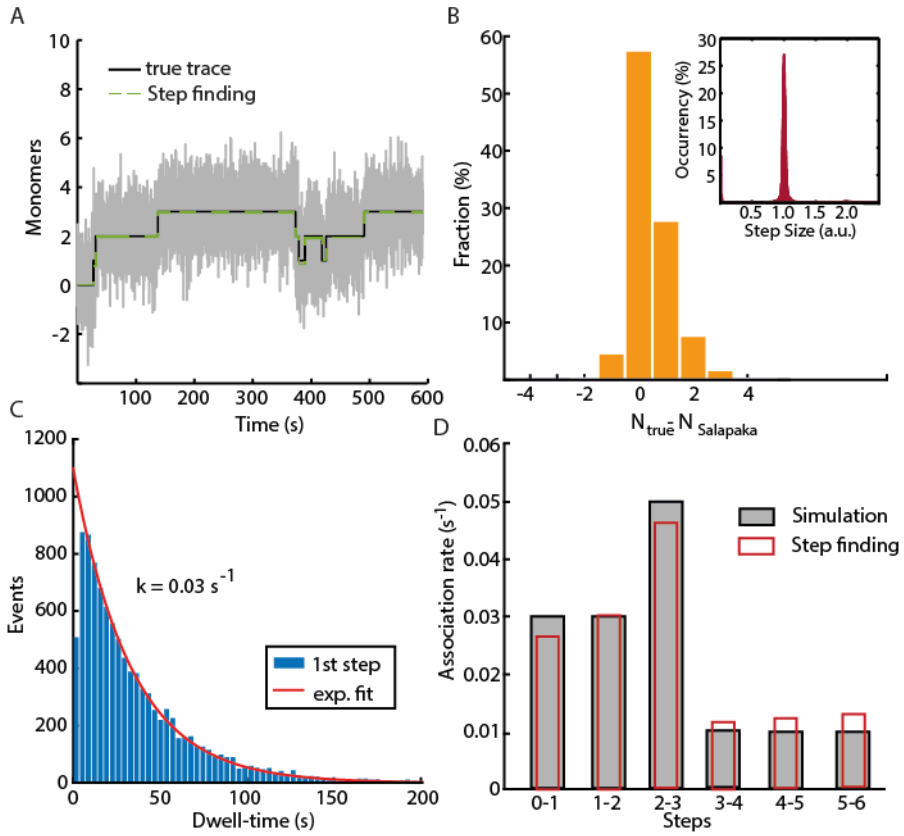

FIGURE 3.3: Testing of the step-finding algorithm. A: A simulated trace (black) with overlaid noise (SNR = 1) (grey) and the result of the Salapaka step-finding algorithm (dashed green line). B: Difference between the true simulated number of steps in a trace and the number of steps found by the step-finding algorithm. Inset: Step size distribution of the result of the step-finding algorithm. The simulated traces had a step size of 1. C: The arrival time distribution for the first up-step fitted by a single-exponential (red line). D: On-rates obtained from the exponential fits of the dewll times for the different steps. Grey: simulated input association rates for the addition of the individual steps, red: recovered rates from the noise-overlaid simulations using an exponential fit of the dwell times of the result of the step-finding algorithm.

When building up the estimate $\hat{x}$ for the signal x, the algorithm aims to have a high percentage of true positives and a low percentage of false positives. True positives are estimated without knowledge of the true signal via the $\mathcal{X}^2$ error, given by $\sum_k (y_k - \hat{x}_k)^2$, where y_k is the kth timepoint of the data and $\hat{x}_k$ the kth sample of the candidate $\hat{x}$. False positives are estimated by the total number of steps in the candidate. When underfitting, a low number of false positives is expected and, at the same time, a low number of true positives. When overfitting, a high number of true positives and a small $\mathcal{X}^2$ error, but also a high number of false positives occurs. To find an equilibrium between true and false positives, a cost function $J(\hat{x})$ was defined. The first term in equation 3.1 corresponds to the $\mathcal{X}^2$ error between the candidate $\hat{x}$ and the measured data y. The second term is a penalty factor for the introduction of more steps to avoid overfitting.

$$J(\hat{x}) = \sum_{k=1}^{N} (y_k - \hat{x}_k)^2 + W \sum_{k=1}^{N} \bar{\delta}(\hat{x}_k - \hat{x}_{k-1}) \tag{3.1}$$

Here, N is the total number of data points in the intensity trace and $\bar{\delta}(u) = 0$ if $u = 0$ and $\bar{\delta}(u) = 1$ if $u \neq 0$. Therefore, $\sum_{k=1}^{N} \bar{\delta}(\hat{x}_k - \hat{x}_{k-1})$ is the number of steps in $\hat{x}$. W determines the weight of the penalty factor and sets the weight between true positives and false positives. It was set to 50 for the ZMW data. An example of the result of the step finding algorithm is given in Fig. 3.1 C, black line.

The results obtained by the Salapaka algorithm were tested on simulated data overlaid with Gaussian noise assuming a signal-to-noise ratio (SNR) of 1 (Fig. 3.3). A SNR of 1 is the lower limit for experimental data, which contains traces with a SNR between 1 and 2, typically (Fig. 3.1 C). As simulated data, I used a growth process with defined association and dissociation rates for the addition and substraction of monomers. An association event is a step with the arbitrary step size of 1 upwards, a dissociation event is a step of step size 1 downwards. As parameters for testing the performance of the stepfinding algorithm, I looked at the number of steps in a trace, the step size distribution and whether the extracted waiting time distribution until the next upward step yielded the simulated input rates. The Salapaka algorithm was able to find the underlying simulated trace despite the low SNR of 1 (Fig. 3.3 A). The number of steps was correct for most traces, with a slight tendency towards underfitting as the number of steps found by the algorithm

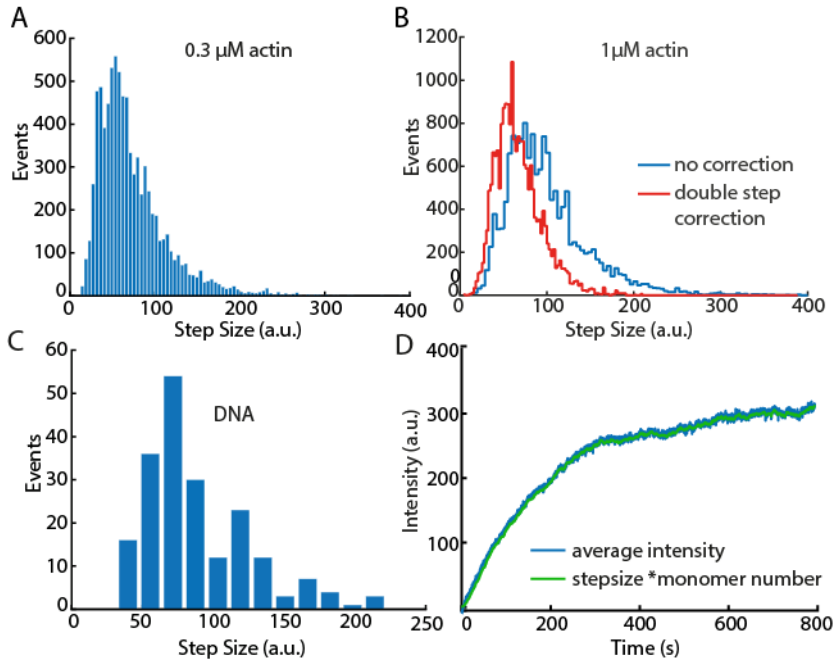

FIGURE 3.4: Step-size distributions in ZMW measurements. A, C: Intensity step-size distribution of 0.3 (A) or 1 μM (B) actin growing on gelsolin. For 1 μM actin, analysis without any correction (blue) and with double-step correction (red) was performed. B: Step-size distribution for a photobleaching experiment of surface-bound DNA strands labeled with atto-488 dyes, without correction. D: Overlap between the average intenstiy of 1 μM actin growing on gelsolin and the monomer number multiplied by the individual trace step size.

was one or two steps lower than the true number of steps (Fig. 3.3 B). The step-size distribution of the result showed a very narrow peak at 1 (Fig. 3.3 B inset), and the waiting times showed an exponential distribution whose fit yielded the input rate for all different steps (Fig. 3.3 C, D).

The result of the step-finding procedure was further converted into monomer numbers based on the intensity levels of monomers, as described in the next section. However, also the step size information could be used to compare the reproducibility of the measurements, and to quantify oligomer binding events measured in TIRFM (chapter 5).

3.3 From Intensity to Monomers

The conversion from intensity to monomer numbers was based on the number of up and down steps, corresponding to monomer association or dissociation events, as well as the expected intensity levels according to the intensity step size of a single dye, as described in more detail later in this paragraph. The

step-size distributions were reproducible for ZMW measurements of atto488 in different biological systems (Fig. 3.4). As a second system besides the assembly of actin monomers, DNA strands labeled with a known number of dyes have been attached to the ZMWs. During photobleaching, traces that show individual dissociation steps were measured (chapter 5). Since the step-finding algorithm treats down steps in the same manner as up steps, the step-size distributions between actin assembly and photobleaching of DNA-atto488 are comparable.

Thus, traces of 0.3 μM and 1 μM actin-atto488 binding to gelsolin and surface-immobilized DNA strands labeled with various atto488 dyes showed a very similar step size distribution (Fig. 3.4). In all cases, a shoulder in the histogram was visible at step-sizes approximately double the most abundant intensity step-size value, which became more prominent when the actin concentration was increased to 1 μM (Fig. 3.4 C, blue histogram). This indicates the presence of double steps, i.e. steps corresponding to two dye molecules binding at the same time or shortly after one another during a single frame. To account for these double or sometimes even triple steps, the step size of a single dye was determined and used as an input in the intensity to monomer conversion algorithm, developed by Rafael Correia at the Universidade NOVA de Lisboa in Lisbon, Portugal under the supervision of Alvaro Crevenna, PhD. First, the mean step size per experimental condition was estimated by fitting the step size distribution with a gamma function. Then, the intensity levels of a trace were binned using the estimated mean step size and all events within that bin were assigned to the same monomer number. In this way, a new, but very similar intensity trace was built, which was then converted into monomer numbers using the actual minimum step size of that intensity trace and splitting steps with double or triple the intensity value into two or three monomer steps. Since the input step size became a determining parameter this way, the consistency between calculated monomer numbers and measured intensity values was checked by comparing the average measured intensity traces with the monomer traces multiplied with the actually used step size. Only when the input parameters were correctly chosen, would the average traces overlap (Fig. 3.4 D) and the step-size distribution did not show a shoulder at higher values (Fig. 3.4 C, red histogram). With the double-step correction, the step-size distribution was reproducible for different actin concentrations and for photobleaching experiments on labeled DNA molecules (Fig. 3.4).

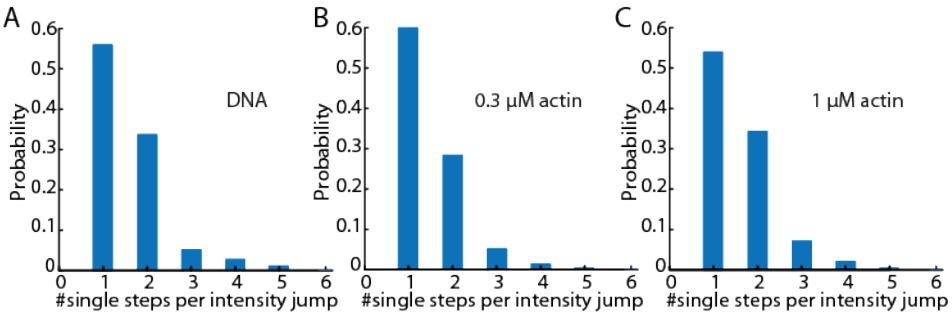

FIGURE 3.5: Prevalence of single and multiple steps per intensity change. A: For a photobleaching experiment of surface-bound DNA strands labeled with atto-488 dyes. B: For 0.3 actin growing on gelsolin. C: For 1 μM actin growing on gelsolin.

For simulations, the monomer number trace was built up simply by using the number and position of the up and down steps in a trace. When a double step correction was necessary, double and triple steps were identified by comparing each step to the mean and the mode of all steps in a trace.

In experiments, double steps could be the result of two fast subsequent monomer binding events, or it could be the binding of a single monomer labeled with two fluorescent dyes. To determine the main origin of the existence of multiple steps, I calculated the probability of having single or multiple steps in one intensity change for DNA-atto488 photobleaching experiments, as well as for a low and a high concentration of actin-atto488 (Fig. 3.5). The distribution was very similar for DNA and a low concentration of actin-atto488. In both cases, predominantly single steps are expected due to the low concentration in the case of actin, and the photobleaching of single dyes in the case of the DNA. For a higher concentration of actin, the probability of double and triple steps increased (Fig. 3.5 C). Thus, the main cause for multiple steps in the intensity-time traces was the fast subsequent binding of actin monomers or, in the case of the DNA, the fast subsequent photobleaching of two dyes.

3.4 Simulations of Protein Assembly

Monte Carlo simulations of protein assembly were performed in order to test the newly developed as well as the classical analysis tools on a defined system. By applying different analysis methods on the simulated traces, these methods could be compared in terms of their effectiveness in extracting the underlying nucleation mechanism. The analysis tools were tested on their capability to extract the simulated kinetics for the individual association and dissociation

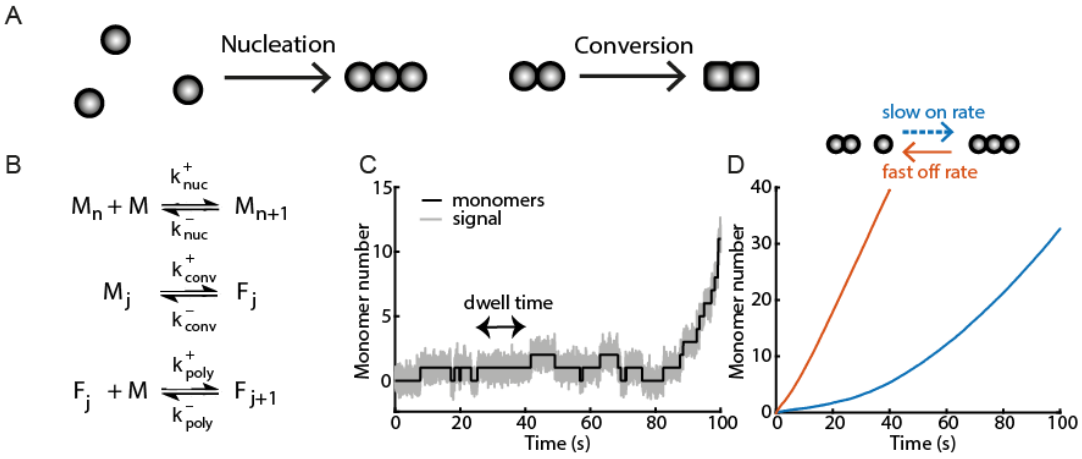

FIGURE 3.6: Simulations of protein self-assembly. A: The simulations assumed either a nucleation-elongation mechanism or a conversion mechanism. B: During nucleation-elongation, slow on rates k^+_{nuc} or fast off rates k^-_{nuc} were assumed until the nucleus size was reached. For a conversion mechanism, only one slow step with a slow k^+_{conv} or a fast k^-_{conv} was simulated. After the nucleus size had been reached, polymerization with k^+_{poly} and k^-_{poly} occurred. C: An example trace of the simulated assembly process. The oligomer size fluctuates around small numbers until the nucleus size is reached. Subsequently, fast polymerization occurs. D: Whether slow on-rates or fast off-rates were simulated during nucleation has an effect on the average growth behavior of the traces.

steps as well as their capability to detect, in general, a nucleation-elongation mechanism or a conversion step occurring during nucleation (Fig. 3.6 A). In addition, simulations using literature kinetic values were used to compare them to the experimental results.

I simulated individual monomer traces with individual kinetic rates for each oligomer size. The association and dissociation rates were given as input parameters. The oligomer number at the start was set to 0. The dwell time for the addition of the first monomer was drawn randomly from an exponential distribution of dwell times corresponding to the inverse of the given association rate for the first monomer. When the oligomer size was not 0, also a dissociation event could occur. In this case, the event with the shorter randomly drawn dwell time would occur. The simulations are based on a Gillespie algorithm, meaning that the simulated time jumps directly to the next event, which is much faster than checking at every time point whether an event takes place.

In this way, thousands of individual oligomer size versus time traces are simulated. Based on the association and dissociation events, a monomer number versus time trace was built with a sampling rate of 100 s^{-1}, unless

otherwise stated. The kinetics prior to reaching the nucleus size were defined by the monomer association rate k^+_{nuc} and the dissociation rate k^-_{nuc} (Fig. 3.6 B). When the monomer number reached the nucleus size, kinetics changed to the polymerization rates k^+_{poly} and k^-_{poly}. When not a nucleation mechanism was simulated, but a conversion step as the bottleneck for polymerization (chapter 2), the conversion step was simulated accordingly, but here only one step was simulated with the slower kinetics k^+_{conv} and k^-_{conv}. If not otherwise stated, k^+_{poly} was 1 s^{-1} and k^-_{poly} was 0.1 s^{-1}, which corresponds to a factor of 1/100 times the sampling rate of 1/10 ms. The sampling rate is the inverse of the time between two data points on the monomer number versus time trace, i.e. the "measurement time". For the slower nucleation kinetics, either the dissociation rates can be enhanced, or the association rates can be slowed down relative to the polymerization kinetics. It has been assumed that the association rate constants do not change during a nucleation process due to the diffusion limited nature of the association reaction (Powers and Powers, 2006). However, I looked into the effect of changing the association rates as well, since some proteins were shown to polymerize on the timescale of hours and thus are not in the diffusion-limited regime (Sabaté, Gallardo, and Estelrich, 2005). Thus, for k^+_{nuc} and k^+_{conv}, I chose values that corresponded to 10%, 50% or 80% of k^+_{poly} to test the sensitivity of the analysis methods to detect slight changes in the kinetics. Accordingly, I chose k^-_{nuc} and k^-_{conv} to be a factor of 2, 5, or 10 faster than k^+_{poly}.

The results of the simulated assembly process were transformed into monomer number versus time traces and overlaid with Gaussian noise to be more comparable with experimental data, whose SNR is in the same regime (Fig. 3.6 C). Additional parameters to the input rates are the sampling time, the labeling efficiency of the monomers and the SNR of the Gaussian noise that is added on top of the monomer-time trace, as well as the total simulated time. Furthermore, photobleaching was added to the traces to study the effect on the analysis tools. I used the single filament traces as well as the average of 1000 traces from individual simulations.

3.4.1 Labeling Efficiency

For the imaging of filament assembly in ZMW or TIRFM, fluorescent labeling of the monomers is essential and adds complexity to the analysis. Dependent on whether a stochastic or a specific labeling strategy is used (see chapter 2),

the distribution of labels per monomer either shows a Poisson distribution where there may be more than one dye per monomer, or each monomer is attached to either zero or one fluorophore as the result of specific labeling. Although high labeling efficiencies are possible in some cases (Lavergne et al., 2016), sample preparation can be very time intensive. Furthermore, high labeling efficiencies can alter the biological function of the proteins. Therefore, it is sometimes necessary to use a mixture of labeled and unlabeled monomers to study the assembly process. As fluorescence measurements only detect the labeled molecules, the labeling efficiency needs to be accounted for in the analysis, when protein labeling is not specific with 100% efficiency.

To test the influence of different labeling strategies with the respective labeling efficiencies, the monomer number trace was modified with a Poisson distribution of different labeling efficiencies from 0.3 to 3 (stochastic labeling), or with a Bernoulli distribution with labeling efficiencies from 0.3 to 1 (incomplete specific labeling). In the case of stochastic labeling with labeling efficiencies of more than 1, the step size of a single step was still assumed to be 1. Since for the simulations, no double-step correction was applied except otherwise indicated, this leads to a treatment of the steps with double or triple step sizes as one monomer addition step in accordance to the simulated process. Experimentally, using stochastic labeling, the difficulty lies in distinguishing two subsequent fast monomer additions from a monomer with two labels, as described in chapter 2.

3.4.2 Addition of Photobleaching

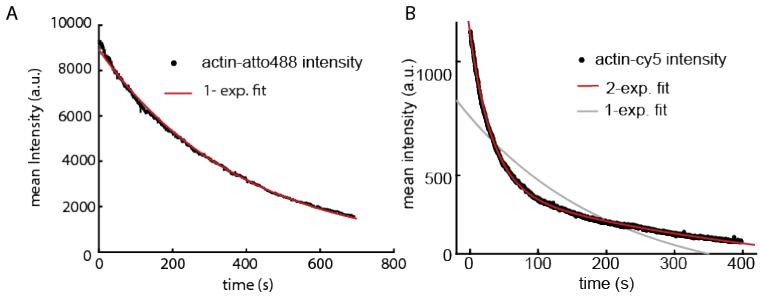

FIGURE 3.7: Photobleaching rate of stabilized filaments measured in ZMW. 1 μM actin was incubated for 1.5 h and stabilized with phalloidin to prevent dissociation. Black: the mean fluorescence intensity decay from about 600 traces. A: Photobleaching of actin-atto488. Red: an exponential fit with a decay constant of k = 0.003 s^{-1}. B: Photobleaching of actin-Cy5. A single exponential fit (grey) does not describe the data, but a double-exponential decay (red) does. The decay constants are 0.025 s^{-1} and 0.0015 s^{-1}.

Another artifact of the measurements that has an impact on the analysis is the photobleaching of dye molecules. Although photobleaching can be reduced by the use of oxygen scavenging systems (see chapter 2), it will always affect the intensity signal dependent on the photobleaching rate. In intensity traces, a photobleaching step is indistinguishable from a dissociation step. This hinders not only the direct measurement of the dissociation rate, but also leads over time to a mismatch between the intensity level and the monomer number. This, in turn, affects the analysis of the association rates.

To test the influence of photobleaching, I introduced down steps in the simulations based on different photobleaching rates. These rates are in the regime of experimentally determined values for atto488 and Cy5 measured in ZMW (Fig. 3.7). If a monomer dissociates after photobleaching, no down step is introduced. If not indicated otherwise, photobleaching was studied on simulations using 100% specifically labeled monomers. In the case of actin-Cy5, the photobleaching rate showed a double exponential decay as expected for Cy5 (Füreder-Kitzmüller et al., 2005).

3.4.3 Simulations of actin polymerization

For simulations of actin elongation, the following reference values from the literature were used: binding of the first actin monomer to gelsolin is 0.025 $\mu M^{-1}s^{-1}$ at pH 7.0 (Selve and Wegner, 1987). Binding of the second actin monomer to gelsolin-actin complex is 40 times faster than binding of the first actin monomer (0.8 $\mu M^{-1}s^{-1}$) (Selve and Wegner, 1987). Dissociation of the second actin monomer (i.e. Gelsolin-$(actin)_2$ to Gelsolin-$(actin)_1$) is 0.02 s^{-1} (Schoepper and Wegner, 1991). The estimated pointed-end k_{on} from Gelsolin-$(actin)_2$ onwards is 0.12 $\mu M^{-1}s^{-1}$ (Brangbour et al., 2011). Assuming a critical concentration of 0.6 μM, the pointed-end k_{off} is 0.07 s^{-1}. I also tried using different values for pointed-end kinetics (k_{on} = 0.5 $\mu M^{-1}s^{-1}$, k_{off} = 0.32s^{-1} (Ditsch and Wegner, 1994) and k_{on} = 1.3 $\mu M^{-1}s^{-1}$, k_{off} = 0.8 s^{-1} (Pollard, 1986)). However, simulations using these values were not comparable to the experimentally observed findings.

3.5 Dwell-time Analysis

The kinetic rates for each single association step were determined by fitting the dwell-time distribution for each step with a single-exponential decay

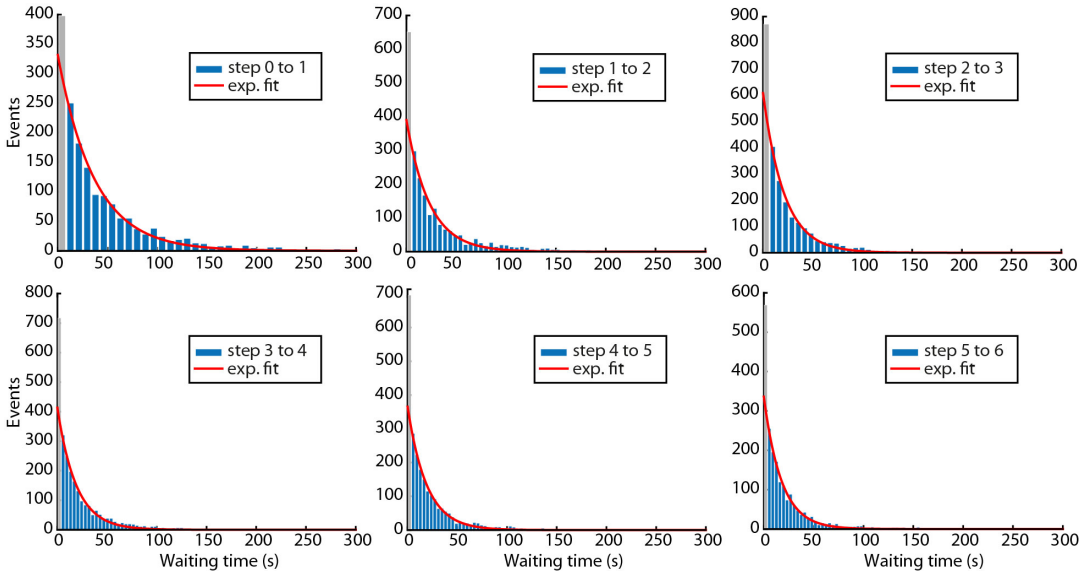

FIGURE 3.8: Experimentally obtained association rates are single-exponentially distributed. Waiting times (blue) and exponential fits (red) of the first to the sixth binding events of actin-atto488 on gelsolin measured inside ZMW. The first bins (grey) contain an artifact of the double-step correction and were not included in the fits.

(Fig. 3.8 A). The dwell times are defined as the total time spent at a particular monomer number n until the next monomer $n+1$ arrives (Fig. 3.6). For experimental data, the dwell time histograms generally showed good statistics until the sixth association step. Beyond this step, the statistics were poorer as only traces that have not displayed a down step before were considered. Down steps could disturb the relationship between intensity and monomer number, since they can be the result of dissociation events or photobleaching events.

When a double-step correction was used, the inserted additional steps were assigned a dwell time that corresponded to the sampling time during the measurement. Therefore, the first bin in the waiting time distribution shows more events than what would be expected according to a mono-exponential distribution (grey bins in Fig. 3.8). The events in that first bin are a combination of fast subsequent event happening during the sampling time, dimer or oligomer binding events and double-labeled monomers. For the exponential fit of the dwell-time distribution, the first bin was not included.

For determining dissociation rates in experimental data, the dwell-time distribution could not be used because of the presence of photobleaching. However, there are other analysis methods that show the effect of a change in the dissociation rates better, or even can estimate the underlying dissociation rates if

the photobleaching rate is known. These methods are described below. For data obtained by simulations, the dissociation rates were obtained in the same manner as the association rates as there is no photobleaching.

3.6 Visitation Analysis

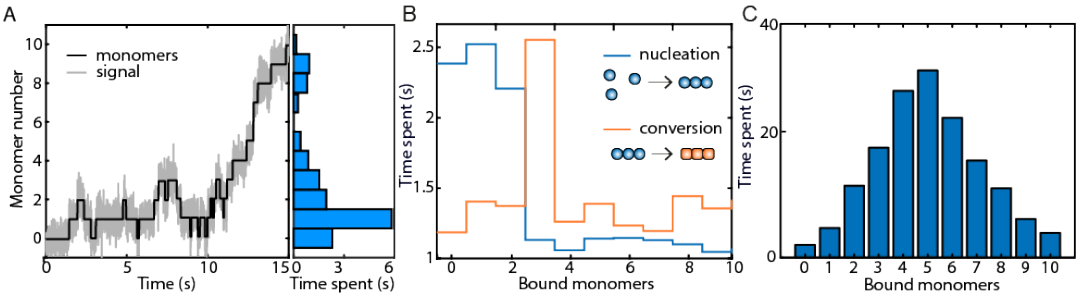

FIGURE 3.9: A: Example trace of a simulated growth process undergoing a nucleation event at a nucleus size of four monomers (black) with Gaussian noise (grey). The distribution of time spent at a certain oligomer size (blue histogram) contains information about the nucleation mechanism, when it is applied to many single oligomer traces (B). B: The visitation analysis can distinguish between a nucleation and a conversion mechanism as well as the nucleus size for nucleation (blue) or conversion (yellow). Visitation analysis on ZMW measurements of actin-Cy5 growing on cappuccino 300 s after addition of monomers to the ZMW. The Cy5 labeling efficiency was 30%.

As an alternative to the dwell-time analysis, I developed the visitation analysis tools to investigate the microscopic mechanisms underlying filament formation. The visitation analysis calculates the time that each oligomer or filament spends with n bound monomers (n = 0,1,2...) and generates a histogram (Fig. 3.9 A). When applied to many oligomers, the result reflects the kinetic changes during the nucleation process and slow or dynamic steps are directly visible (Fig. 3.9 B). For example, a protein assembling via a nucleation-elongation mechanism is characterized by many small oligomers that form and immediately disassemble. In this mechanism, the oligomers spend a considerable amount of time below the nucleus level, which is directly visible in the visitation analysis (Fig. 3.9 B blue line). For a conversion mechanism, stable oligomers are formed that grow after a slow conversion step at a particular oligomer size (Fig. 3.9 B orange line). The visitation analysis was evaluated to be better suited than the dwell-time analysis to detect changes in the kinetics from nucleation to polymerization, even if only a single step shows different kinetics.

For experimental data, to investigate how the oligomer size distribution changes during the course of the experiment, the 800 s traces were divided into 6 time intervals. For each time interval, the total time an oligomer spent having a particular number of monomers was calculated (Fig. 3.9 C for one time interval).

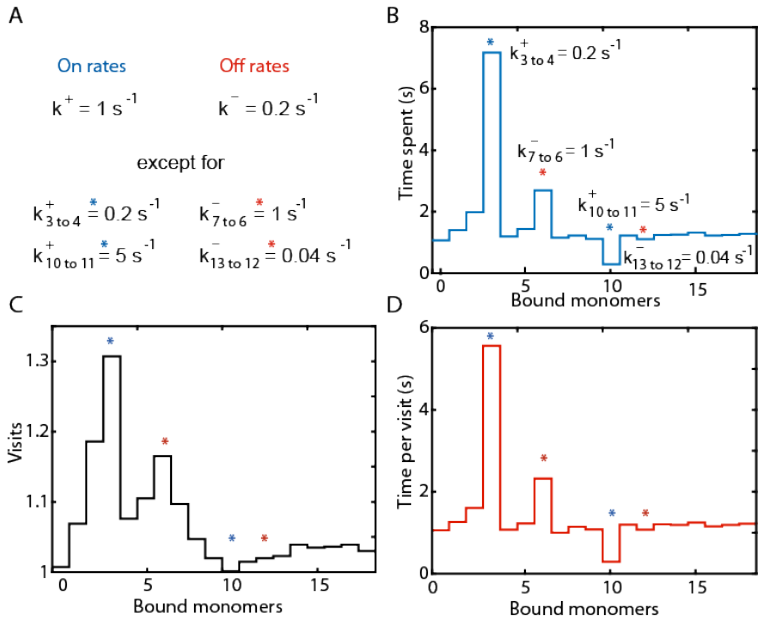

FIGURE 3.10: Visitation analysis on a growth process with single steps of different kinetics. A: the simulated growth process. All monomer binding events have an on rate $k^+ = 1s^{-1}$, all dissociation events an off-rate of $k^- = 0.2s^{-1}$. The third and 10th monomer binding event show a slower or a faster on-rate, respectively (by a factor of five, except for k^-_{13to12}) and are marked by blue stars. The 7th and 13th show a faster or slower off rate, respectively, and are marked by red stars. B-D: The visitation can resolve multiple single steps with different kinetics.

Because the visitation analysis showed a high potential to detect individual steps with faster or slower kinetics, I simulated a hypothetic growth mechanism with individual slower or faster steps in between (Fig. 3.10). The association rate is 1 s^{-1}, and the dissociation rate is 0.2 s^{-1}, except for the steps 3 to 4, 7 to 6, 10 to 11 and 13 to 12, which show association and dissociation rates as indicated in Fig. 3.10 A. Until the 11^{th} step, these individual steps are directly visible in the visitation analysis for both faster and slower steps (Fig. 3.10 B). As an alternative to calculating the mean time the oligomers spend at each monomer number, the number of visits per step (Fig. 3.10 C) or the time per visit were calculated (Fig. 3.10 D). The number of visits visualizes the dynamics around steps with a faster association rate or dissociation rate.

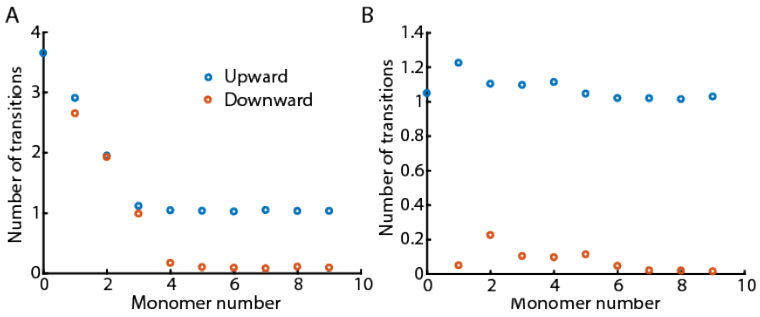

FIGURE 3.11: Upward and downward transition between steps. The number of transitions was calculated for (A) a nucleation-elongation mechanism and (B) the hypothetic growth process as depicted in Fig. 3.10 A.

Additionally, the number of upward and downward transitions between each monomer number can be calculated (Fig. 3.11). During a nucleation process or around a conversion site, the oligomers fluctuate around the rate-limiting steps until the nucleus size is reached or the necessary rearrangement has occurred. This approach is not suited for detecting single steps with different kinetics, but can visualize the nucleation mechanism.

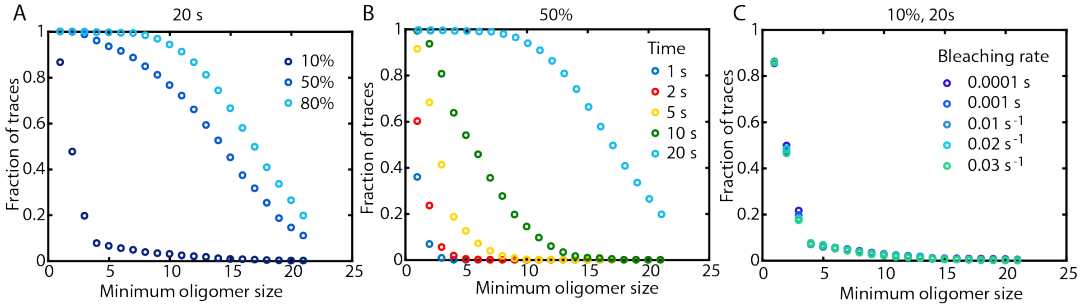

FIGURE 3.12: Statistics of filament growth. Fraction of traces that reach a certain oligomer size for a nucleation process where k^+_{nuc} is at 10, 50 or 80% of k^+_{poly}. A: Total time of the simulation is 20 s. B: The effect of the measurement time for k^+_{nuc} at 50% of k^+_{poly}. C: The influence of photobleaching for a total time of 20 s and k^+_{nuc} set to 10% of k^+_{poly}.

Finally, with the conversion of intensity to monomer number, also the fraction of oligomers reaching a certain oligomer size can be calculated (Fig. 3.12). Depending on the difference in the rates between nucleation and elongation phase (k^+_{nuc} and k^+_{poly}), different results are obtained (Fig. 3.12 A). Also, the total measurement time has a very strong effect on this analysis approach Fig. 3.12 B), whereas the effect of photobleaching on the apparent monomer number cannot be visualized (Fig. 3.12 C).

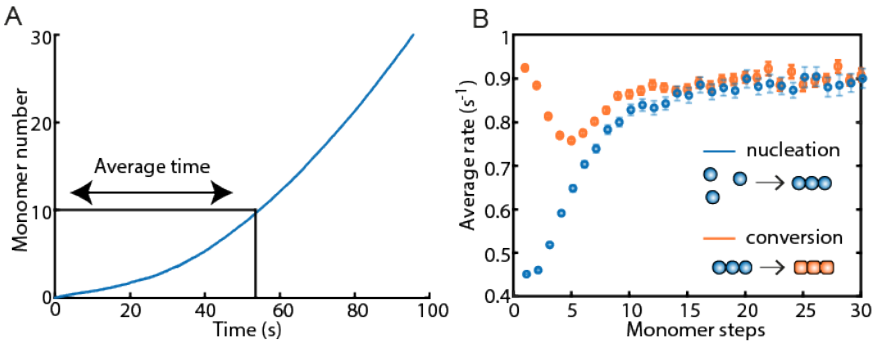

FIGURE 3.13: Average rates analysis. From the average trace of many individual filaments growing from the same starting point, average rates can be calculated from the average time it takes to reach an oligomer size of 1, 2, 3... (A). When plotted versus the monomer number (oligomer size), different nucleation mechanisms show individual signatures (B).

3.7 Average Rates

When statistics are sufficient, i.e. in the range of several hundred intensity versus time traces of oligomer growth, the intensity can be pooled together to calculate a mean intensity or monomer increase (Fig. 3.13 A). The difference to bulk measurements lies in the defined starting point of the growth process and the inhibition of interactions between the measured oligomers. When the mean intensity step size of for the addition of a single monomer is known, the average rates for each association step can be calculated. Average rates are defined as the inverse of the time it takes to reach the intensity level corresponding to 1 monomer, or from 1 to 2 monomers, and so forth (Fig. 3.13 A). These average rates are then plotted as a function of oligomer size (Fig. 3.13 B).

For many oligomers that started growing at the same time, a nucleation mechanism is directly visible in the shape of the averaged intensity curve (Fig. 3.13 A). Similar to the visitation analysis, the average rate analysis also reveals signatures that can be clearly associated with either a nucleation-elongation (Fig. 3.13 B blue points) or a conversion mechanism (Fig. 3.13 B orange points). Nucleation-elongation starts from a low average rate and increases monotonically until it reaches the average elongation rate. The average rate from a conversion mechanism first drops and then increases until it also reaches the average elongation rate.

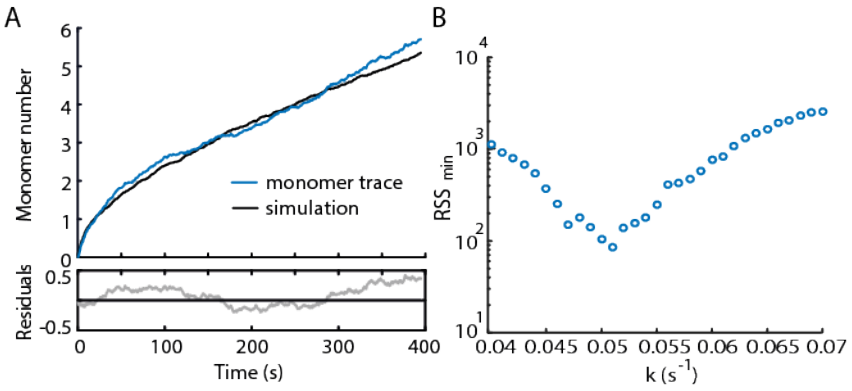

FIGURE 3.14: Offrate estimation exemplified on ZMW measurements of actin-Cy5 growing on cappuccino. The Cy5 labeling efficiency was 30%. A: Average monomer number trace of 600 traces (blue) and the average monomer number trace of 2000 simulations using the measured association rates and one dissociation rate for all steps. B: The residual sum of squares (RSS) error for the comparison between experiment and simulation shows a minimum at a dissociation rate of 0.051 s^{-1}.

3.8 Off-rate Estimation

As already mentioned, a direct calculation of the dissociation rates from the dwell-time distributions of the down steps is not possible due to photobleaching. But even when photobleaching is absent, the extraction of dissociation rates was evaluated to be problematic using simulations (see chapter 4). With a faster association rate, the dwell-time distribution of the dissociation steps is always shifted towards faster values, which makes an unbiased estimation of the dissociation rates impossible.

An indirect way to estimate the off rates of single dissociation events is to simulate a growth process with the same association rates as experimentally determined via the dwell-time analysis, while adjusting the dissociation rate and considering the measured photobleaching rate (Fig. 3.14 A). For a comparison between measurement and experiment, the average trace of about 600 experimental traces or 2000 simulated traces was used. The simulation was run with different dissociation rates until a minimum in the error between simulation and experiment was reached (Fig. 3.14 B). As an error estimation, the residual sum of squares was used (RSS). The process was started with the most simple approach, i.e. the dissociation rate was the same for all steps. Only when this model does not give a good agreement, more detailed models allow two or more different dissociation rates, for example a faster one during the nucleation regime and a lower one during polymerization. The off-rate estimation was developed by Alvaro H. Crevenna, PhD.

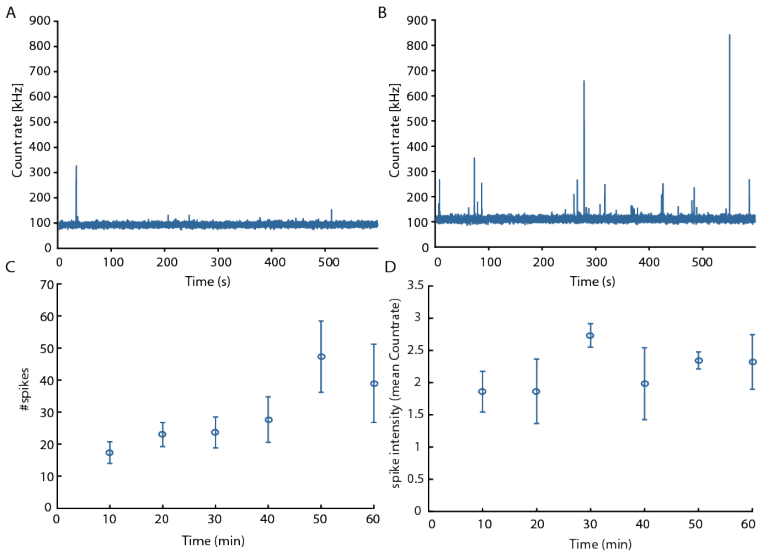

FIGURE 3.15: A spike analysis of FCS data to monitor actin oligomerization. A, B: Countrate of 100 nM actin-atto488 after 1 h incubation without (A) and with (B) 10x excess of MiuA. C: The number of spikes in 10 min time intervals extracted for measurements of 100 nM actin with 10x excess of MiuA. D: The intensity of spikes, quantified using the mode of the countrate of the individual measurements. Errorbars represent the standard error of the mean of three independent measurements.

3.9 Analysis of FCS Data

Another approach to measure protein oligomerization is to use fluorescence correlation spectroscopy. Here, freely diffusing labeled monomers are measured and the oligomerization process is visible in the autocorrelation funcion (ACF) or in the countrate directly, depending on the size of the oligomers.

When measuring a freely diffusing monomeric species, the intensity is uniformly distributed around a mean value (Fig. 3.15 A base line). However, when oligomerization occurs, the oligomers are visible as spikes in the intensity (Fig. 3.15 B) as the increased number of dyes on the oligomers significantly surpasses the stochastical fluctuations of freely diffusing monomers in the observation volume. When oligomerization continues, this results in an increased number of spikes over time (Fig. 3.15 C) as well as an increased height in the intensity of the spikes (Fig. 3.15 D). An intensity peak was considered to be a spike when the intensity was higher than the mean countrate of the measurement plus 4 times the standard deviation. The spike intensity was quantified in units of the mean count-rate of the measurement. This "spikeness" can be used to analyze protein oligomerization (Crevenna et al., 2013).

Additionally, the oligomerization is visible in the autocorrelation curve due to the slower diffusion of the oligomers (chapter 5). For the calculation of the autocorrelation function, large oligomers that resulted in spikes have been removed. Large oligomers of different sizes have a pronounced effect on the diffusion part of the ACF that is problematic to analyze because of the low statistics of the spikes in comparison to the measured countrates around the mean value. For higher concentrations of actin, a fit of the FCS curve could only be obtained when the curve was cut off at 10 to 100 μs due to the complexity of the system as discussed in chapter 5. ACF curves were plotted using PAM (PIE analysis with Matlab) (Schrimpf et al., 2018).

Chapter 4

Analysis Methods for Investigating Protein Aggregation

4.1 Introduction

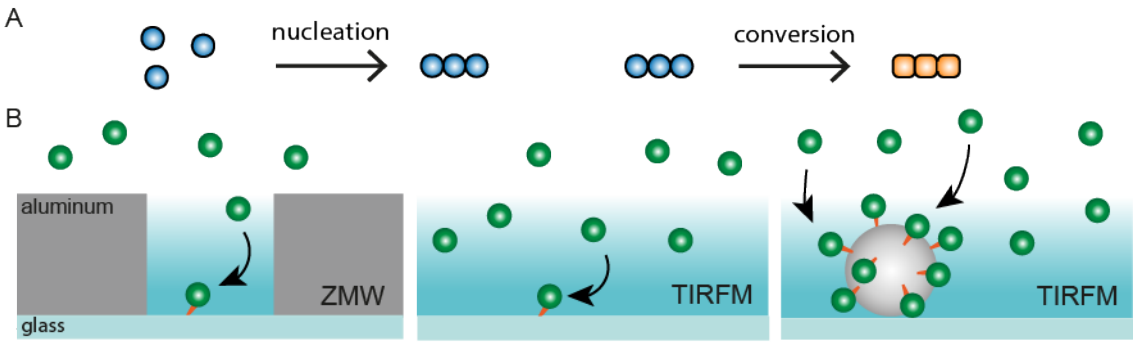

FIGURE 4.1: Methods for collecting single-filament data of protein self-assembly. A: Two major mechanisms are depicted for the initiation of oligomerization. During primary nucleation, either a one-step nucleation process can occur, or a conversion step is necessary with a rearrangement of the oligomers prior to further growth. B: Single-oligomer data of the early steps during nucleation can be obtained using ZMW, or TIRFM when the required concentrations are sufficiently low. In TIRFM, many oligomers growing at the same time yield average, but synchronized information of the growth process (right panel). Spontaneous oligomerization in solution is not measured.

Despite the recent advances in our understanding of protein self-assembly processes, many of the details during the early nucleation phases of polymerization remain unknown. Of the various methods available, single molecule techniques are a promising route since they could provide direct, real-time measurements of single monomer association and dissociation events occurring during the growth process (Andrecka et al., 2016; Hoyer et al., 2018). In particular, single molecule fluorescence techniques in combination with ZMW

or TIRFM (Levene et al., 2003) have opened the possibility to directly observe the early stages in oligomer assembly (Fig. 4.1 B). This is particularly useful as the various steps occur spontaneously over potentially different pathways, making synchronisation impossible.

Aside from single-molecule techniques information about the growth process can also be obtained from the average information of filament growth measured on many surface-bound nucleator proteins, for example by using TIRFM (Liang, Lynn, and Berland, 2009), circular dichroism (Uratani, Asakura, and Imahori, 1972) or other spectroscopy methods (Kirkitadze, Condron, and Teplow, 2001; Zhai et al., 2012; Ramachandran et al., 2014). Only filaments growing on the surface-bound nucleator protein of interest are measured, excluding spontaneous oligomerization events occurring in solution (Fig. 4.1, in the case of TIRFM, the evanescent field and the fast diffusion exclude the measurement of oligomers in solution). This makes it possible to synchronize the starting point of the oligomerization process.

By using single molecule techniques, binding events are visualized as step-wise signal increases over time, whereas dissociations correspond to step-wise downward transitions (see chapter 3). In an often used approach to data analysis, the residence time at each monomer number is pooled together for all monomer numbers. This method is normally referred to as a dwell-time analysis and has been used for many applications in biophysics (Szoszkiewicz et al., 2008). The dwell-time analysis can determine each microscopic rate and therefore reveal the unique underlying mechanism. However, the analysis accuracy depends, and by extension that of identifying the nucleation mechanism, on sufficient sampling and data quality. For example, to accurately estimate the rate of a single transition, a sampling rate of at least ten times the rate to be estimated is required as will be shown later. For some techniques such as optical tweezers, the sampling frequency is not a problem as it is only dictated by the readout speed of a position sensitive detector. For fluorescent samples, high sampling frequency comes at the expense of increasing the probability of photobleaching, which shortens the achievable measurement time.

Most primary nucleation studied so far has been classified to occur either through a nucleation-elongation mechanism or through a conversion mechanism (Fig. 4.1 A) (Meisl et al., 2016). I simulated first a one-step nucleation mechanism, i.e. the formation of a nucleus of defined size (n monomers) that

represents the smallest stable structure and allows subsequent polymerization (Fig. 4.1 A). Hereby, every monomer binding event until the formation of the nucleus is defined by the nucleation kinetics and the faster polymerization kinetics take effect after the nucleus size has been reached. For a simulation of the kinetics during nucleation prior to polymerization, either the dissociation rate constants of the single monomers can be enhanced, or the association rate constants can be slowed down. It has been assumed that the association rate constants do not change during a nucleation process due to the diffusion limited nature of the association reaction (Powers and Powers, 2006). However, I looked into the effect of changing the association rates as well, since some proteins were shown to polymerize on the timescale of hours and thus are not in the diffusion-limited regime (Sabaté, Gallardo, and Estelrich, 2005; Powers and Powers, 2006).

In some cases, a rearrangement of the oligomer occurs, leading to a single conversion step with different kinetics (Fig. 4.1 A right side). Therefore, I tested the analysis methods both for their ability to detect a transition from nucleation-governed kinetics to faster polymerization, as well as for their ability to detect a single conversion step.

This chapter describes the development and testing of the analysis methods for kinetic data of filament growth on the single oligomer level as well as for averaged, but synchronized filament growth. The analysis methods have been described in chapter 3. The objective is to i) recover the correct on- and off-rates of single monomer addition and dissociation events, and ii) recover the correct assembly mechanism, i.e. the relative differences between monomer binding events at different oligomer sizes. To that aim, I simulated growth processes of single oligomers with defined binding and dissociation rates of the monomers, dependent on the oligomer size at the time of the binding or dissociation event. Thereby, two main mechanisms were distinguished: a nucleation mechanism with a slow on-rate or high off-rate in the beginning until the polymerization phase is reached, and a conversion mechanism where a single slow on-rate or high off-rate defines a bottleneck for successful polymerization.

To test the robustness of the analysis tools, I introduced changes in the SNR, the simulated measurement rate and the relative difference between the nucleation and polymerization kinetics. Furthermore, since measurements in ZMW and TIRFM depend on dye-labeled monomers, I looked into the distribution of labels per monomer (i.e. the labeling efficiency), as well as the

photobleaching of fluorescent labels.

4.2 Materials and Methods

Simulations and analyses have been employed as described in chapter 3. In short, in the simulations, a step-wise growing oligomer starting from 0 monomers was built up according to the main input parameters; the association and the dissociation rate. During the nucleation phase until the assembly of the critical nucleus, the association rate was slowed down or the dissociation rate was accelerated in comparison to the polymerization kinetics. If not otherwise stated, k^+_{poly} was 1 s^{-1}, k^-_{poly} was 0.1 s^{-1}, which corresponds to a factor of 1/100 times the simulated sampling rate of 100 s^{-1}. The chosen kinetics are in the same range as pointed-end actin polymerization rates (Pollard, 1986). For k^+_{nuc} during the nucleation phase and k^+_{conv} for a single conversion step, I chose values that corresponded to 10%, 50% or 80% of k^+_{poly}. Accordingly, I chose k^-_{nuc} and k^-_{conv} to be a factor of 2, 5, or 10 faster than k^+_{poly}. The simulated monomer trace versus time was overlaid with Gaussian noise with a SNR of 2, if not otherwise stated. Then, to treat the simulated traces like the experimentally measured traces, the Salapaka step-finding algorithm extracted the monomer trace back and further analyses (dwell-time analysis, visitation analysis and average rate analysis) were performed. I analyzed single filament traces as well as the average of 1000 traces from individual simulations for the average rate analysis.

Looking at the relative difference between the expected rates of the chosen biological system and the sampling rate, the results can be used to estimate the necessary sampling rate for any experiment of this kind, or when the sampling rate is given, estimate if the extracted rates are trustworthy.

To test the analysis methods, changes in the sampling rate, the SNR and the respective difference between nucleation or conversion, and polymerization kinetics have been simulated. Furthermore, the effect of labeling efficiency and photobleaching was studied.

4.3 Results

Dwell-time Analysis First, I applied a classical dwell-time analysis to the monomer number versus time data that resulted from the step-finding algorithm. The on- and off-rates were extracted from an exponential fit of the dwell-time distribution (Fig. 4.2 A, B) and plotted against the monomer number to visualize the transition from nucleation to polymerization that occurs once the nucleus size has been reached (Fig. 4.2 C-D). While a change in the association rates from nucleation to polymerization was directly visible and allowed the determination of the nucleus size (Fig. 4.2 C), the dissociation rates did not reflect the simulated change in kinetics (Fig. 4.2 D). When applied to a growth process with a single conversion step, the dwell-time analysis could only identify single steps with a large change in the on-rate (Fig. 4.2 E). Changes in the off-rate and fast steps were likely to be overseen (Fig. 4.2 F).

The dwell-time analysis was able to detect differences in the association rates when the difference was at least a factor 2 (Fig. 4.3 A, B). Regarding the measurement conditions, a high sampling time and a high SNR are required (Fig. 4.3 C-H). A low SNR leads to slower apparent on-rates as fast steps are likely to be overseen, which was also reflected in the dwell-time distribution (Fig. 4.3 C). A slow sampling time lead to an apparently wrong nucleation or conversion step (Fig. 4.3 G). This could be improved by incorporating a double-step correction. For the dwell-time analysis at slow sampling rates, a double-step correction was used (see chapter 3 for details). With slow sampling, fast individual steps could not be resolved and appeared as a step with higher step size. For the double step correction, the mean step size per trace was calculated. An up or down step with a step size twice or three times the mean step size was treated as two or three monomers, respectively. The additional steps were assigned a dwell time that corresponded to the sampling time.

The testing of the requirements of the measurement for reliable use of the dwell-time analysis showed that it is very sensitive towards SNR, sampling rate and the relative difference between the different association rates. Therefore, results from a dwell-time analysis should be interpreted very carefully.

Visitation Analysis To overcome the poor sensitivity of the dwell-time analysis towards changes in the dissociation rates and its little robustness towards

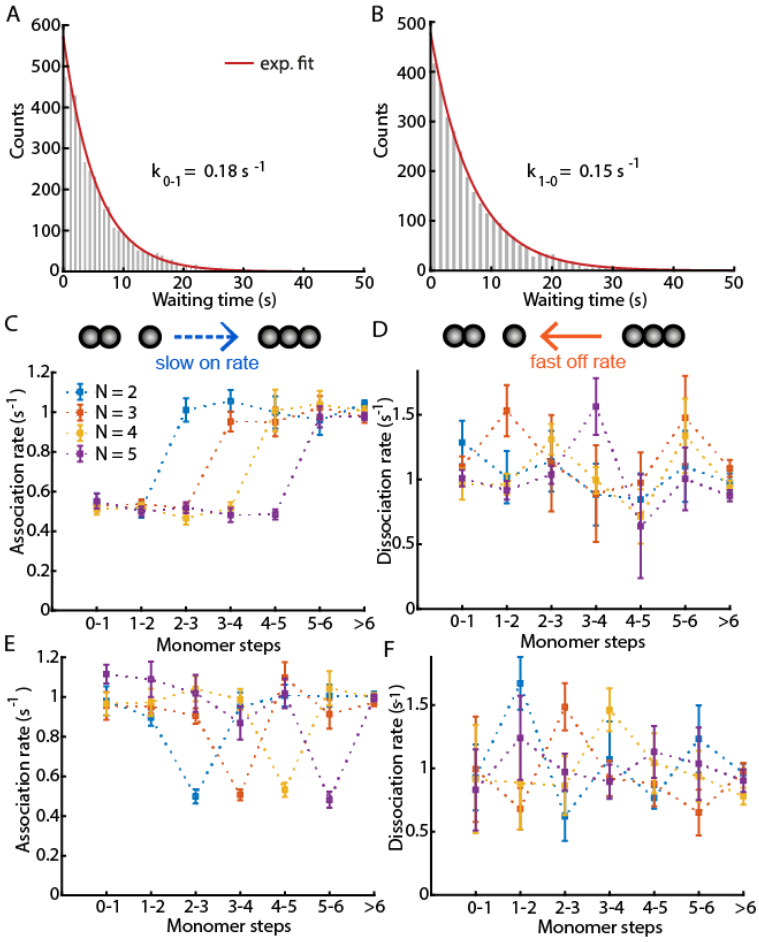

FIGURE 4.2: Dwell-time analysis on an assembly process with a conversion step at 2, 3, 4 or 5 monomers. A, B: the dwell-time distributions for the first association step (A) and the first dissociation step (B) are shown. The dwell-time distribution for each individual step was fitted with a single-exponential distribution. C, E: The extracted association rates for a nucleation (C) and a conversion mechanism (E) with different nucleation or conversion sizes. The dwell-time analysis is able to identify the association rates for the individual steps. The association rates during nucleation k^{+}_{nuc} were at 50% of k^{+}_{poly} with no change in the off-rates. D, F: The extracted dissociation rates for a nucleation (C) and a conversion mechanism (E) with different nucleation or conversion sizes. The dwell-time analysis could not identify the dissociation rate changes during the nucleation or conversion steps. The dissociation rates during nucleation k^{-}_{nuc} were at 5x of k^{-}_{poly} with no change in the on-rates. Errorbars for the rates represent the 95% confidence intervals of the exponential fits.

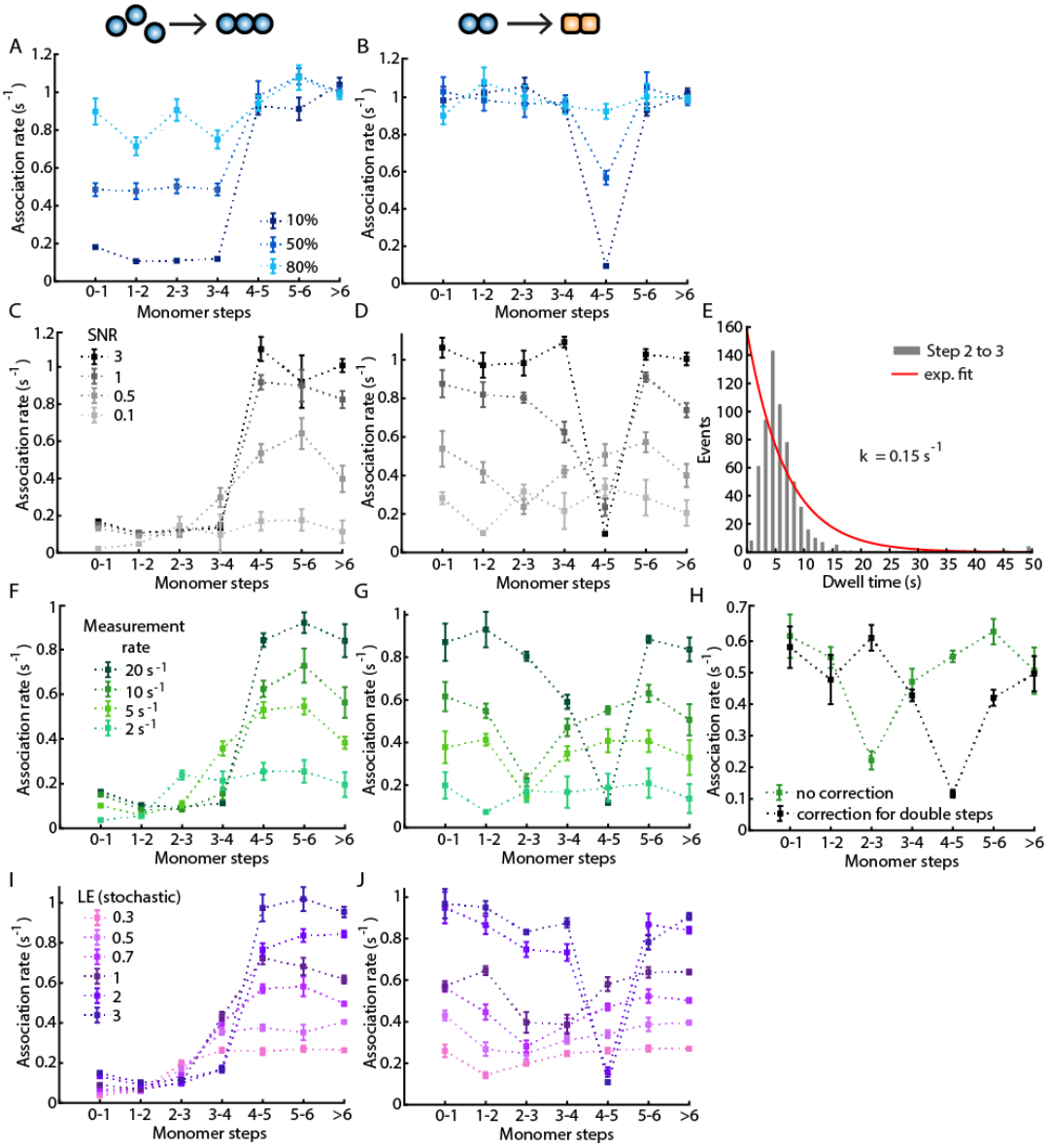

FIGURE 4.3: Robustness of the dwell-time analysis. For all simulations, a nucleus or conversion step at four mononomers was chosen. A, B: Extracted on-rates for simulations varying the difference between nucleation and polymerization kinetics. The association rates k^{+}_{nuc} and k^{+}_{conv} were chosen to be 10, 50 or 80% of k^{+}_{poly}. C, D: Extracted on-rates for simulations applying different SNRs. A nucleation mechanism (C) or a slow conversion step (D) can be detected until a SNR of 1. E: With low SNR, fast steps are not detected and the dwell-time distribution does not follow an exponential decay (red line). F, G: Extracted on-rates for simulations varying the sampling time. To estimate association rates, the measurement rates should be at least 10x faster than the fastest rate. H: By using a correction for fast subsequent steps that appear as single steps, the correct conversion step can be determined despite a measurement rate of 10 s^{-1} or 10x slower than the sampling rate. I, J: Extracted on-rates for simulations of monomers with different degrees of labeling. A high labeling efficiency (LE) is needed for correct interpretation of the dwell-time analysis. For stochastic labeling, the LE should ideally be more than 100%.

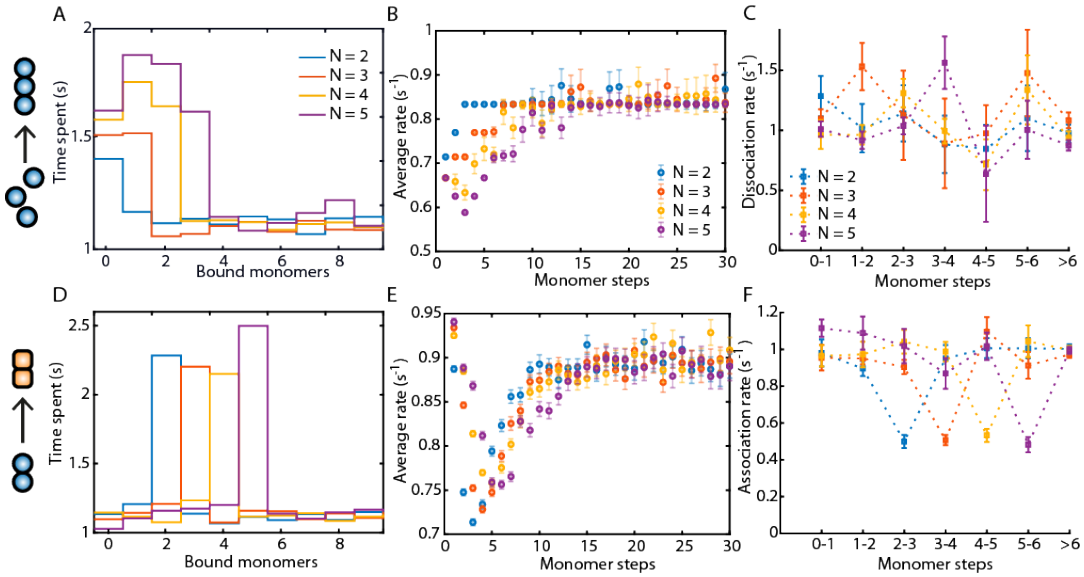

FIGURE 4.4: A comparison of the visitation analysis, average rates and dwell-time analysis on an assembly process with nucleus site at 2, 3, 4 or 5 monomers. A, D: A visitation analysis on a nucleation mechanism with slower off-rates during the nucleation phase (A) and on a conversion mechanism with a slower on-rate on the conversion step (D). B, E: Average rate analysis on the same nucleation and conversion mechanism as in (A, B). C, F: Dwell-time analysis on the same nucleation and conversion mechanism as in (A, B). The dwell-time analysis can identify a mechanism with a change in the on-rate by extracting the association rates (F), but not a mechanism with a change in the off-rate, since the extracted dissociation rates do not indicate any changes in the simulated rates (C). Errorbars for the rates represent the 95% confidence intervals of the exponential fits. The association rates during nucleation k^{+}_{nuc} were chosen to be 50% of k^{+}_{poly} with no change in the off-rates. The dissociation rates during nucleation k^{-}_{nuc} were chosen to be 5x of k^{-}_{poly} with no change in the on-rates.

SNR and the measurement rate (Fig. 4.3), I developed a more direct way to visualize the kinetic transition from the early stages in oligomer formation to the polymerization phase, the visitation analysis. I calculated the mean time the oligomers spent with n bound monomers (see chapter 3). With this analysis, the slower nucleation kinetics were directly visible and the nucleus size could be estimated regardless of whether the association rate or the dissociation rate defined the nucleation mechanism (Fig. 4.4 A) or a single conversion step (Fig. 4.4 D).

For a nucleation-elongation mechanism, polymer growth is determined by the nucleation phase, where initial oligomers form and immediately disassemble due to the high thermodynamic barriers. In this mechanism a single nascent oligomer is observed to spend a considerable amount of time at the nucleus level (Fig. 4.4 A). A filament that polymerizes through a conversion mechanism can be observed to form stable oligomers that do grow after a slow conversion step at a particular monomer number (Fig. 4.4 D). The visitation analysis was able to identify the nucleus size and a conversion point accurately (Fig. 4.4).

Since the visitation analysis was able to detect conversion steps with a high sensitivity, I wanted to further test its ability to detect single steps with different kinetics. To this aim, I simulated a growth process with individual slower or faster steps at defined oligomer sizes (Fig. 4.5 A).

The visitation analysis is sensitive to changes in the on- and off-rates of individual steps even at low SNR and with only slight differences between the rates of the individual steps (Fig. 4.5 B). It was robust towards a SNR as low as 0.5 (Fig. 4.5 C) and a measurement rate of 5 times the default on-rate (Fig. 4.5 D). The addition of photobleaching affects the conversion of steps into monomer number due to the indistinguishability of a dissociation step and a photobleaching step. Therefore, the visitation analysis is sensitive towards photobleaching (Fig. 4.5 E). In contrast, the dwell-time analysis is only able to identify the first change in the on-rate at step 3 to 4 and cannot identify a change in the off-rate at all (Fig. 4.5 F).

Applied to a simulation of a nucleation mechanism, the visitation analysis was even more robust towards SNR, measurement rate, labeling efficiency and photobleaching (Fig. 4.6, table 4.1). The visitation analysis can identify the nucleation regime of the oligomer sizes even at a SNR of 0.1 (Fig. 4.6 C). For

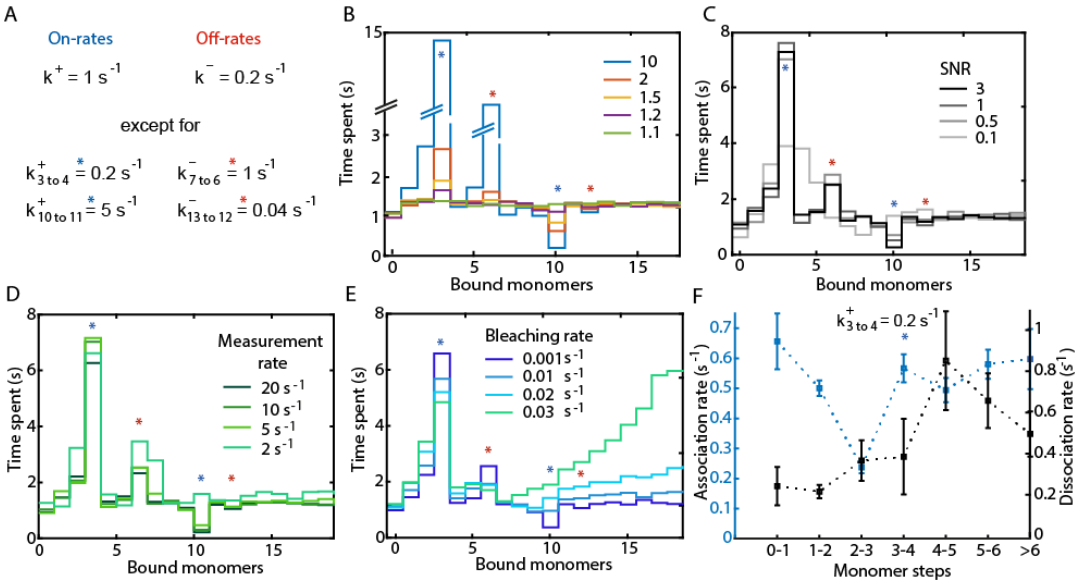

FIGURE 4.5: Reliability of the visitation analysis for a hypothetic growth process. A: depiction of the hypothetic growth process. All steps have a on-rate k^+ of 1 s^{-1} and an off-rate of 0.2 s^{-1}, except for the indicated steps. The given rates are an example of a factor of 5 difference between the single steps and the default rates. B: Varying the difference between the rates of the single steps (indicated by stars as in (A)) and the default rates by different factors. The difference between the single steps with slower or faster kinetics can still be detected at a factor of 1.5. C: Varying the SNR. Individual steps are visible down to an SNR of 0.5. The difference in kinetics was a factor of five as depicted in (A). D: Varying the sampling rate. The visitation analysis is able to detect individual steps at measurement rates down to 5 times the default on-rate. E: Visitation analysis on simulations considering the influence of photobleaching. F: Dwell-time analysis on the same simulated growth process. The dwell-time analysis is not able to resolve multiple individual rates even with a SNR of 2, measurement rate of 20 s^{-1} and no photobleaching.

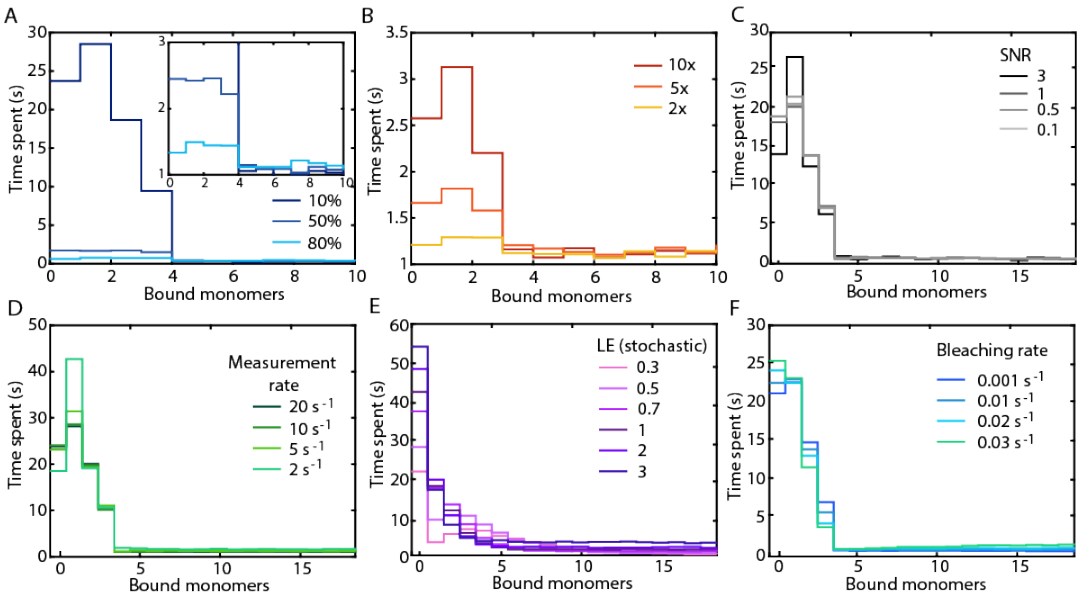

FIGURE 4.6: Robustness of the visitation analysis applied to a nucleation mechanism with a nucleus size of four monomers. A,B: Visitation analysis on simulations varying the difference between nucleation and polymerization kinetics. The association rates during nucleation k^{+}_{nuc} were at 10, 50 or 80% of k^{+}_{poly} (A). The dissociation rates during nucleation k^{-}_{nuc} were a factor of 10, 5 or 2 of k^{-}_{poly} (B). C: Visitation analysis on simulations varying the SNR. A nucleation mechanism can be detected until a SNR of 0.1. D: Visitation analysis on simulations varying the sampling time. The visitation analysis is quite robust towards slow measurement rates. E: Visitation analysis on simulations using monomers with different degrees of stochastic labeling. The labeling efficiency (LE) should be slightly below 100% for the correct estimation of the nucleus size. F: Visitation analysis of simulations considering the influence of photobleaching.

the detection of the transition from the slow nucleation to the fast polymerization regime, the visitation analysis does not need a big difference between nucleation and polymerization rates (Fig. 4.6 A).

Average rates Next, I looked into the information of the time-averaged traces that can be obtained in an experiment when the starting point of the growth process is synchronized. A pronounced nucleation or conversion mechanism is directly visible in the shape of the averaged intensity curve (Fig. 3.6 D). Since the sum follows the same behavior as the average of many traces, this can also be applied to experiments where the single-filament data is not available (Fig. 4.1). However, if single filament data is available, averaging is a useful tool to circumvent the limitations of a low SNR (Fig. 4.7 A, B). When the mean step size of an individual monomer binding event is known, average rates can be estimated by calculating the time until the average trace reaches a level corresponding to a monomer, a dimer and so forth (described in chapter 3). In these average rates, a nucleation process or a single conversion step are well visible also at a low SNR (Fig. 4.4, 4.7).

Similarly to the visitation analysis (Fig. 4.4 A, D), the average rate (Fig. 4.4 B, E) also reveals signatures that can be clearly associated with either a nucleation-elongation (Fig. 4.4 B, 4.7 A) or a conversion mechanism (Fig. 4.4 E, 4.7 B). Nucleation-elongation starts from a low average rate and increases monotonically until it reaches the average elongation rate. The average rate from a conversion mechanism first drops and then increases until it also reaches the average elongation rate. The average rate analysis was able to identify the nucleus size and the conversion size accurately (Fig. 4.4).

The extracted average rates are not influenced by SNR and measurement rates, down to an SNR of 0.1 and a measurement rate of only twice the polymerization rate (Fig. 4.7 A-D). When the labeling efficiency is below or above 100%, a nucleation mechanism or a conversion step is still visible in the average rates, however, the conversion size cannot be estimated (Fig. 4.7 E, F). In the case of photobleaching, the photobleaching rate gets problematic for the calculation of the average rates when the growth is inhibited to an extent that higher average monomer numbers are apparently not reached and the average rates can therefore not be calculated for the formation of these oligomer sizes (Fig. 4.7 G, H).

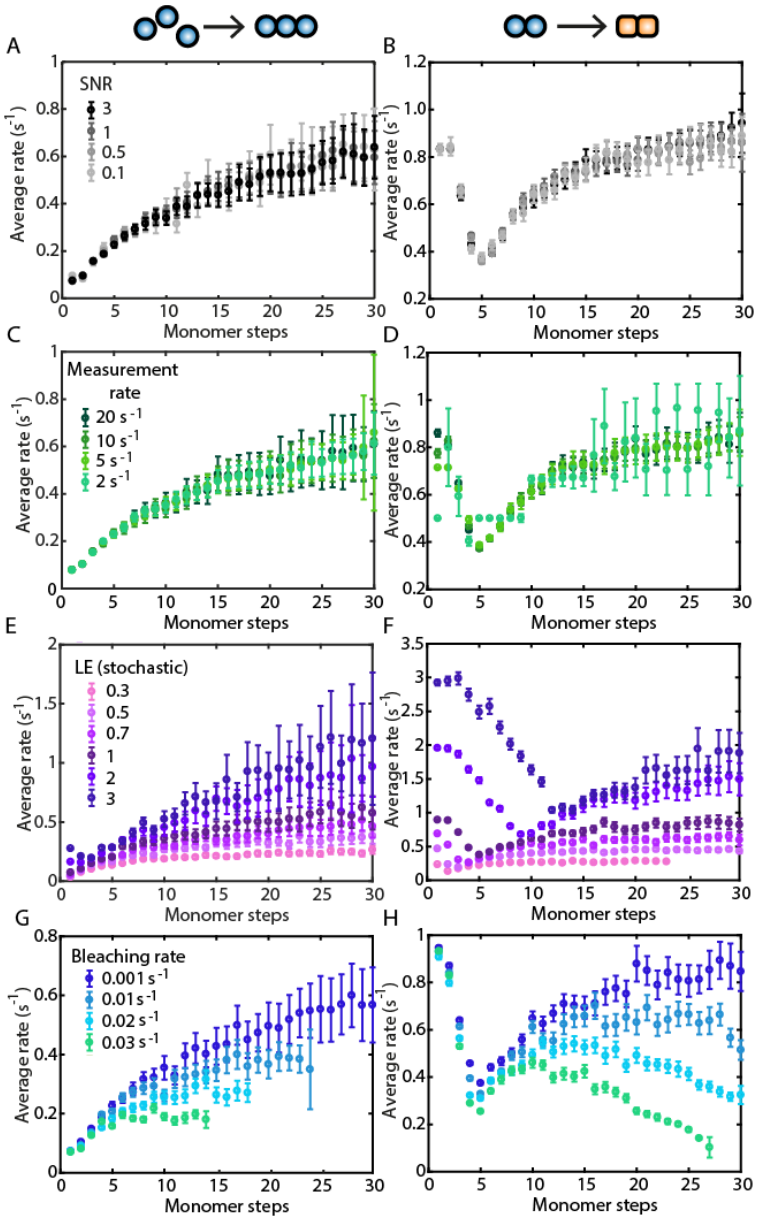

FIGURE 4.7: Robustness of the average rate analysis. A, B: Average rate analysis on simulations applying different SNRs. A nucleation mechanism (A) or a slow conversion step (B) can be detected until a very low SNR. C, D: Average rate analysis on simulations varying the sampling time. To detect a nucleation mechanism or conversion step, the measurement rates should be at least 2x faster than the fastest rate. E, F: Average rates for simulations using monomers with different labeling efficiencies. A nucleation mechanism (E) can be detected at all tested labeling efficiencies. For the correct conversion step (F), the labeling efficiency should be at 100%. G, H: Average rates for simuluations considering the influence of photobleaching. A high photobleaching rate can shorten the average trace or lead to apparently slower kinetics.

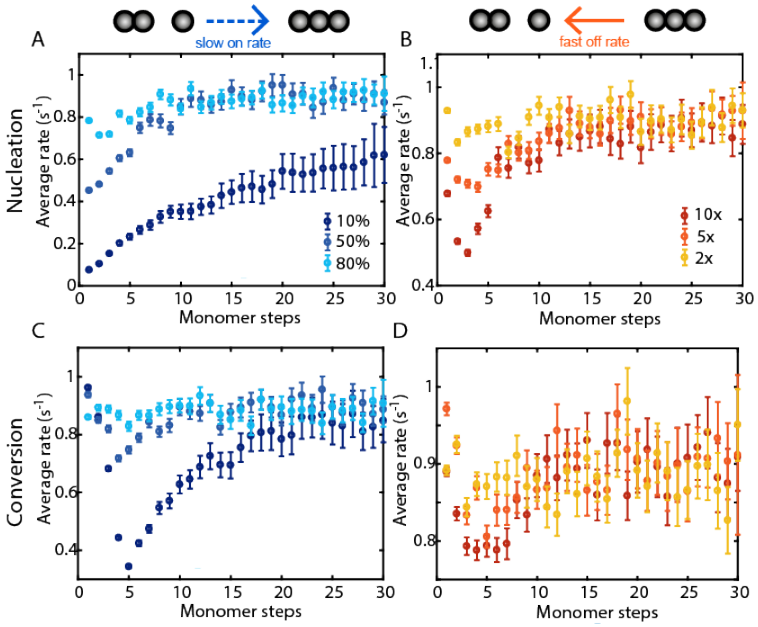

FIGURE 4.8: The influence of a change in the on-rate versus a change in the off-rate in the average rate analysis for a nucleation (A, B) and a conversion mechanism (C, D). A, C: Average rate analysis on simulations varying the association rate during nucleation or conversion. The association rates during nucleation k^{+}_{nuc} were at 10, 50 or 80% of k^{+}_{poly}. B, D: Average rate analysis on simulations varying the dissociation rate during nucleation or conversion. The dissociation rates during nucleation k^{-}_{nuc} were a factor of 10, 5 or 2 of k^{-}_{poly}. For nucleation and conversion, the average rates show a different behavior dependent on whether the association rate or the dissociation rate was changed with respect to the polymerization rates.

A nucleation phase can be determined by a slower on-rate respective to the polymerization kinetics, or by a destabilization effect via high off-rates. These two mechanisms are visible in the average rates (Fig. 4.8). For a nucleation process, a slower on-rate during nucleation results in a steady increase in the average rates with oligomer size (Fig. 4.8 A), whereas for a faster off-rate, the average rates first decrease with oligomer size and then increase again (Fig. 4.8 B). Also for a conversion mechanim, the average rate shows a different behavior for the single step with slower association rate or faster dissociation rate than for the surrounding steps (Fig. 4.8 C, D). Thus, the average rate analysis can be used to determine whether the association or the dissociation kinetics are changed when the nucleus size is reached.

Influence of SNR and data collection rate Every analysis tool tested here has its own requirements in terms of the experimental data and the question that needs to be answered. Is the goal to detect a slower conversion step, to determine the nucleation mechanism or is the aim to correctly determine every microscopic rate for each step? To estimate what SNR and measurement rate are needed to correctly answer these questions, I tested the presented analysis methods for their robustness towards noisy data and slow sampling times. The average rate analysis proved to be the most robust towards low SNRs and slow data collection rates (Fig. 4.7). The dwell-time analysis and the visitation analysis both use single-filament data and a step-finding algorithm, but the visitation analysis was much more robust towards low SNRs and slow measurement times (Fig. 4.3, 4.6). For the dwell-time analysis, the performance could be improved for measurements with a slow data collection rate when a double-step correction was applied (Fig. 4.3 F). The intensity of the individual steps is used to define single, double or triple steps to transform intensity into monomers correctly even when fast single steps cannot be resolved. However, even with the double-step correction, the dwell-time analysis could not identify several individual steps with different rates and remains sensitive towards all tested measurement parameters (Fig. 4.3).

Labeling efficiency Imaging of filament growth in ZMW or TIRFM relies on fluorescent labeling of the monomers. Labeling of the proteins for the nucleation studies brings additional complexities into the analysis. Dependent on whether a stochastic or a specific labeling strategy is used, the fraction of labeled monomers either shows a Poisson distribution of labels where

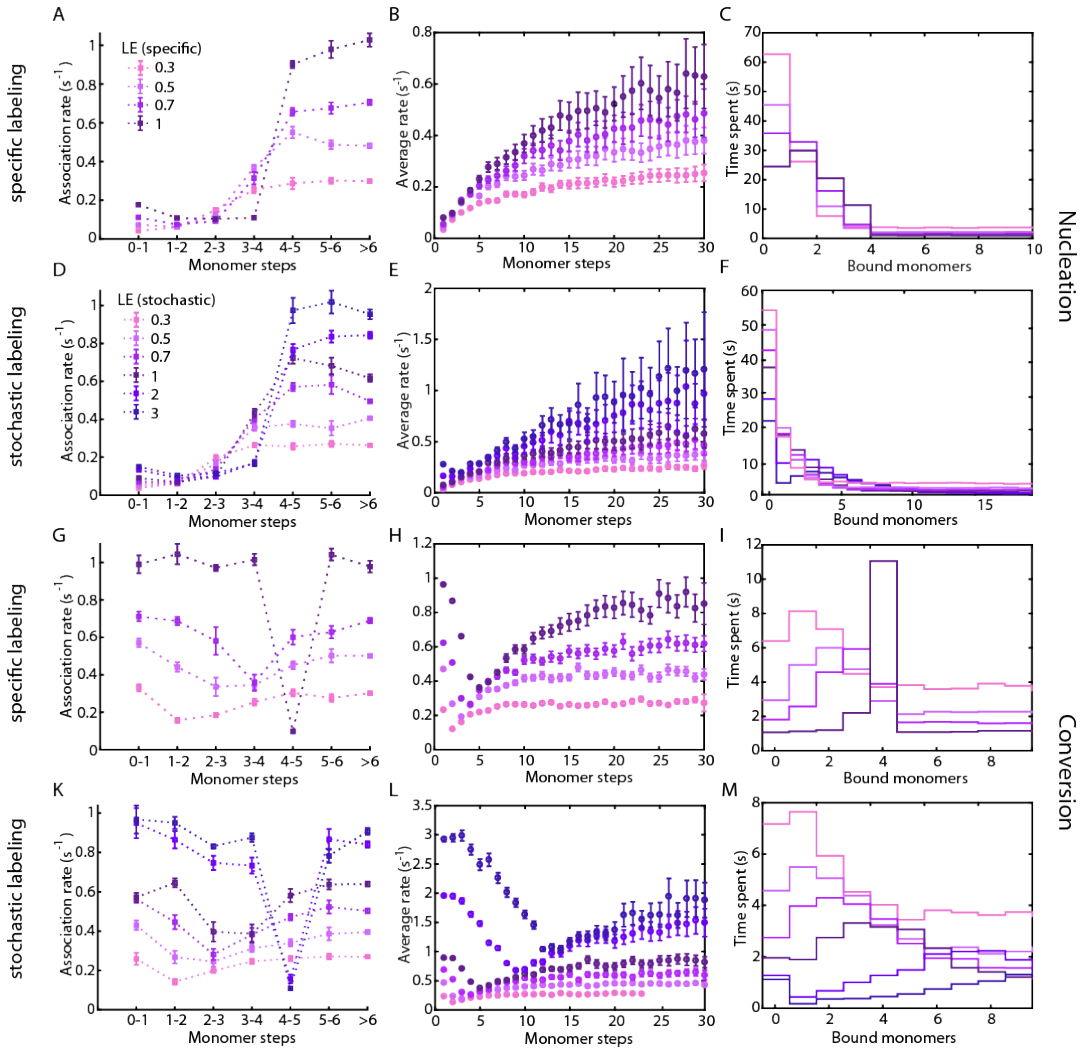

FIGURE 4.9: A comparison of the effect of stochastic and specific labeling efficiencies on the analysis methods. A-F: Analysis methods on simulations assuming a nucleation mechanism, G-M: Analysis methods on simulations assuming a conversion mechanism. First and third row: specific labeling with 1 or 0 labels per monomer, second and fourth row: stochastic labeling where multiple labels per monomer are possible. First column: dwell-time analysis, second column: average rate analysis, third column: visitation analysis. For a nucleation mechanism, a wide range of labeling efficiencies can be tolerated for all analysis methods. However, the dwell-time analysis extracts the correct polymerization rates only for labeling efficiencies of 100% for specific labeling (A) or more than 100% for stochastic labeling (D). For the determination of the correct conversion size, the labeling efficiency should be at 100% for the average rate analysis and the visitation analysis (H, I, L, M). For the dwell-time analysis, labeling efficiencies at or above 100% are needed (G, K).

there may be more than one dye per monomer, or each monomer has either zero or one dye molecule attached as a result of a specific labeling strategy. Though high labeling efficiencies are in some cases possible (e. g. Lavergne et al., 2016), sample preparation can be very time intensive. In addition, it is sometimes necessary to use a mixture of labeled and unlabeled monomers to not influence the assembly process. When the protein labeling is not specific with 100% efficiency, the labeling efficiency needs to be included in the analysis. To test the influence of different labeling strategies and the resulting labeling efficiencies, the monomer number trace was modified with a Poisson distribution of different labeling efficiencies from 0.3 to 3, or with a specific labeling approach with labeling efficiencies from 0.3 to 1.

I investigated the impact of labeling efficiency on the different analysis methods. For a distribution of dye molecules on the assembling monomers, the labeling efficiency should be at least at 30 to 50%, dependent on the analysis method and whether stochastic or specific labeling is used (Fig. 4.9). The visitation analysis allowed for labeling efficiencies down to 30% (Fig. 4.9 C, F). In contrast, the dwell-time analysis reproduced the correct on-rate only with very high labeling efficiencies (Fig. 4.9 first column). For specific labeling, the correct polymerization rate was determined when a labeling efficiency of 100% was simulated (Fig. 4.9 A, G). For stochastic labeling, where also monomers without any label are possible, the labeling efficiency had to be above 100% for the correct estimation of the polymerization rate (Fig. 4.9 D, K). The apparent polymerization on-rates, as extracted from the average traces, depended on the labeling efficiency (LE* k^{+}_{poly}) (Fig. 4.9 second column). For specific labeling of the monomers, a nucleation process could still be identified even at 30% labeling efficiency, whereas a specific conversion step could only be detected at 100% specific labeling (Fig. 4.9).

For the dwell-time analysis and the average rates, the extracted rates for the polymerization regime correspond to k^{+}_{poly} as LE $\cdot$ k^{+}_{poly}. Thus, if the process reaches polymerization kinetics and the labeling efficiency is known, the polymerization rate can be extracted quantitatively.

Effect of Photobleaching Another artifact that impacts the measurements is photobleaching of fluorophores. Although photobleaching can be reduced by the use of oxygen scavenging systems (see chapter 2), it will always affect the intensity signal dependent on the photobleaching rate. In intensity traces,

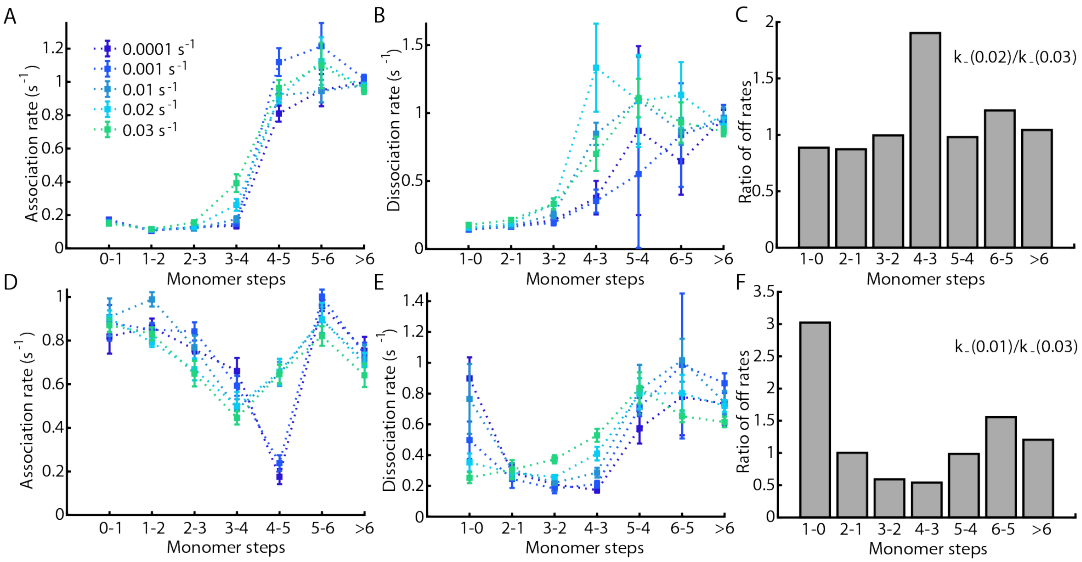

FIGURE 4.10: Using photobleaching as a tool to estimate the nucleation or conversion step. Dwell-time analysis on a simulation assuming a nucleation mechanism (A-C) or a conversion mechanism (D-F) with k^{+}_{nuc} = 0.1 k^{+}_{poly} and no change in the off-rates. Photobleaching with different photobleaching rates has been applied to the simulations. A, B: The extracted association rates visualize the nucleation or conversion step at 4 monomers. B, E: The extracted dissociation rates for the same simulated processes as in (A) and (D). The apparent dissociation rates at the nucleus or conversion size are affected most by different photobleaching rates. C, F: The ratio between the apparent dissociation rates for the same simulation under the influence of different photobleaching rates are plotted for each step. The difference between the apparent dissociation rates is the highest at the nucleation or conversion size.

a photobleaching step is indistinguishable from a dissociation step. This hinders not only the direct measurement of the dissociation rate in single-filament traces, but also leads to a mismatch between the intensity level and the monomer number, which has an effect on the extracted on-rates as well.

To test for the influence of photobleaching, I introduced down steps in the simulations based on different photobleaching rates. These rates are in the regime of the experimentally determined values (chapter 3). If a monomer dissociates after photobleaching, no down step is introduced. If not indicated otherwise, photobleaching was applied to 100% specifically labeled monomers.

The presented analysis methods are all affected by photobleaching, although some still allowed the identification of the underlying assembly mechanism (table 4.1). For all analysis methods, photobleaching should not exceed 3% of the on rate during polymerization or 30% of the off-rate (Fig. 4.3, 4.5, 4.7). However, even with photobleaching, it was even possible to distinguish between a nucleation mechanism that affects the on-rate or the off-rate when looking at the effect of different photobleaching rates on the results, since a high off-rate leads to the exchange of photobleached monomers with unbleached monomers. By comparing the apparent off-rates from measurements with different photobleaching rates as determined by the dwell-time analysis, the nucleus size or a conversion step could be estimated even at higher photobleaching rates (Fig. 4.10). Thus, photobleaching can be used to identify steps with high monomer fluctuation, i.e. an oligomer with a higher off-rate.

Effect of labeling efficiency and photobleaching To visualize the impact of labeling efficiency and photobleaching, I simulated unhindered filament growth without nucleation or conversion and a restricted filament growth that stops at four assembled monomers (Fig. 4.11). A photobleaching rate at 10% of the polymerization kinetics still allows for a correct kinetic analysis via the visitation analysis, dwell times and average rates (Fig. 4.11 red curves). In combination with a stochastic labeling efficiency of 30%, the visitation analysis shows a distribution shifted towards smaller oligomer sizes (Fig. 4.11 A, E). The dwell-time analysis resulted in reduced rates ((Fig. 4.11 B, F). For unhindered growth, the resulting rate depended directly on the labeling efficiency as $LE \cdot k^{+}_{poly}$. The same is true for the average rate analysis of a nucleation or conversion process (Fig. 4.7), thus, if the process reaches

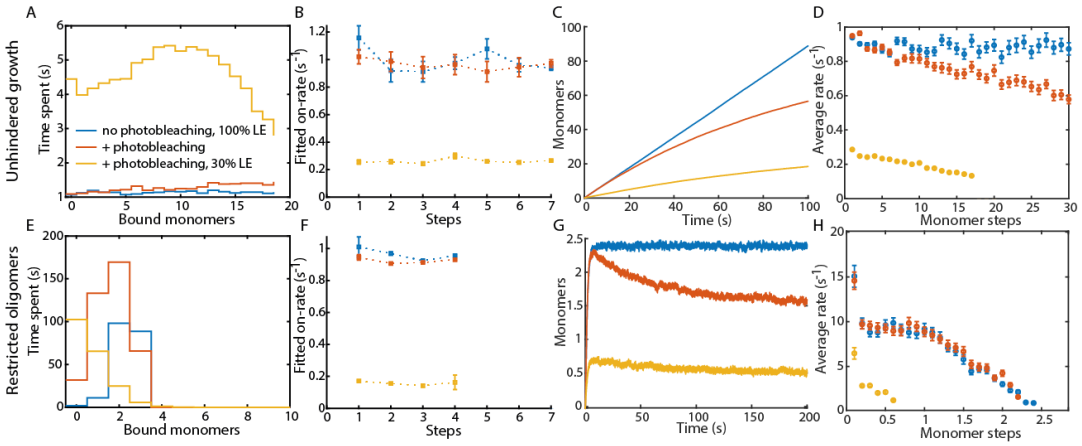

FIGURE 4.11: Effect of photobleaching and labeling efficiency on unhindered growth (A-D) and restricted growth that stops after the assembly of four monomers (E-H). Both unhindered and restricted growth had $k^{+}_{poly} = 1s^{-1}$ and $k^{-}_{poly} = 0.1s^{-1}$. Visitation analysis (A, E), dwell-time analysis (B, F) and average rates (D, H) extracted from the average traces (C, G) were applied to data with 100% labeling efficiency and no photobleaching (blue data). The average trace of restricted growth reaches only 2.5 monomers, despite possible growth until 4 monomers, because of the equilibrium between the on- and the off-rate. The effect of a photobleaching rate of 0.01 s^{-1} does not significantly influence the extracted rates and the visitation analysis (red data). The combination of stochastic labeling of 30% and photobleaching with a rate of 0.01 s^{-1} affects all analysis methods (yellow). Errorbars for the dwell-time analysis represent 95% confidence intervals of the exponential fit.

TABLE 4.1: Robustness of the analysis methods

	Dwell-time analysis		Visitation analysis		Average rates	
	Mecha-nism	Single steps	Mecha-nism	Single steps	Mecha-nism	Single steps
SNR	>1	>1	>0.1	>1	>0.1	>0.1
Sampling rate	>10x*	>20x	>1x	>2x	>1x	>5x
LE_{stoch}	>1	>2	<1	1	>0.3 (1**)	>0.7
LE_{spec}	1	>0.3	1	>0.3	1	>0.3
Photobleaching	<3%*	<0.1%	3%	<2%	<3%	<2%

* compared to the fastest rate
** for correct determination of the conversion step

polymerization kinetics and the stochastic labeling efficiency is known, the polymerization rate can be extracted quantitatively.

For a restricted growth mechanism where the growth stops after a certain oligomer size is reached (exemplified for four monomers in Fig. 4.11 E-H), the average rates can only be extracted for the very first monomers, because the average filament size does not reach beyond 0.5 monomers due to the equilibrium between the on- and the off-rate (Fig. 4.11 G). For that reason, fractional average rates in 0.1 monomer steps have been extracted using the time until the average trace reached the monomer level of 0.1, 0.2,... monomers (Fig. 4.11 H).

4.4 Discussion

Single filament data as well as synchronized ensemble data contain a wealth of information that is not immediately visible from looking at the recorded time traces. The most common approach for dealing with this type of data is probably the kinetic analysis of the dwell times. The obtained microscopic rates should directly reflect the underlying self-assembly mechanism. However, a correct interpretation of the dwell-time distributions depends, to a high extend, on the quality of the data, such as the signal to noise ratio, but also on the measurement rate or the influence of dye photobleaching in fluorescence microscopy measurements (Fig. 4.3, table 4.1). Therefore, I developed other analysis methods for single filament data and synchronized ensemble data that give insight into the microscopic mechanism of the self-assembly process

that are less prone to misinterpretation. An overview about the minimal requirements for each of the tested analysis methods in terms of measurement rate, SNR, labeling efficiency and photobleaching is given in table 4.1.

The visitation analysis is able to detect a slow nucleation phase despite non-ideal measurement conditions like low SNR (Fig. 4.6). Moreover, it is sensitive enough to detect multiple events with slower or faster kinetics during an assembly process (Fig. 4.5). Thereby, the sampling rate needs to be about a factor of 2 higher than the expected kinetics, which is an order of magnitude slower than the required speed for the dwell-time analysis (table 4.1). The visitation analysis on single-filament data is, therefore, a suitable method to detect nucleation or individual conversion steps (table 4.1).

When the quality of single-filament data is not sufficient for the use of a step-finding algorithm to extract the individual monomer binding and dissociation events, an average trace can be obtained from the growth information of multiple filaments. If the number of filaments and the intensity information of a single monomer binding event is known, average rates can be used to visualize and detect a slow nucleation phase or a pronounced slow individual step. The average rate analysis can deal with a sampling time in the same range as the expected kinetics and an SNR as low as 0.1 (Fig. 4.7, table 4.1) and is therefore the most robust analysis method presented here.

For the simulations of a nucleation or conversion process, changes in the dissociation and the association rates have been separated to study the effects independently. In a real self-assembly process, the transition from nucleation to polymerization could affect both rates, enhancing the binding rate and stabilizing the formed oligomers at the same time. If, however, only one rate is affected during the growth process, the average rates can be used to determine whether the association or the dissociation kinetics are changed when the nucleus size is reached (Fig. 4.8).

The dwell-time analysis provides the microscopic rates for each monomer addition and should reveal the underlying assembly mechanism. However, it is very sensitive to the SNR and acquisition speed, which should be more than an order or magnitude faster than the expected kinetics (table 4.1). However, an advantage of the dwell-time analysis is that photobleaching can be used as a tool when the same measurement is repeated with different photobleaching rates. This can be accomplished by using different laser powers for the same

measurement. A comparison of the extracted rates can help identifying the nucleus size or conversion step (Fig. 4.10).

Photobleaching, in general, affects all analysis methods (table 4.1). The dwell-time analysis is most affected when the kinetics of single steps are to be determined (Fig. 4.3, table 4.1). Photobleaching affects the conversion from intensity to monomer number. As a result, the dwell-time histogram contains dwell times from different oligomer sizes, which leads to an averaging effect of the rates of the different oligomer sizes. For the visitation analysis and the average rates, the photobleaching rate should not exceed 2 to 3% of the association rate (table 4.1).

Concerning the labeling of the monomers, the labeling efficiency should be at least at 30 to 50%, dependent on the analysis method and whether stochastic or specific labeling is used (Fig. 4.9). The visitation analysis can tolerate labeling efficiencies down to 30% (Fig. 4.6, 4.9). In contrast, the dwell-time analysis reproduced the correct on-rate only with very high labeling efficiencies (Fig. 4.3, 4.9). For specific labeling, the on-rate during polymerization can be corrected for as $LE \cdot k^{+}_{poly}$ when the labeling efficiency is known. Using the dwell-time analysis, a nucleation process could still be identified even at 30% specific labeling efficiency, whereas a specific conversion step could only be detected at 100% specific labeling (Fig. 4.9).

To summarize, I developed new analysis methods for single and averaged filament data that can be obtained by fluorescence microscopy or iScat. These analysis methods are highly robust towards low SNR and slow measurement rates, in contrast to the widely used dwell-time analysis.

Chapter 5

Experimental Studies on Actin Nucleation

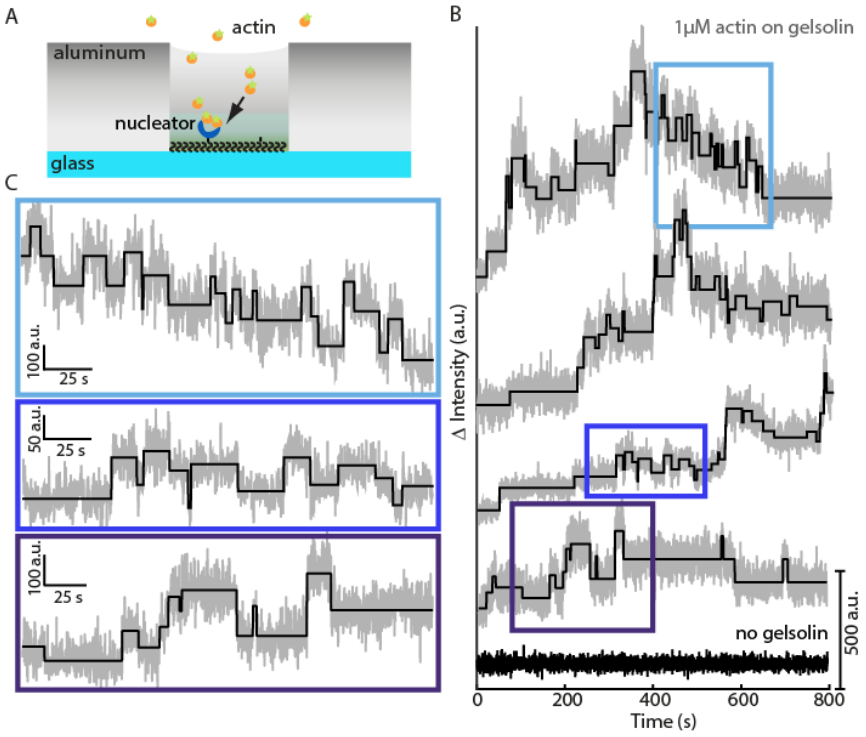

FIGURE 5.1: Observation of gelsolin-mediated actin filament nucleation and elongation within ZMW. A: Schematic of a ZMW with gelsolin attached to the coverslip (not to scale). B: Experimental data. 1 μM of atto-488 labeled actin was added to the ZMW and the fluorescence was monitored over 800 seconds. Grey: measured intensity trace, Black: underlying trace as determined by a step-finding algorithm. The bottom trace was taken from an experiment where gelsolin was not present. C: Zoom-ins of the corresponding highlighted regions in panel B.

Actin polymerization has been studied thoroughly (see chapter 2), however, the early steps in actin assembly before and around the formation of the nucleus have never been observed in detail. Therefore, I used ZMW to directly

visualize the early steps in actin nucleation (Fig. 5.1). These data provide information on the growth process on a single filament level, as the individual association steps are directly visible. The developed analysis methods described in chapter 3 were applied to these data with the goal of elucidating the hidden information inside the single filament traces.

First, I studied pointed-end actin nucleation on the weak nucleator gelsolin (see chapter 2). The biotinylated gelsolin molecules were attached to the bottom of the functionalized ZMW via a streptavidin-biotin linker (Fig. 5.1 A). Upon addition of actin-atto488 or actin-Cy5 under polymerizing conditions, the intensity signal started to increase and single filament traces could be extracted as described in chapter 3.

Gelsolin forms the GA_2 complex with two actin monomers, which acts as a weak nucleator as its presence in bulk actin polymerization assays does not abolish the lag phase (Coué and Korn, 1985). In order to compare those results with a known strong nucleator, I also carried out experiments with the formin-homology domain 2 (FH2) of the formin cappuccino (see chapter 2). Furthermore, ZMW experiments were carried out with yet another class of actin nucleators, the ABCD domain of spire. These experiments were performed in collaboration with Radoslav Kitel, PhD of the group of Tad Holak, University of Krakow, Poland.

During polymerization, the actin monomers ungergo a conformational change, the flattening of the actin monomer inside the filament structure (see chapter 2). Latrunculin A inhibits this conformational change and is known to disrupt the filament structure in cells (see chapter 2). To elucidate the timepoint and effect of the flattening on actin nucleation, I repeated the experiments using gelsolin as a nucleator protein with an excess concentration of LatA. Furthermore, I looked into the effect of Miuraenamide A, which also binds monomeric actin specifically, to add to the emerging knowledge of the applicability and function of actin targeting drugs using FCS on a confocal microscope set-up.

5.1 Proof of Principle

In order to test the applicability of ZMW for the intensity measurement of individual dyes in a step-wise manner, DNA double strands labeled with 4, 6 or 8 atto488-dyes were attached to the bottom of the ZMW. ZMW arrays were measured on a fluorescence microscope where hundreds of individual

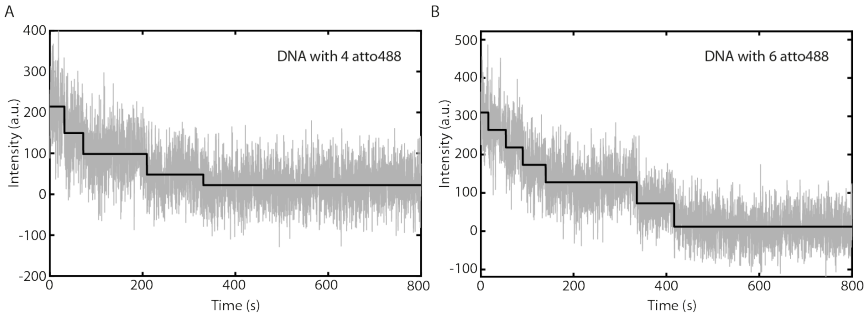

FIGURE 5.2: Test of the step-finding algorithm on DNAs with a different number of labels. Example photobleaching traces of double strand DNA labeled with (A) 4 atto488-dyes and (B) 6 atto488-dyes are plotted. Grey: measured fluorescence signal, black: result of the step-finding algorithm.

TABLE 5.1: Photobleaching steps of DNA labeled with 4, 6 or 8 atto488 dyes

4 dyes	6 dyes	8 dyes
5.5 ± 1.3	6.7±1.3	7.3±1.4

apertures in real time could be observed. The labeled DNA strands were photobleached, which resulted in intensity traces with a step-wise decrease in intensity (Fig. 5.2). As the step-finding algorithm does not distinguish between up and down steps, the photobleaching traces could be treated in the same manner as the traces of actin assembly. The number of down steps reflected the number of dyes on the DNA strands with an error of about one dye (Fig. 5.2, table 5.1). Thus, the method is sensitive for the intensity measurement of up to around six to eight dye molecules.

The addition of 1 μM actin monomers labeled with atto488 onto an attached tethering protein at the bottom of the ZMW resulted in an increase in the intensity per individual well over time under polymerizing buffer conditions (in the presence of KCl and Ca^{2+}) (Fig. 5.3 C). Under non-polymerizing conditions as well as without tethering protein, no increase in the intensity was observed (Fig. 5.3). The intensity fluctuates a bit more when the tethering protein is present compared to without the tethering protein (Fig. 5.3 A, B). This could be due to some transient attachment of actin in G-buffer to the here used tethering protein, gelsolin. The fact that the intensity only increases under polymerizing conditions and in the presence of a tethering protein indicates that filaments grow specifically attached to the tethering protein in the ZMWs. I used actin molecules covalently labeled with 90% labeling efficiency with atto488 or with 30% labeling efficiency with Cy5 on random surface lysines, which was shown not to impair filament nucleation and elongation

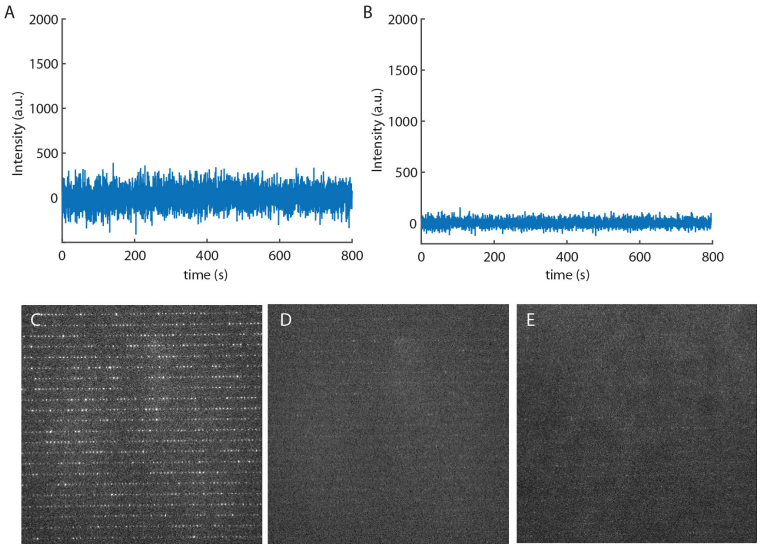

FIGURE 5.3: Intensity changes signifying nucleation were not observed in G-Buffer or without gelsolin. (A) An example trace from a ZMW for a measurement in G-buffer. (B) An example trace from a ZMW in F-buffer for a measurement without gelsolin as a tethering protein. (C) An image of a waveguide array with 200 nM gelsolin and 1 μM actin in polymerizing conditions after 800 seconds. (D) An image of a waveguide array with 200 nM gelsolin and 1 μM actin in G-buffer after 800 seconds. (E) An image of a waveguide array with 1 μM actin without gelsolin under polymerizing conditions after 800 seconds.

(Crevenna et al., 2013). The high degree of labeling does not impair long filament formation for atto488 (Fig. 5.4 A), however, for Cy5 the high degree of labeling reduces the probability of seeing long filaments in TIRFM (Fig. 5.4 B). Therefore, for measurements with Cy5, only 30% labeling efficiency was used.

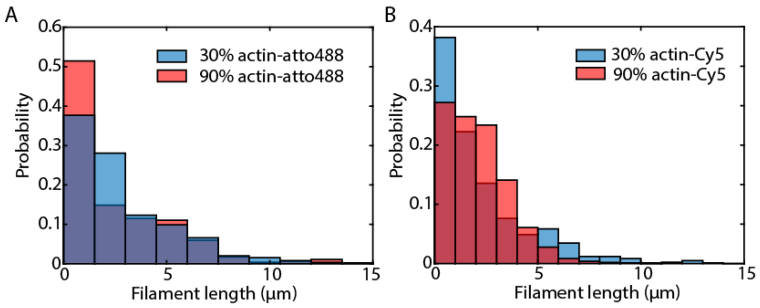

FIGURE 5.4: The filament length distributions for 30% and 90% labeled actin after 250 s after inducing polymerization for (A) atto-488 labeled actin and (B) Cy5-labeled actin.

To show that indeed long filaments can form inside ZMW, a photobleaching experiment was done after one hour incubation in ZMW. Before photobleaching, the filaments were stabilized with phalloidin, so that down steps could be

fully attributed to photobleaching and not to disassembly. The distribution of down steps showed that long filaments can assemble inside ZMW (Fig. 5.5).

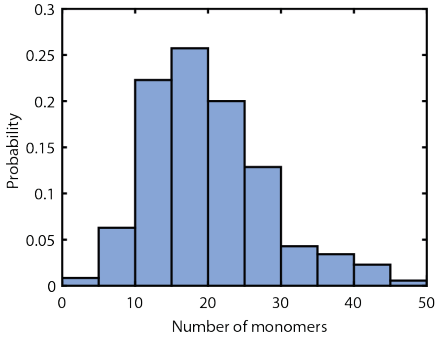

FIGURE 5.5: Number of monomers as determined from photobleaching steps after one hour incubation time in the waveguides under growing conditions. The filaments were stabilized using phalloidin.

To minimize the possibility that two or more molecules were present in a single aperture, a low concentration of tethering protein was used when preparing the waveguides. The fraction of apertures monitored where signal was detected was never more than 30%, which corresponds to around 600 wells, to keep the probability of double occupancy within the apertures low. The occupancy of the apertures by biotinylated gelsolin molecules is given by Poissonian statistics of the form $P(k) = e^{-\lambda}(\lambda^k/k!)$, where λ is the mean occupancy and k is the number of molecules in the aperture. At the used concentrations of tethering protein, between 600 to 700 apertures showed a signal out of 3000 apertures, i.e. there is an average occupancy, λ, of 0.22 ± 0.02. The probability that two or more molecules were present ($k \geq 2$) in a single aperture is then 0.020 ± 0.003. Of the traces that showed a signal, only 10% to 12% would originate from apertures with multi-molecule occupancy. Due to this low probability, no further correction for multiple occupancy was applied in the analysis.

Functionality tests of the biotinylated tethering proteins (gelsolin, cappuccino and spire-ABCD) showed that the capping function of gelsolin and the nucleating function of cappuccino were not impaired by the attachment of biotin (Fig. 5.6, 5.7). Actin filaments showed the same length distribution with spire as with biotinylated spire (Fig. 5.8). The capping and severing behavior of biotinylated gelsolin was compared to the unbiotinylated form in a TIRFM assay using actin-atto488 (Fig. 5.6). The average filament length was reduced to the same average length by both gelsolin forms via the severing activity of gelsolin. Actin binding to biotinylated gelsolin was confirmed by a TIRFM

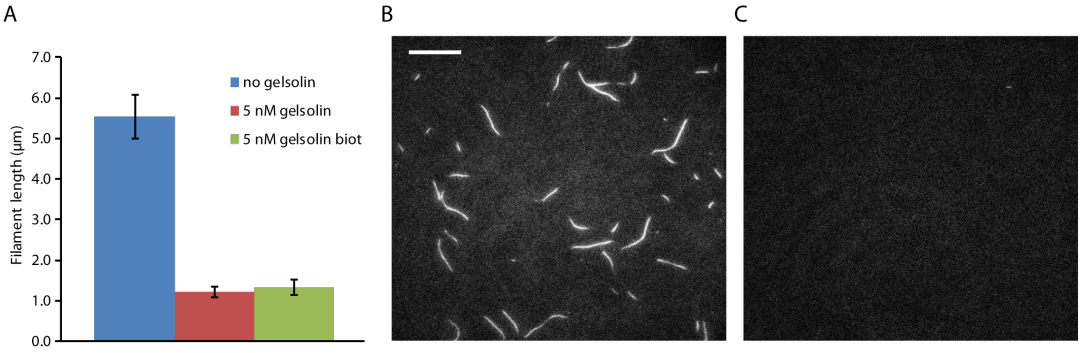

FIGURE 5.6: Biotinylation and surface immobilization of gelsolin does not impair function. The efficiency of biotin labeling was 80%. A: The average actin filament length measured using TIRF microscopy after 5 minutes growth of 1 μM actin (N = 29) and 5 nM gelsolin (N = 61) or 5 nM biotinylated gelsolin (N = 69). B, C: TIRFM images of filament growth on the surface in the presence (B) or absence (C) of biotinylated gelsolin. Scale bar is 10 μm.

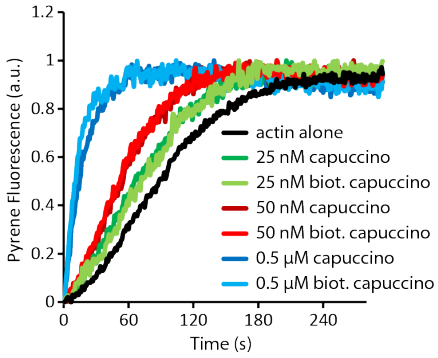

FIGURE 5.7: Biotinylated cappuccino and actin-cy5 are functional as monitored by a pyrene assay. The nucleation rate of actin alone (black) is enhanced by cappuccino (dark green, red and blue) and biotinylated cappuccino (light green, red and blue) in a concentration-dependent manner.

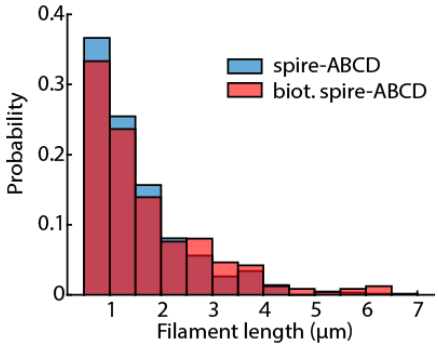

FIGURE 5.8: Biotinylated spire-ABCD shows the same behavior as unlabeled spire-ABCD. The filament length distributions after 850 s are plotted from a TIRFM assay for unlabeled spire-ABCD (blue) and biotinylated spire-ABCD (red).

assay without biotinylated gelsolin, where no filaments could be observed close to the cover slide (Fig. 5.6 C). The nucleating function of biotinylated cappuccino was confirmed using a pyrene assay, which was done by Radoslav Kitel, PhD, in Warsow, Poland. Biotinylated cappuccino and the nonlabeled form show the same nucleating activity on actin-cy5 (Fig. 5.7).

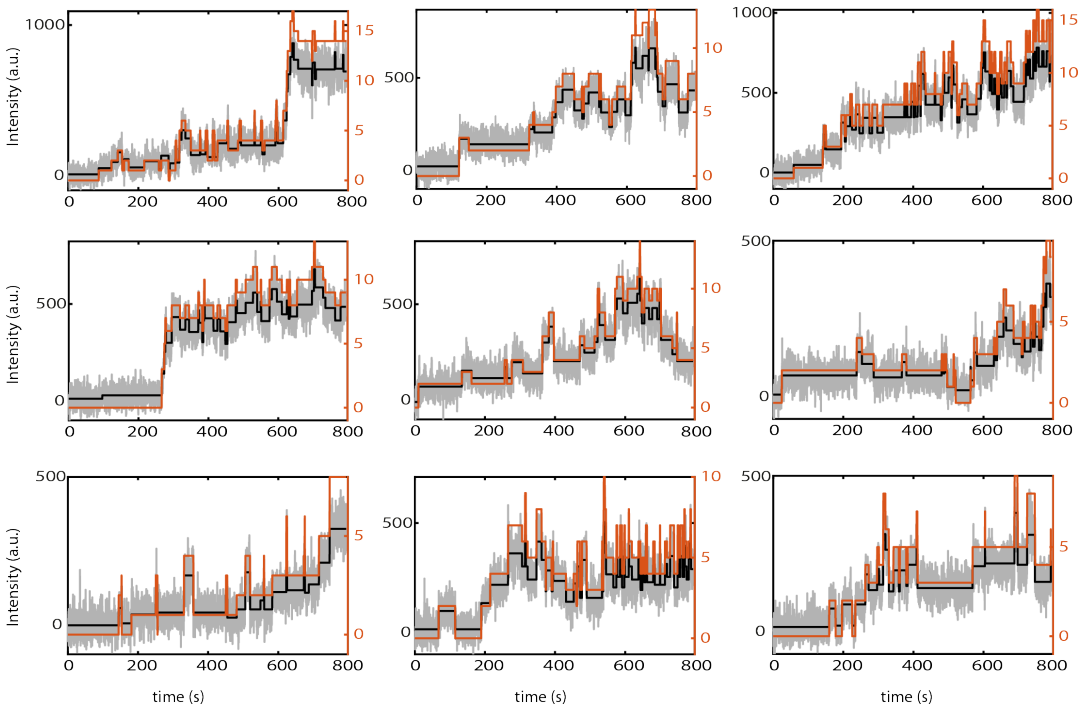

FIGURE 5.9: Measurements of gelsolin-initiated actin oligomerization. A few characteristic traces of actin nucleation on gelsolin are shown for 1 μM actin. Grey: fluorescence intensity, black: result of the step-finding algorithm, orange: conversion to monomer number, using the step-size information and double-step correction.

The addition of actin-atto488 to the ZMW containing tethered gelsolin resulted in a dynamic step-wise increase in the intensity per individual well under polymerizing buffer conditions (Fig. 5.9). The step-finding algorithm (chapter 2) finds the most probable step trace without accounting for the step size. The intensity to monomer conversion (orange traces in Fig. 5.9) takes into account the individual step size with regard to the step size distribution and converts the results of the step-finding algorithm into a monomer trace (chapter 2). The good overlay between the signal, the result of the step-finding algorithm and the monomer trace both on average (chapter 2) and for the single filaments show that the intensity to monomer conversion is working well.

5.2 Material and Methods

5.2.1 Proteins and DNA

Atto488-labeled actin (rabbit, skeletal muscle) and biotinylated gelsolin were purchased from Hypermol (Bielefeld, Germany). Labeled DNA double strands were obtained from IBA (Göttingen, Germany). DNA molecules were labeled with 4, 6, or 8 atto488 dyes and attached to a biotin-linker.

Cappuccino and Spire Expression and Purification Cappuccino and spire ABCD preparation was done by Radoslav Kitel, PhD working in the group of Tad Holak, PhD in the University of Krakow, Poland. Constructs encoding GST-pABCD1 and GST-CapuFH2 were transformed in E. coli BL21-CodonPlus-RIL competent cells and cultured in LB medium with ampicillin (100 μg/ml) and chloramphenicol (34 μg/ml) at 37°C. Protein expression was induced with 0.5 mM isopropyl-β-D-thiogalactopyranoside (IPTG) when an OD600 of 0.6 - 0.8 was reached. Proteins were expressed for 16-20 h at 16°C. Cells were harvested by centrifugation (30 min, 2000 rpm, 4°C) and bacterial pellets were frozen at -20°C.

Subsequently, pellets were handled on ice using ice-cold buffers. Pellets were thawed on ice and resuspended in ca. 50 mL of lysis buffer A (1xPBS, pH 7.4, 1 mM EDTA, 1 mM DTT, 0.5 mM PMSF) in the case of GST-pABCD or lysis buffer B (50 mM Tris-HCl pH 7.0, 150 mM NaCl, 0.2% Triton-X100, 1 mM DTT, 1 mM PMSF and 1 μg/mL DNAseI) in the case of GST-CapuFH2. After cell disruption using ultrasonification, the whole extract was cleared by centrifugation (30 min, 15000 rpm, 4°C). The soluble fraction containing recombinant proteins was then loaded onto a GSTPrep FF 16/10 column (GE Healthcare) connected to an ÄKTA FPLC System (GE Healthcare). After removal of bacterial host proteins, the column was washed with 10 cv of PBS and then equilibrated with PreScission Protease buffer (50 mM Tris-HCl, pH 7.0, 150 mM NaCl, 1 mM EDTA, 1 mM DTT). Next, a solution of PreScission Protease (4 mg/ml) was loaded onto the column and incubated overnight at 4°C. Subsequently, cleaved proteins were eluted from the column with PreScission Protease Buffer. The GST tag that remains on the column and PreScission Protease were removed by washing the column with regeneration buffer (50 mM Tris-HCl pH 8.0, 150 mM NaCl, 10 mM GSH). Fractions containing spire-ABCD or CapuFH2 were concentrated and subsequently purified by

a gel filtration method on S75 Superdex columns (spire-ABCD) equilibrated with storage buffer (50 mM Tris-HCl, pH 8.0, 300 mM NaCl, 1 mM DTT) or on S200 Superdex columns (CapuFH2) equilibrated with storage buffer.

Spire and Cappuccino biotinylation via Sortase A-mediated ligation Spire-ABCD and CapuFH2 constructs were labeled at their N-termini using Sortase A-mediated ligation (SML). In a typical reaction, CapuFH2 (45 μM) or spire-ABCD (50 μM) were mixed with an excess of desthiobiotin-peptide (300 μM) bearing a sequence recognised by Sortase A (desthiobiotin-GCGLPETGG, Smart Bioscience) and Sortase A (2 μM, Eurx). The reaction mixture was supplemented with 10 mM $CaCl_2$ and incubated for 6 or 24 h at 4°C. The progress of the reaction was monitored with immunoblotting using HRP-conjugated streptavidin (Biolegend). After completion, DB-CapuFH2 was purified on a Superdex 200 Increase 10/300 column (GE Healthcare). The ABCD construct was purified on a Superdex S75 column. The degree of desthiobiotinylation was calculated to be 53% and 60% for CapuFH2 and spire-ABCD, respectively as judged by the HABA assay (ThermoScientific).

5.2.2 ZMW fabrication and functionalization

For the experiments using gelsolin as tethering protein, ZMWs were purchased from Pacific Biosciences (Pacific Biosciences, Menlo Park, CA). For experiments with cappuccino and spire, ZMWs were fabricated by Kherim Willems at the imec Leuven, Belgium and functionalized at the LMU Munich by myself.

ZMWs were fabricated on glass coverslips (22mmx22mm, type #1, Menzel Glazer) by means of physical vapor deposition, e-beam lithography and low-pressure dry etching. Details are described below.

Substrate cleaning Any particles and organic contamination were first removed from the glass surface by submersing the coverslips in Standard-Clean 1 (SC-1) solution, i.e. stock solutions of H_2O:NH_4OH(27%):H_2O_2(30%) mixed in a ratio of 5:1:1 (MicroChemicals, Ulm, Germany) at 75°C for 15 min, followed by a thorough rinsing in high purity water (HPW) and a brief dip (<5 s) in buffered oxide etch 7:1 (MicroChemicals, Ulm, Germany), again rinsed in HPW and dried under a N_2 stream.

Metal deposition Next, each coverslip was subjected to a brief O_2-plasma to activate the surface, followed immediately by physical vapor deposition (Argon sputtering, Pfeiffer Spider 630, Pfeiffer, Germany) of a 80 nm-thick aluminum layer and a 10 nm-tick titanium nitride (TiN) layer. The metals were deposited at 2.5 nm/s.

E-beam lithography Immediately after metalization, a layer of the positive tone electron-beam resist MET-2D/XP52711 (Rohm& Haas, Hoek,The Netherlands) was spin-coated on top of each sample for 1 min at 800 rpm to a final thickness of around 100 nm, followed by a 3 minute soft-bake at 120°C on a hotplate. Next, the ZMWs (150x150 arrays of 140 nm diameter apertures, 1.5 μm pitch) were written in the resist layer with e-beam lithography (Leica VectorBeam 6, Raith, The Netherlands) under ultra-high vacuum (50 keV beam, 5 nm grid and a 65 uC/cm^2 dose). After pattern writing, the samples were baked at 105°C on a hotplate for 15 minutes upon exposure to the atmosphere. The patterned resist areas were then removed by submerging the samples for 1 min in the basic developer solution OPD262 (Fujifilm, Sint-Niklaas, Belgium) followed by a rinse in HPW and drying under N_2. The existence of the ZMW pattern was verified by dark-field microscopy.

Aluminum dry etch The resist pattern was then transferred into the underlying Al/TiN layers by a 45 s inductively coupled plasma reactive ion etch (ICP-RIE) with an Oxford Plasmalab 100 (Ofxord Instruments, Bristol, UK). The chlorine-based gas chemistry ($SiCl_4$/He at 15/60 sccm, 4 mTorr chamber pressure and 50°C chuck temperature) and power densities (ICP at 50 W and RF at 100W) were optimized to yield a good trade-off between etch slope (80-90°), etch rate (3 nm/s) and resist selectivity (>2). To prevent corrosion after exposure to the atmosphere, all $AlCl_3$ residues were removed by submerging each sample (within 5 min) in an post-etch residue remover bath (EKC265, DuPont, Mechelen, Belgium) at 65°C for 5 minutes, followed by rinsing in iso-propylalcohol (IPA), HPW and finally drying under a N_2 stream. Any resist traces were then removed by treating the samples for 10 minutes with an O_2 plasma (100 W, 255 mTorr chamber pressure) in a home-built barrel asher SiO_2/TiN dry etch. To increase the amount of collected fluorescence signal and thereby improve the signal-to-noise ratio of the fluorescence signal inside the ZMWs, the SiO_2 underneath the apertures was recessed for 5-10 nm, resulting in etched ZMWs. To this end, we used the same ICP-RIE tool, etching

for 20 s (0.5nm/s SiO_2 etch rate, > 2 nm/s TiN etch rate) using a fluorine-based gas chemistry (CF_4/O_2/He at 10/40/50 sccm, 12 mTorr chamber pressure and 20°C chuck temperature). Any post-etch polymer residues were finally removed by treating the samples for 10 minutes with an O_2 plasma (100 W, 255 mTorr chamber pressure).

Aluminum wet etch The bulk of the aluminum on the samples was subsequently removed using standard UV contact lithography and wet etching, leaving only 4 squares of 1.5 mm x 1.5 mm with the ZMW arrays at their centers. Briefly, a layer of the positive tone UV resist IX845 (JSR Micro, Haasrode, Belgium) was spin-coated for 30 s at 4000 rpm to a thickness of 1.2 μm, followed by a 1 min soft-bake at 120°C on a hotplate. The unwanted aluminum areas were then exposed to UV light using a MA6 mask aligner (SUSS MicroTec, Garching, Germany) followed by removal of the exposed resist and the underlying Al layer by submersion in the basic developer OPD5262 (Fujifilm, Sint-Niklaas, Belgium) for 3 minutes. After rinsing in HPW and drying under a N_2 stream, the resist protecting the ZMW arrays was removed by submersion in an acetone bath for 15 minutes, followed by a rinse in isopropyl alcohol and drying under a N_2 stream. As before, any residual organic traces were removed by means of a 10 minute O_2-plasma treatment.

Functionalization and passivation of the aluminum ZMWs were passivated using 0.2% polyvinylphosphonic acid (Polysciences, USA) (10 min, 90°C) followed by incubation in 3-[Methoxy(polyethyleneoxy)propyl]trimethoxysilane (6-9 PE-units, abcr, Karlsruhe, Germany) and PEG-biotin-silane (Nanocs Inc, New York, USA) in toluene (4 h, 55°C).

5.2.3 Experiments

ZMW measurements ZMWs were incubated with 0.15 mg/ml streptavidin and 5 mg/ml BSA in PBS for 5 min. After washing with PBS, 200 nM freshly diluted biotinylated gelsolin, 30 nM of cappuccino or 50 nM of spire-ABCD was incubated for 5 min, followed by 5 min incubation with 1 mg/ml BSA and 5 mg/ml biotinylated BSA. 1 μM actin-atto488 or 800 nM actin-Cy5 in G-buffer was incubated in magnesium exchange buffer for 5 minutes on ice (50 μM $MgCl_2$, 0.2 mM EGTA). When Latrunculin A (LatA) was used, it was added at 10x the actin concentration after 4 minutes and incubated for 1 minute. Actin polymerization was induced by adding 1/10 volume of a 10x

concentrated polymerization buffer (50 mM KCl, 2 mM $MgCl_2$, 0.2 mM $CaCl_2$, 0.2 mM ATP, pH 7.0).

The final buffer contained a PCA/PCD oxygen scavenging system with 250 nM protocatechuate dioxygenase (PCD), 2.5 mM 3,4-dihydroxybenzoic acid (PCA) and 1 mM Trolox (Aitken, Marshall, and Puglisi, 2008). After starting polymerization, 50 μl of the reaction mixture was added to the waveguides and data acquisition was started immediately.

To measure the photobleaching rate, 1 μL of phalloidin (66 μM) was added to the waveguides after 1 h to stabilize the formed filaments and prevent dissociation. Experiments were carried out on a home-built wide-field microscope system as described in chapter 2.

DNA measurements were carried out using 100 nM DNA, labeled with 4, 6 or 8 atto488 dyes in PBS. DNA was added to the waveguides after streptavidin incubation as described above. After incubation for 30 min and washing with PBS, acquisition was started.

TIRFM measurements Fluorescently labeled actin was also assayed in TIRF mode for functionality and to control that biotinylation of gelsolin did not affect its behavior. Actin filaments were imaged in TIRFM using the assembled flow chambers as described in chapter 2. The chambers were incubated with 0.15 mg/ml streptavidin for 5 minutes. After thorough washing, the biotinylated tethering protein was added and incubated for 10 minutes. After washing again, the actin mixture in polymerization buffer was added the same way as for the measurements in ZMW.

For actin nucleation measurements using spire, the measurement was started before flushing in the protein, so that the first steps could be imaged.

To measure the gelsolin capping behavior before mixing with polymerization buffer, 5 nM gelsolin or biotinylated gelsolin was added and incubated for 1 min prior to the measurement.

To compare biotinylated spire-ABCD with unbiotinylated spire-ABCD, 800 nM of 30% labeled actin-cy5 was imaged in TIRFM using myosin as the tethering protein. Actin was incubated before with 200 nM biotinylated spire-ABCD or unbiotinylated spire-ABCD for 3 min. The length distribution of the filaments was compared after 850 s. The exposure time during the measurement was 200 ms and the interframe time 1 s.

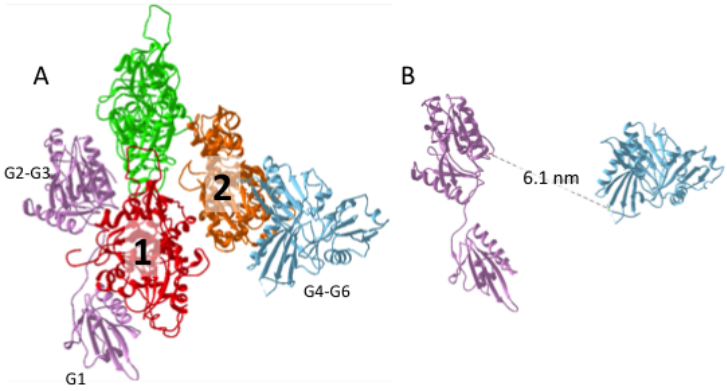

FIGURE 5.10: Structural model of gelsolin bound to the barbed end of an actin filament (three actin monomers depicted in red, orange and green). A: Alignment of the gelsolin domain structures bound to actin G1-G3 (pdb 1RGI, purple) and G4-G6 (pdb 1H1V, blue) to the filament barbed-end. The actin monomers labeled with 1 and 2 form a cross-dimer. B: The measured distance between the C-terminal amino acid of G3 to the N-terminal amino acid of G4.

Structural modeling Structural modeling was done by Jose Rafael Cabral Correia, working with Alvaro Crevenna, PhD at the Universidade Nova de Lisboa, Portugal. A structural arrangement was generated using Chimera (Pettersen et al., 2004). Since there is no structure of full-length gelsolin with actin bound, the available structures of gelsolin domains G1-G3 (1RGI, Burtnick et al., 2004) and G4-G6 (1H1V, Choe et al., 2002) with actin and Ca^{2+} were used. The actin of the G1-G3 gelsolin-actin complex was aligned to the terminal actin monomer within the filament structure (Fig. 5.10 A, Narita, Oda, and Maeda, 2011). The actin of the G4-G6 gelsolin-actin complex was then aligned to the monomer on the opposite strand within the filament. This arrangement corresponds to a cross-dimer configuration, which has been proposed before (Nag et al., 2013). The calculated distance between the C-terminal amino acid of the G1-G3 chain and the N-terminal amino acid of the G4-G6 fragment is about 6 nm (Fig. 5.10 B), which is too long to be traversed by the missing linker of about 40 amino acids. Since no other arrangement generated shorter distances, this suggests that further conformational changes take place during gelsolin-actin complex formation.

FCS measurements FCS experiments were performed on a home-built confocal fluorescence set-up. To passivate the surface, LabTek slides were incubated

with 10% BSA for 10 min. Atto488 labeled actin (90% labeled, Hypermol, Bielefeld, Germany) was incubated in Mg exchange buffer for 5 min on ice, then polymerization was started by adding KMEI buffer (100 mM KCl, 2 mM $MgCl_2$, 2 mM EGTA, 30 mM imidazole) to a final actin concentration of 10 to 500 nM. For higher actin concentrations, the content of labeled actin was reduced. FCS measurements were taken for 1 h in 10 min time intervals. When MiuA was added, a 5x or 10x excess of the actin concentration was added to actin in G-buffer and incubated for 3 min prior to adding the KMEI buffer. The measurement with 500 nM actin was first measured without MiuA, then MiuA was added and the same sample was measured again.

5.3 Pointed-end Actin Nucleation on Gelsolin

Dynamic intensity traces To investigate gelsolin-mediated actin filament formation, full-length gelsolin molecules were immobilized at the bottom of ZMW via biotin functionalization. The first surprising result was that the fluorescence intensity traces were very dynamic showing binding and dissociation of actin even beyond the formation of trimers and tetramers (Fig. 5.1 and 5.9). Traces indicative of filament growth also showed dynamics, although some appeared to stagnate around a certain intensity level (e.g. Fig. 5.1 B). The concentration of actin (1 μM) is above the critical concentration for pointed-end growth (600 nM) (Pollard, 1986) and, therefore, mainly continuous filament elongation was expected after formation of an actin nucleus. In order to investigate this discrepancy in more detail, the expected size distribution of filaments from literature values was compared with the measured data.

The size of the filaments formed on the apertures was estimated as described above by converting the intensity level into a monomer number after running a step-finding algorithm (Aggarwal et al., 2012) (Fig. 5.9 left y-axis) and then applying the intensity-to-monomer conversion algorithm as described in chapter 3 (Fig. 5.9 right y-axis).

Elongating filaments are uncommon Using the intensity-to-monomer conversion algorithm, the filament size in number of monomers per aperture at the end of the measurement with the expected behavior based on literature values could be compared. Overall, the observation of an elongating filament was an uncommon process, as only about 40% of all recorded traces had accumulated 6 or more monomers within 800 s (Fig. 5.12 A). In addition, the

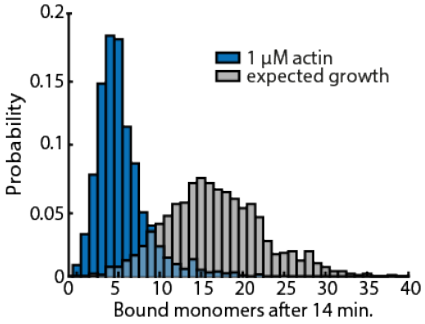

FIGURE 5.11: Distribution of filament lengths after 800 s. Blue: measured filament length distribution for 1 μM actin. Grey: expected behavior from a simulation using kinetic values from literature (chapter 3 for details), considering the measured photobleaching rate of 0.003 s^{-1}.

observed mean monomer number per filament at 800 s was 5 (Fig. 5.11), which is much lower than expected. Simulating the actin filament length distribution using actin nucleation and elongation values from literature as described in chapter 3 and incorporating a correction for photobleaching (0.003 s^{-1}, chapter 3) yielded a distribution centered at a peak probability of 15 monomers (Fig. 5.11).

An explanation would be that some of the surface-immobilized gelsolin has lost its capacity to bind actin monomers. However, as described above, the biotinylated gelsolin was functionally equivalent to its non-biotinylated form (Fig. 5.6) and surface-immobilization did not preclude its interaction with actin as filaments grow at longer timescales (Fig. 5.5). Therefore, neither photobleaching nor surface-induced artifacts can account for the observed filament size distribution.

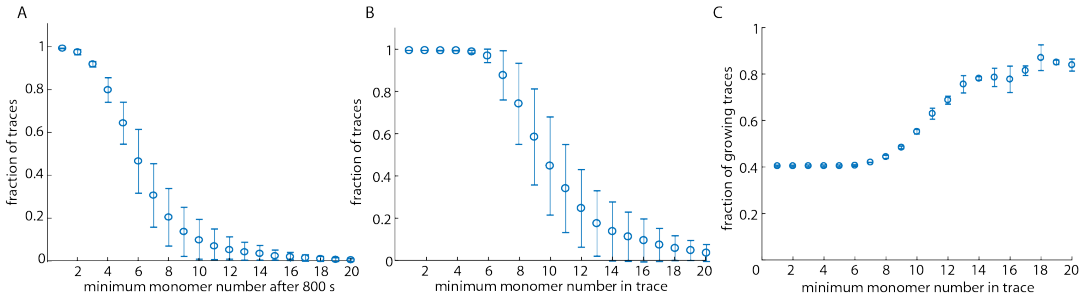

FIGURE 5.12: Statistics of oligomer growth. Fraction of oligomers that show at least 1,2,3...monomers at any time during the measurement (A) or after 800 s (B). C: Fraction of oligomers that show more than 6 monomers after 800 s after having reached at least n monomers at any time during the measurement. The error bars indicate the standard deviation of two independent measurements.

Oligomers do not elongate necessarily after reaching the nucleus size The nucleation-elongation model of actin filament formation predicts that, upon formation of a tetramer, all formed oligomers will continue to elongate as long as sufficient monomers are available (Sept and McCammon, 2001). In contrast to this expectation, although all individual traces reached at least four bound monomers at some point over the 14 minutes of observation (Fig. 5.12 B), only about 40% continued to grow (Fig. 5.11, 5.12 C).

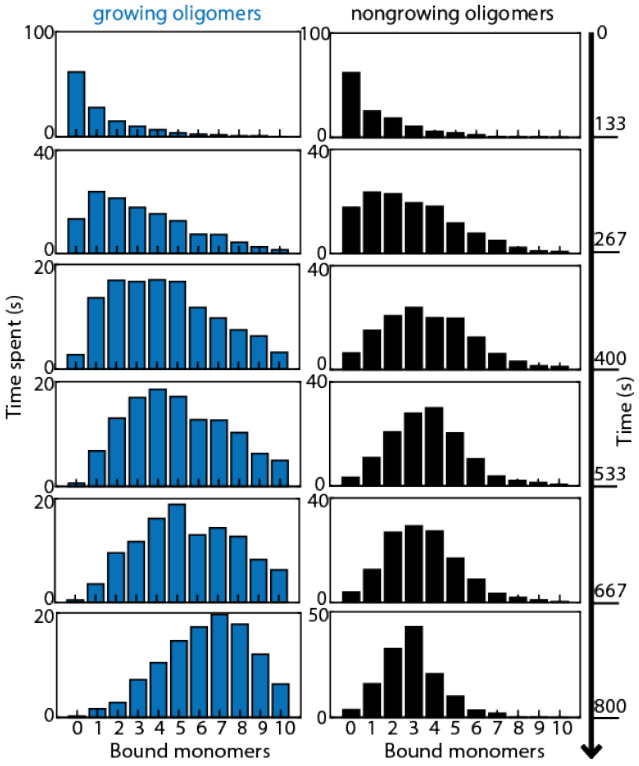

FIGURE 5.13: Visitation analysis on actin growing on gelsolin. The results from a visitation analysis showing the behavior of growing (blue) and non-growing oligomers (black). The total time oligomers of particular lengths were present during six time intervals of 133 s was calculated, covering the 800 s of the measurement.

Visitation analysis on actin nucleation on gelsolin reveals two populations To explore the origin of growth, I defined growing oligomers as those with more than 6 monomers at 800 s and non-growing oligomers were defined by having 4 monomers or less at this time point. Per 130 s time interval, the time a trace spent in a state with a certain number of bound monomers was calculated for both the elongating and non-elongating populations (Fig. 5.13). During the first 260 s, all oligomers showed identical size distributions (Fig. 5.13). After 260 s, the size distribution of the growing population shifted continuously over time towards larger monomer numbers (Fig.5.13), indicating filament

growth. This shift toward larger monomer numbers is independent of the oligomer size used to define the elongating population (Fig. 5.14).

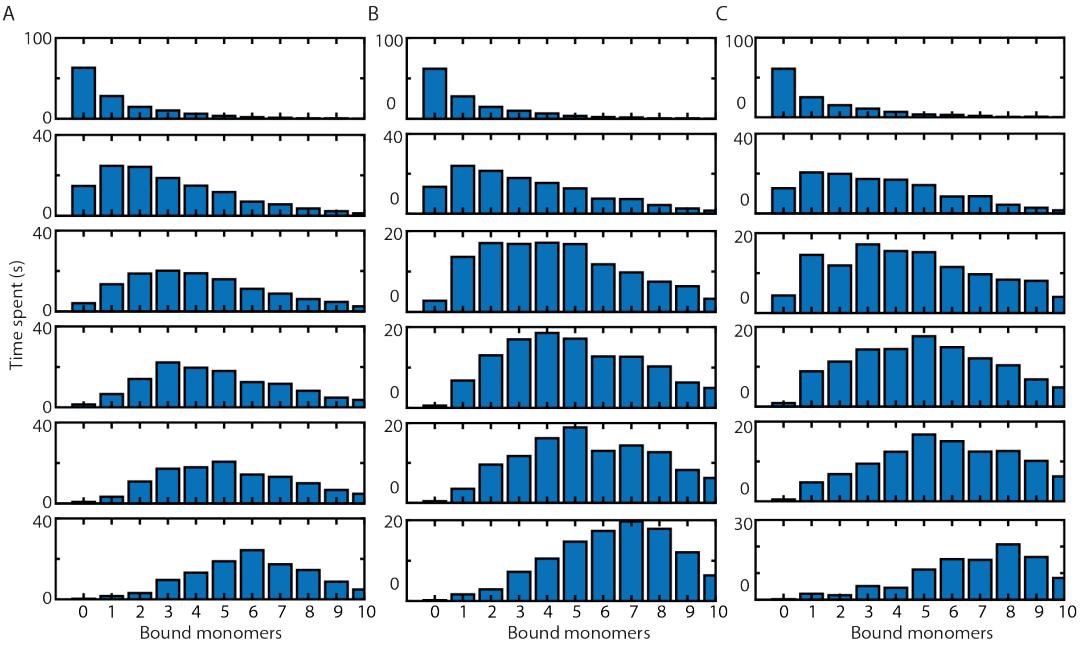

FIGURE 5.14: Visitation analysis on growing oligomers defined by those containing five monomers (A), six monomers (B) or seven monomers (D) after 800 s.

The monomer size distribution of the non-growing oligomer population shifted its mean value to a trimer level during the first 400 s and then dwelled at that level for the duration of the experiment. The observed peak in the non-growing oligomer size distribution suggests the presence of a preferred oligomer size that does not elongate. To test whether the two populations are an artifact of how the growing and the nongrowing populations were defined, I performed the same analysis on simulated data containing only one population. Artificially splitting these traces into two subpopulations could not reproduce the static behavior of the nongrowing population observed in the experiment (Fig. 5.15). Therefore, the finding of the two populations in the traces represents the existence of at least two oligomer assemblies.

Association rates differ for the two different populations Next, to gain insight into the differences between the growing and the non-growing oligomers, I analyzed the association and dissociation kinetics of the first six steps during oligomerization. The dwell-time histograms for the first six monomer association steps were calculated and fitted by a single exponential function as described in chapter 3 (Fig. 5.16 A, B). The estimated association rates revealed faster association rates for the non-growing population compared to

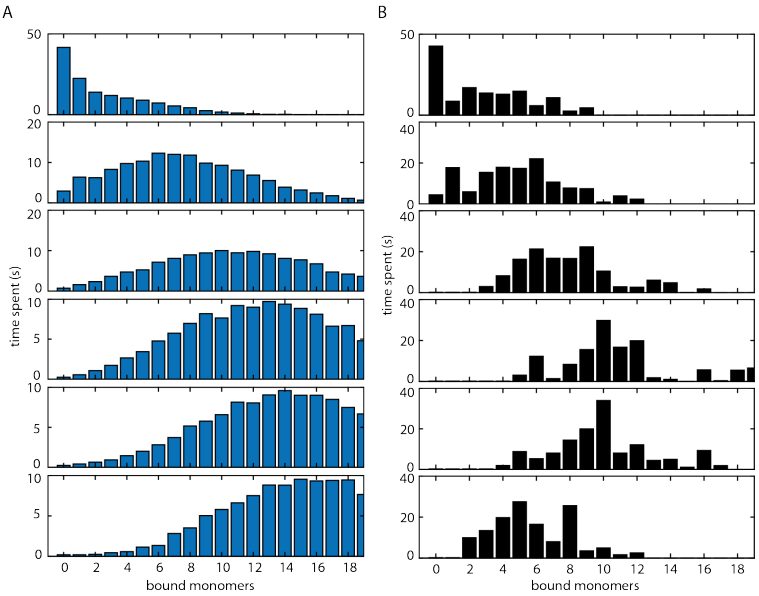

FIGURE 5.15: Visitation analysis on a simulation based on literature values, considering the experimentally determined photobleaching rate of 0.003 s^{-1}. The simulated traces were divided into a "growing" (A) and a "non-growing" (B) population based on the monomer number after 800 s. "Non-growing" show less than 4 monomers after 800 s, "growing" above 6 monomers.

the growing population (Fig. 5.16 B). The difference in association rates was not a result of the sorting procedure as artificially sorting traces from the same population gave identical association rates (Fig. 5.17).

Estimation of dissociation rates Dissociation events could not be accurately determined by the dwell-time analysis since the loss of signal due to photobleaching is indistinguishable from a dissociation event. Instead, dissociation rates were estimated indirectly by comparing the experimental results with that of a Monte Carlo simulation that considers the stochastic photobleaching process (see chapter 3). Off-rates have been estimated for nongrowing and growing oligomers separately (Fig. 5.16 D, Fig. 5.18, 5.19).

For the indirect estimation of dissociation rates, a model with 4 different on- and off-rates was used (3 individual monomer transitions plus elongation). The average trace of 2000 simulated runs were compared with the average of the experimental traces (chapter 3). To simplify the analysis, the association rates were fixed to the experimentally determined on-rates (Fig. 5.16). The individual off-rates were sampled and indicated the dissociation rate of the first monomer is slow, with an upper boundary of 0.001 s^{-1} (Fig. 5.19 C).

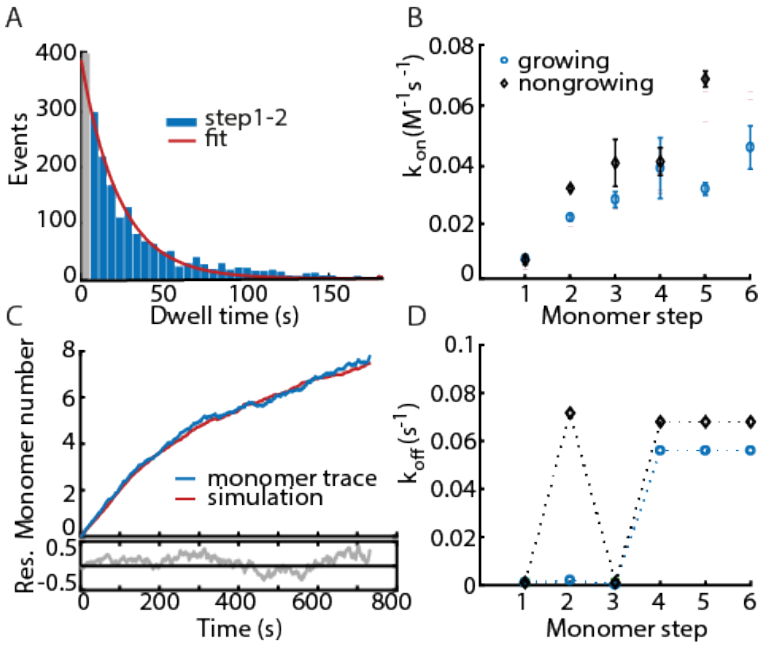

FIGURE 5.16: A kinetic analysis of gelsolin mediated nucleation. A: The dwell-time distribution of the second monomer-binding event is plotted (blue) and fit to a mono-exponential function (red). The first bin (grey) is not included in the exponential fit. B: Association rates k_{on} for the first six binding events for 1 μM actin growing on gelsolin. Growing filaments were defined as those with more than 6 monomers (bue circles), nongrowing filaments as those with less than 4 monomers after 800 s (black diamonds). C: The mean monomer trace of the growing oligomers (blue) and simulation considering photobleaching (red) and optimized values for the off-rates. D: Estimated dissociation rates for growing oligomers (blue) and nongrowing oligomers (black).

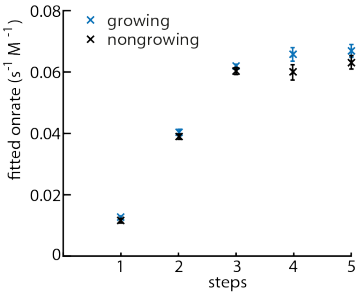

FIGURE 5.17: Association rates determined from a simulation using literature values (chapter 3). The simulated traces were divided into a "growing" (blue) and a "nongrowing" (black) species based on the monomer number after 800 s. The "nongrowing" species showed less than 4 monomers after 800 s, the "growing" species contained more than 6 monomers.

When optimizing the off-rates of the subsequent steps, it became clear that optimizing two different off-rates was not sufficient to describe the experimental average trace. Therefore, three different off-rates were optimized using the residual sum of squares (RSS) between the simulated average trace and the experimentally obtained trace (Fig. 5.18, 5.19). As a result, the RSS showed minimum values for a higher off-rate for the dimer and a slow off-rate for the trimer for both populations.

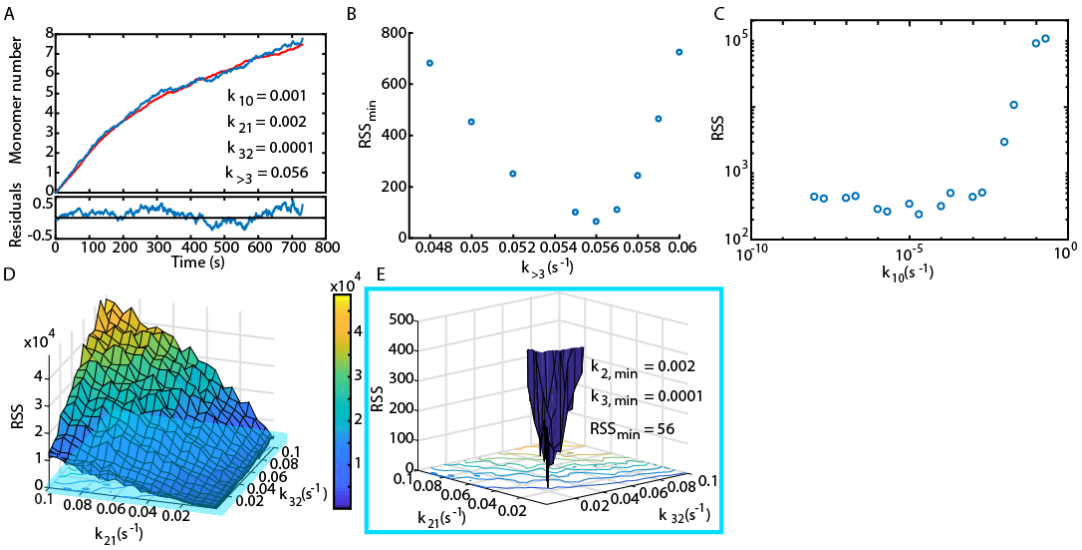

FIGURE 5.18: Off-rate estimation for growing oligomers. A: Comparison between the average of all growing oligomer traces (blue) and a simulation using the measured association rates and four different dissociation rates (red). The off-rates have been optimized to best describe the experimental data. B: The minimum residual sum of squares (RSS) error for the comparison between experiment and simulation for screening the off-rate of the fourth and subsequent steps. The RSS shows a minimum at 0.056 s^{-1}. C: RSS error screening for the off-rate of the first monomer. The RSS is plotted on a logarithmic scale. D: The RSS error for screening the off-rates of the second and third monomer. E: Zoom in of the region of (D) indicated by the blue box shows a clearly defined minimum in the RSS for an off-rate of the dimer of 0.002 s^{-1} and an off-rate of the trimer at 0.0001 s^{-1}.

Dimer stability determines the different populations The nongrowing population showed the highest off-rate for the dissociation of the second monomer, as well as for the fourth and subsequent monomers (Fig. 5.19). However, the trimer was stable with an off-rate slower than can be determined from the experiments (Fig. 5.19). For the growing oligomers, the dimer was estimated to be significantly more stable than for the nongrowing oligomers (Fig. 5.16 D, 5.18, 5.19). The estimated dissociation rate for polymerization (0.056 s^{-1}) agrees well with reported values (Schoepper and Wegner, 1991,

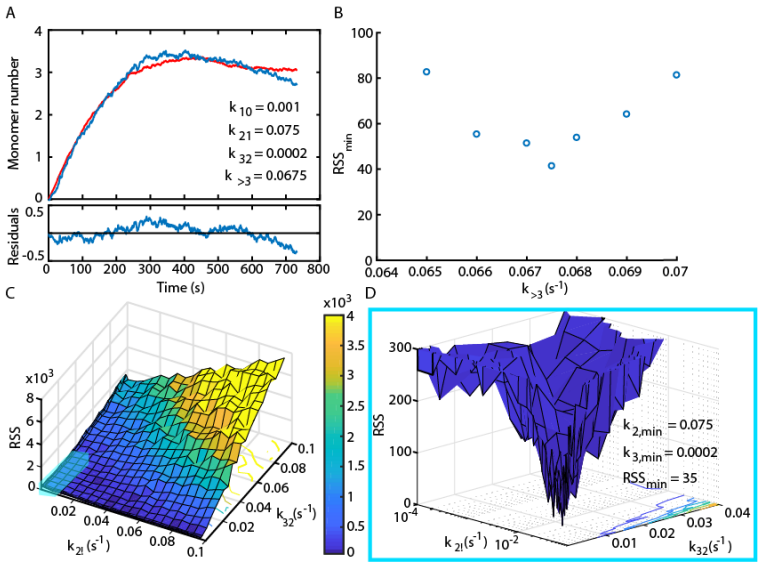

FIGURE 5.19: Off-rate estimation for non-growing oligomers assuming a slow off rate for the first step (0.001 s^{-1}). A: Comparison between the average of all growing oligomer traces (blue) and a simulation using the measured association rates and four different dissociation rates (red). The off-rates have been optimized to best describe the experimental data. The best fit of the dissociation rate for the second monomer was 0.075 s^{-1}, for the third monomer 0.0002 s^{-1}. B: The RSS error for the comparison between experiment and simulation for the screening of the off-rate of the fourth and subsequent steps. The RSS shows a minimum at 0.0675 s^{-1}. C: RSS error for screening the off-rates of the dimer and the trimer. D: Zoom in of the region in (C) indicated by the blue box shows a minimum in the RSS for an off-rate of the dimer of 0.075 s^{-1} and an off-rate of the trimer at 0.0002 s^{-1}.

Brangbour et al., 2011). Based on the estimated association rates, the critical concentration of gelsolin-mediated pointed-end filament growth is about 0.7 μM, in agreement with previous estimates (Pollard, 1986).

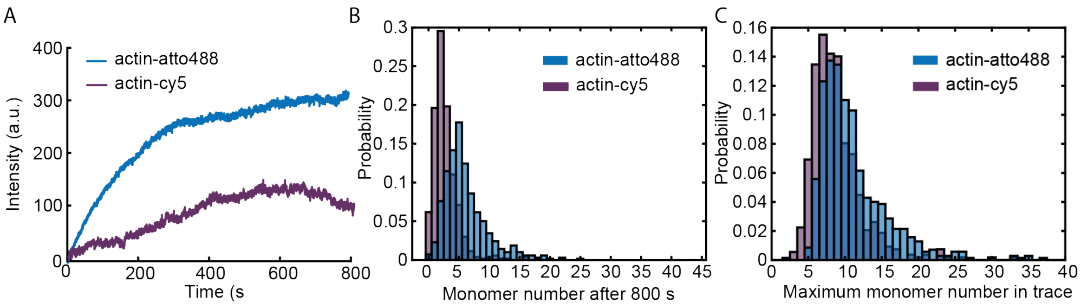

FIGURE 5.20: Comparison between actin-atto488 99% labeled and actin-Cy5 33% labeled growing on gelsolin. A: The mean monomer traces for actin-atto488, 90% labeled (blue) and actin-Cy5, 30% labeled (purple). B: The distribution of monomer numbers observed after a 800 s measurement. C: The distribution of maximum monomer numbers found in the traces during the 800 s measurement.

Actin-Cy5 shows the same behavior as actin-atto488 I repeated the gelsolin measurements with actin-Cy5 with 30% labeling efficiency to compare the findings with actin labeled with atto-488 (Fig. 5.21). Actin-Cy5 was fully functional (Fig. 5.7). Comparing the growth of actin-atto488 or actin-Cy5 on gelsolin, the results are similar when the difference in labeling efficiency and the different photobleaching rate between fluorophores are taken into account (chapter 3).

5.4 Barbed-end Actin Nucleation on Formin

To compare the findings for gelsolin-mediated pointed end growth to a more potent nucleator, I repeated the measurements with the FH2 domain of cappuccino using actin-Cy5. To be able to resolve the steps during a much faster barbed-end nucleation (Quinlan et al., 2007, Rosales-Nieves et al., 2006), I used actin with a labeling efficiency of 30%. Actin-Cy5 as well as biotinylated cappuccino were fully functional (Fig. 5.7). Actin-Cy5 and actin-atto488 showed a similar behavior during gelolin-mediated nucleation (Fig. 5.20).

Actin growing on cappuccino shows more growth and faster kinetics than on gelsolin Barbed-end nucleation via cappuccino showed more growth and faster kinetics than pointed-end nucleation via gelsolin (Fig. 5.21, 5.24).

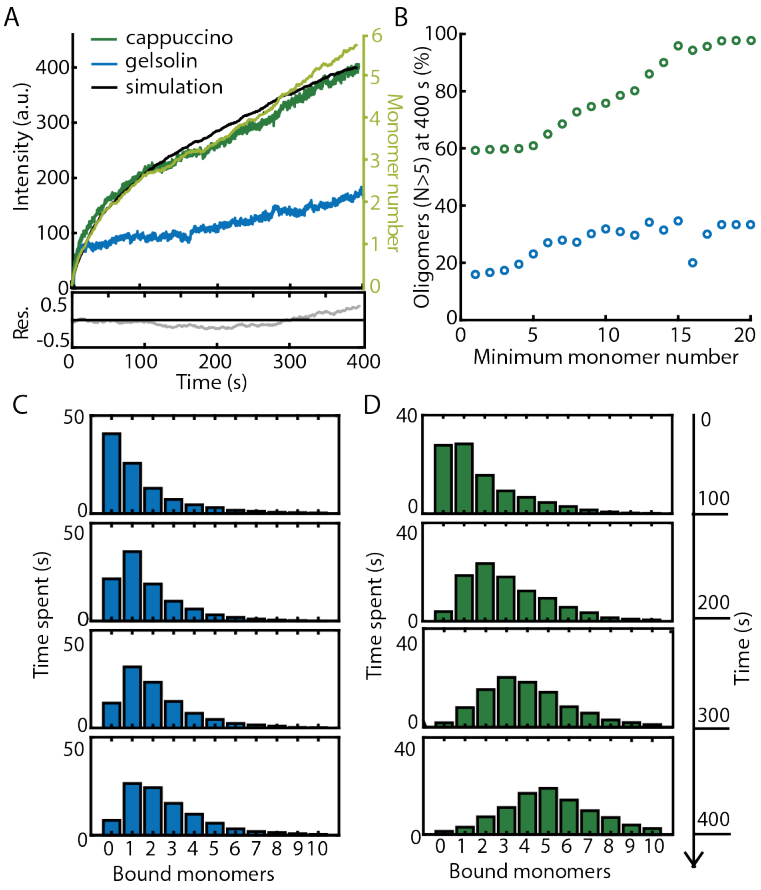

FIGURE 5.21: Barbed-end nucleation of actin-Cy5 on the FH2 dimer of cappuccino. A: Average intensity traces and monomer trace (light green) of actin-Cy5 nucleating on cappuccino (0.8 μM actin, green) and gelsolin (1 μM actin, blue). The degree of labeling was 30%. The black curve shows the result of a simulation using only one off-rate for every step with $k_{-}^{cap} = 0.051\ s^{-1}$. B: The percentage of oligomers consisting of more than 5 monomers after 400 s as a function of the minimum monomer number found in the trace during the measurement for cappuccino-mediated growth (green) and gelsolin-mediated growth (blue). Cappuccino-bound oligomers have a much higher probability to form growing filaments than gelsolin-bound oligomers. C, D: Visitation analysis of actin-Cy5 growing on gelsolin (C) and cappuccino (D) for all oligomers.

The average intensity trace showed about three times more growth for the cappuccino-bound oligomers in comparison to gelsolin-mediated growth (Fig. 5.21 A).

Actin growing on cappuccino forms stable oligomers Even very small oligomers bound to cappuccino have a high probability to form stable, growing filaments after 400 s, in contrast to gelsolin-bound oligomers (Fig. 5.21 B). A comparison of the visitation analysis for all oligomers and the growing oligomers supports the finding that for actin-Cy5 nucleating on gelsolin, some stable filaments can form while most of the population stays at one or two labeled monomers (Fig. 5.21 C), i.e. three to six monomers in total when considering the degree of labeling (Fig. 5.22). In contrast to the experiments with gelsolin, actin growing on cappuccino mainly consists of stable, continuously growing oligomers, as the oligomer size shifts towards higher monomer numbers over time (Fig. 5.21 D). The kinetics could be modeled with a single on-rate and a single off-rate (Fig. 5.21 A, 5.24, 5.22).

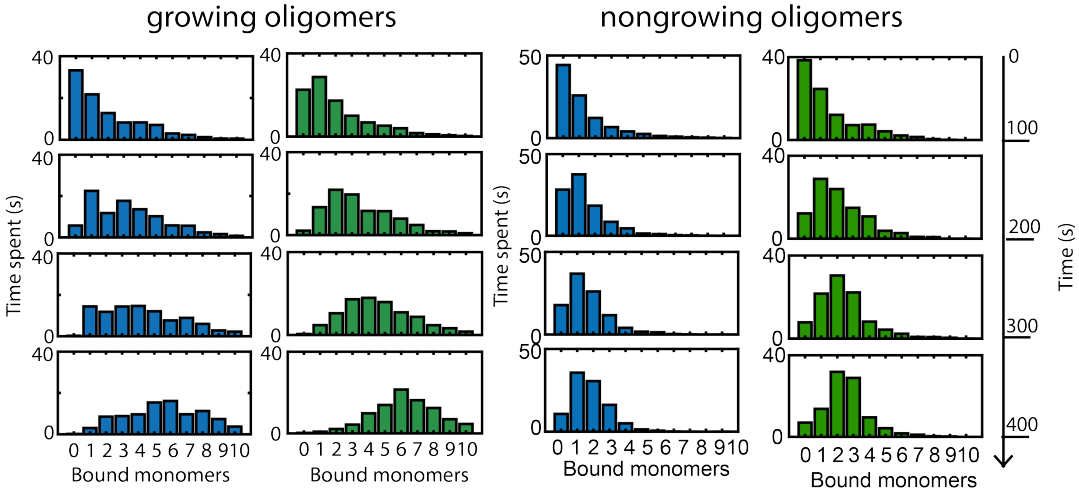

FIGURE 5.22: Visitation analysis for oligomers growing on gelsolin (blue) or cappuccino (green) for growing and nongrowing oligomers. Growing oligomers were defined to contain more than 5 monomers after 400 s, nongrowing oligomers were defined to contain less than 4 monomers after 400 s of measurement.

The measured kinetics are slower than expected Although the qualitative behavior of actin filament initiation with cappuccino is consistent with previous findings, the estimated association rate (0.081 s^{-1} or 0.24 s^{-1} for 0.8 μM actin when correcting for the labeling efficiency of the actin as described in chapter 4, Fig. 5.24 B) is far slower than expected for barbed-end elongation rates (Pollard, 1986).

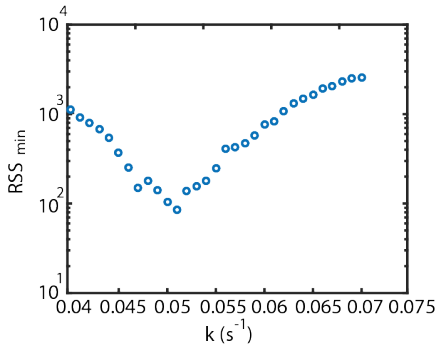

FIGURE 5.23: Off-rate estimation for oligomers growing on cappuccino. RSS error scan for the comparison between experiment and simulation assuming a single dissociation rate for all steps. A minimum was found at 0.051 s^{-1}.

To check whether this could be an artifact of the acquisition speed, I increased the acquisition rate from 5 Hz to 16.6 Hz. This resulted in an estimated association rate that increased by the same factor (0.24 s^{-1} or 0.72 s^{-1} when accounting for the labeling efficiency, Fig. 5.24 C). This suggests that there may be additional faster dynamics and that the current time resolution is not sufficient to reliably estimate such fast association rates.

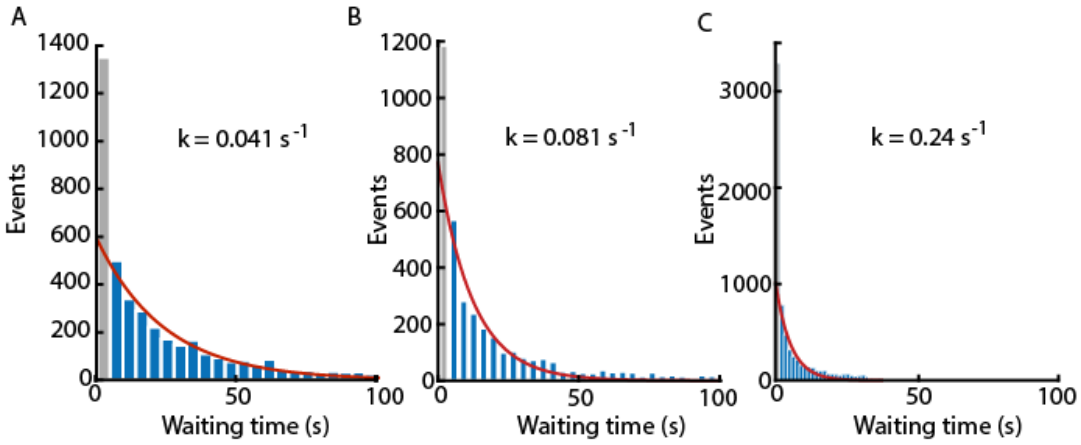

FIGURE 5.24: A: Waiting time distribution of all steps of actin-Cy5 growing on gelsolin with exponential fit (red). B, C: Waiting time distribution of cappuccino-mediated growth with exponential fit (red) of all steps measured with (B) 5 frames/s or (C) 16.6 frames/s.

5.5 Nucleation on Spire

TIRFM measurements Actin growth on spire-ABCD has been measured in TIRFM using 800 nM of 90% labeled actin-atto647. The TIRFM measurements

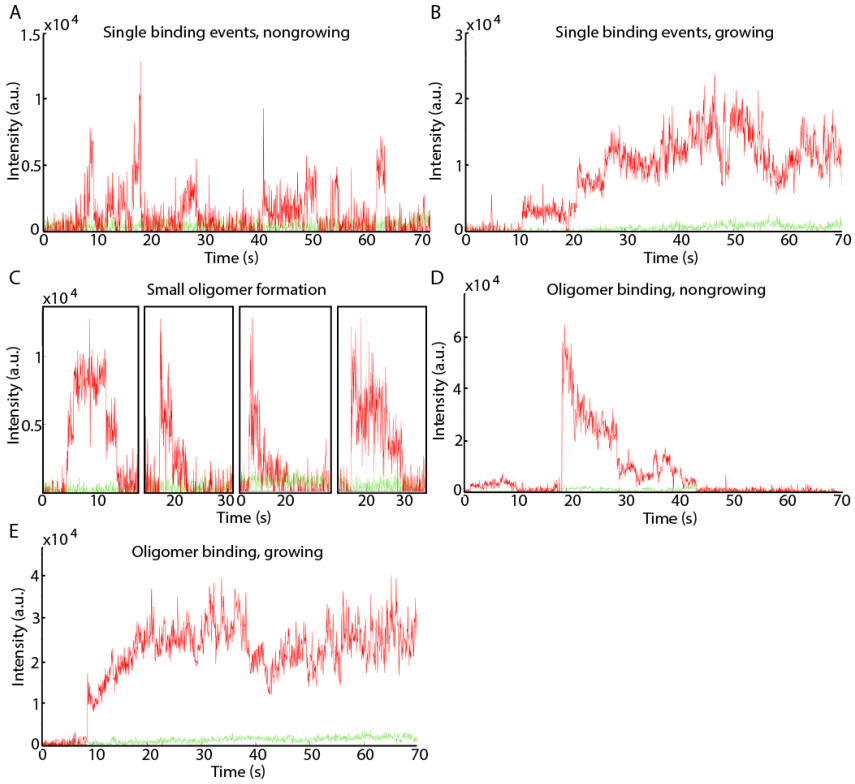

FIGURE 5.25: TIRFM traces of actin growing on spire-ABCD. Example traces (red) for the typical events of single monomer binding, either disassembling (A) or successfully growing (B), small oligomer formation (C) and oligomer binding followed by disassembly (D) or by further growth (E). The background intensity is depicted in green.

TABLE 5.2: Occurrences of the different types of events of actin growing on spire-ABCD measured in TIRFM. Total 1116 traces.

Event	Number of traces
Single binding events	438 (39%)
Small oligomer formation	505 (45%)
Oligomer binding followed by shrinking	78 (7%)
Oligomer binding followed by growth	21 (2%)

were done by Radoslav Kitel, PhD. In TIRFM, the spire molecules were immobilized via a streptavidin-biotin linker on the surface of a cover-glass directly. The measurement was started prior to flushing in the actin in polymerizing conditions, as in the ZMW experiments. After a drift correction, traces have been extracted like the traces measured in ZMW (see chapter 3).

Upon looking at the extracted traces, several typical events could be identified (Fig. 5.25). Either, single monomer binding events occurred, which disassembled or photobleached (Fig. 5.25 A), or could lead to successfull growth (Fig. 5.25 B). Furthermore, single binding events could also lead to the assembly of small oligomers, often trimers (Fig. 5.25 C), that disassembled or photobleached. Preformed oligomers assembled in solution could also bind to the surface-immobilized spire-ABCD, either followed by shrinking or by further growth (Fig. 5.25 D, E). In the case of further growth, often a dip in the intensity was observed prior to an increase in intensity, indicating elongation of the bound oligomer (Fig. 5.25 E).

An analysis of the occurrences of the different events showed that traces with mostly single binding events and traces showing small oligomer formation were most common. Oligomer binding followed by shrinking occurred in 7% of the traces, and oligomer binding followed by further growth occurred in only 2% of the traces (table 5.2).

Using the step-finding algorithm, I was able to look at the step size distribution of the different events to investigate the size of the oligomers binding to spire-ABCD (Fig. 5.26, 5.27). The step size distribution shows that the step size corresponding to a monomer binding event was around 3000 a.u. Interestingly, for oligomer binding events followed by growth, the distribution showed a peak at steps sizes corresponding to trimers and tetramers. For shrinking oligomers, step sizes corresponding to a pentamer or hexamer resulted in a small peak in the distribution (Fig. 5.26). In both cases, even higher step sizes

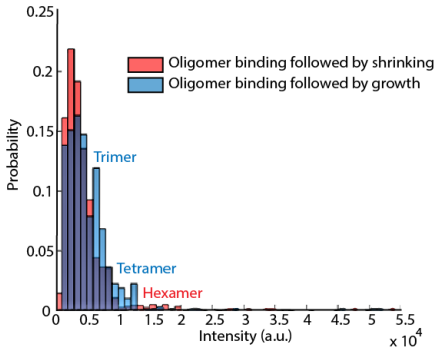

FIGURE 5.26: Step size distribution for oligomer binding events followed by growth or shrinkage. Step sizes were pooled for upward and downward steps. The labeling efficiency was at 90%, therefore, no further corrections were applied.

were detected, corresponding to larger oligomers formed in solution binding to spire-ABCD.

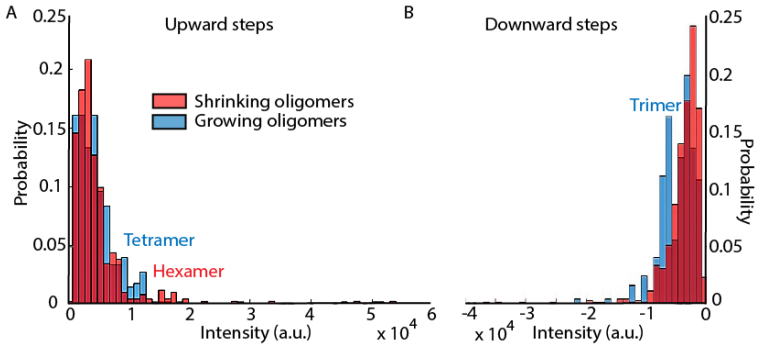

FIGURE 5.27: Upward and downward step size distribution for growing and shrinking oligomer binding events. Separated step size distribution for upward (A) and downward (B) steps for oligomer binding events followed by growth or shrinkage. The labeling efficiency was at 90%.

To be able to distinguish between upward and downward steps, the step size distribution was extracted for upward and downward steps separately (Fig. 5.27). For upward steps, tetramers or hexamers were more likely for growing or shrinking oligomers, respectively. This most likely corresponds to the binding of the oligomer formed in solution. For downward steps, growing oligomers showed an increased likelihood for the dissociation of trimers, whereas shrinking oligomers mostly dissociated single monomers at a time.

ZMW measurements Actin-Cy5 assembly on spire-ABCD measured in ZMW using 1 μM of 30% labeled actin-Cy5 (Fig. 5.28) showed little growth, corresponding to the single monomer binding events and small oligomer assemblies measured in TIRFM. The visitation analyis showed that only very

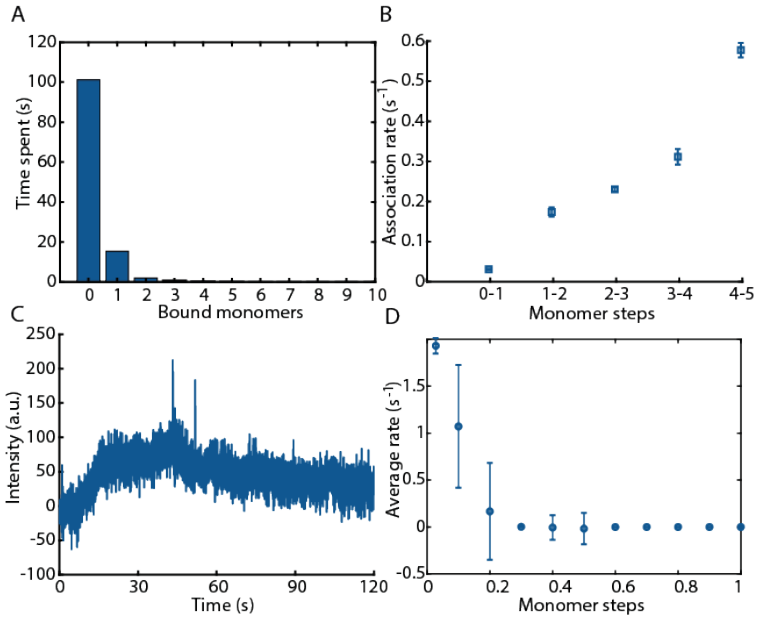

FIGURE 5.28: Actin-Cy5 growing on spire-ABCD measured in ZMW. Visitation analysis (A), dwell-time analysis (B) and the average trace (C) for 30% stochastically labeled actin-Cy5. The fractional average rates have been calculated using the time until the average trace reached the intensity corresponding to 0.1, 0.2,... monomers. Fractional average rates are 10 times faster than average rates, because only 1/10 of a monomer has to be reached. The photobleaching rate was measured to be 0.025 s^{-1} (chapter 3).

few monomers bind to spire-ABCD (Fig. 5.28 A). However, the association rates, as determined from the dwell-time analysis, showed increasing rates with oligomer size (Fig. 5.28 B). This is most likely due to the fact that, when filament growth is not very likely, only fast on-rates can lead to the assembly of higher oligomers, thus filtering the distribution of individual on-rates for the fast ones. This is then reflected in the dwell-time analysis, but not in the visitation and average rate analysis. The average rate showed decreasing rates with oligomer size, and the average trace indicates the formation of small oligomers (Fig. 5.28 C).

I compared the results of actin growth on spire-ABCD with simulated data affected by photobleaching and labeling efficiency (Fig. 4.11 E-H, chapter 4). The visitation analysis and average rate analysis applied to simulations of restricted growth, i.e. growth only until a certain monomer number, showed a good similarity. In this case, the influence of photobleaching and a labeling efficiency of less than 100% results in a decrease of apparent oligomer sizes, which shifts the distribution of the visitation analysis and causes the extracted average rates to decrease with oligomer size (Fig. 4.11 E-H, chapter 4).

5.6 Influence of Drugs on Actin Nucleation and Growth

5.6.1 Latrunculin A

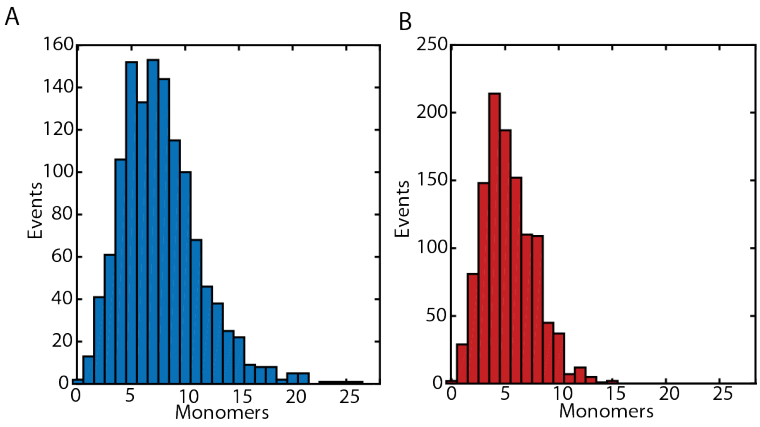

FIGURE 5.29: The maximum number of bound monomers during an individual trace. A: 1 μM actin, B: 1 μM actin with 10 μM LatA.

Actin flattening, the conformational change associated with the filament structure (Fujii et al., 2010, Oda et al., 2009), may be involved during the initial

phase of actin oligomerization. To investigate the contribution of flattening during nucleation, experiments of actin nucleating on gelsolin were repeated in the presence of saturating concentrations of Latrunculin A (LatA), a macrolide that binds within the nucleotide pocket (Morton, Ayscough, and McLaughlin, 2000) and blocks polymerization (Coué et al., 1987) by preventing the inter-domain motions that allow flattening (Rennebaum and Caflisch, 2012) (see also chapter 2).

Flattening occurs early during oligomerization and is necessary for growth In the presence of 10 μM LatA and 1 μM actin under polymerization conditions, traces show dynamics with length fluctuations up to over 10 monomers (Fig. 5.29). However, on average, only two monomers were bound over the 800 s of experimental observation and growth was not observed (Fig. 5.30, right column). Thus, LatA impairs the formation of both growing and non-growing oligomers that assemble in the absence of LatA. These results suggest that flattening of the actin molecule occurs during dimer or trimer formation and its occurrence is necessary but does not guarantee the formation of an oligomer that can sustain growth.

Flattening is required for the formation of a stable trimer For the average trace measured in the presence of LatA, only two different off-rates were necessary to describe the data (Fig. 5.32). In the presence of LatA, only the binding of the two first monomers was stable, while all subsequent monomer additions have a dissociation rate similar to the non-growing population (Fig. 5.31 D, 5.32). A comparison of the estimated dissociation rates for oligomers in the presence and absence of LatA showed the trimer level to be about two orders of magnitude more stable in the oligomers where flattening is allowed. The presence of LatA also increased the dissociation rates for oligomers larger than trimers by 35% compared to the growing population (Fig. 5.31 D). Thus, flattening is a key requirement during the formation of the trimer and it allows the formation of two different gelsolin-(actin)$_3$ arrangements.

Flattening is needed for filament elongation Flattening of the actin monomer is not only required for the formation of both dimer assemblies but it is also needed for filament elongation. These findings are supported by the fact that the probability of growth increases the longer the complex remains at a

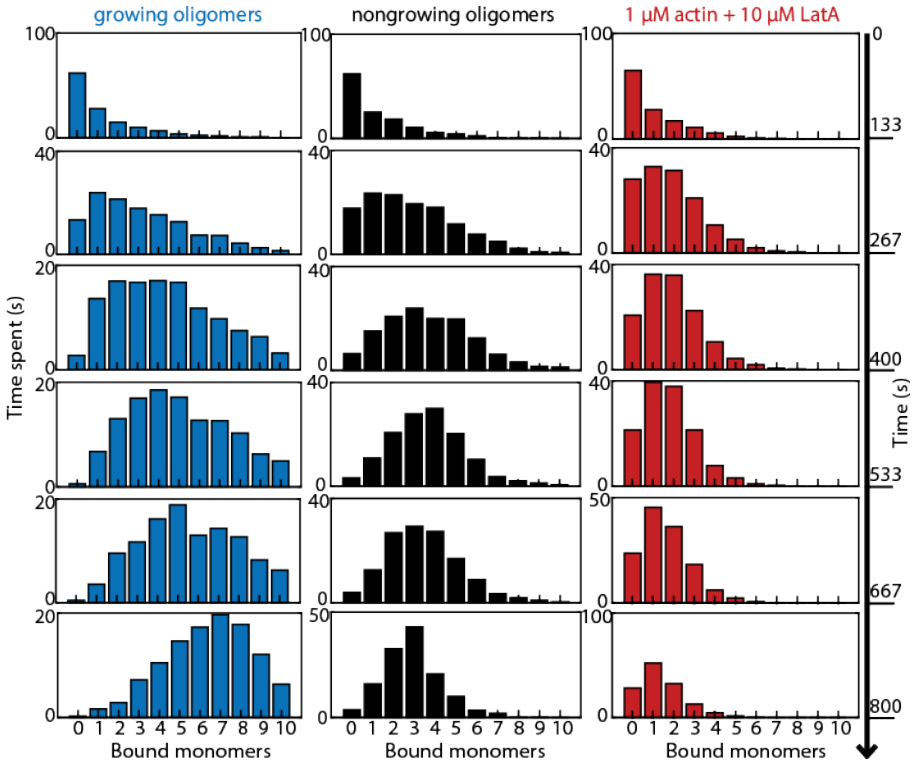

FIGURE 5.30: Visitation analysis on actin in the presence of LatA. The results from a visitation analysis showing the behavior of growing (blue) and non-growing (black) oligomers as well as the influence of LatA (red). The data for growing and non-growing oligomers has been shown before in Fig. 5.13). The total time spent in oligomers with particular lengths was calculated for six time intervals of 133 s each spanning the 800 s of the measurement.

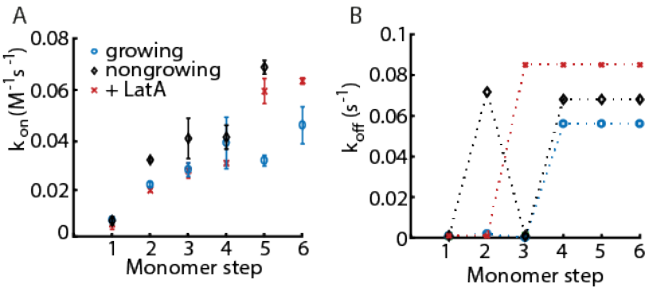

FIGURE 5.31: A kinetic analysis of nucleation. A: Association rates k_{on} for the first six binding events for 1 μM actin, in the absence and presence of LatA (red crosses). Growing filaments were defined as previously to contain more than 6 monomers (bue circles), nongrowing filaments to contain less than 4 monomers after 14 min (black diamonds). For higher oligomer numbers, association rates in the presence of LatA were fast, since only fast events could overcome the high dissociation rate (see panel B). B: Estimated dissociation rates using simulations (Fig. 5.32) for growing oligomers (blue), nongrowing oligomers (black) as well as monomers bound to LatA (red).

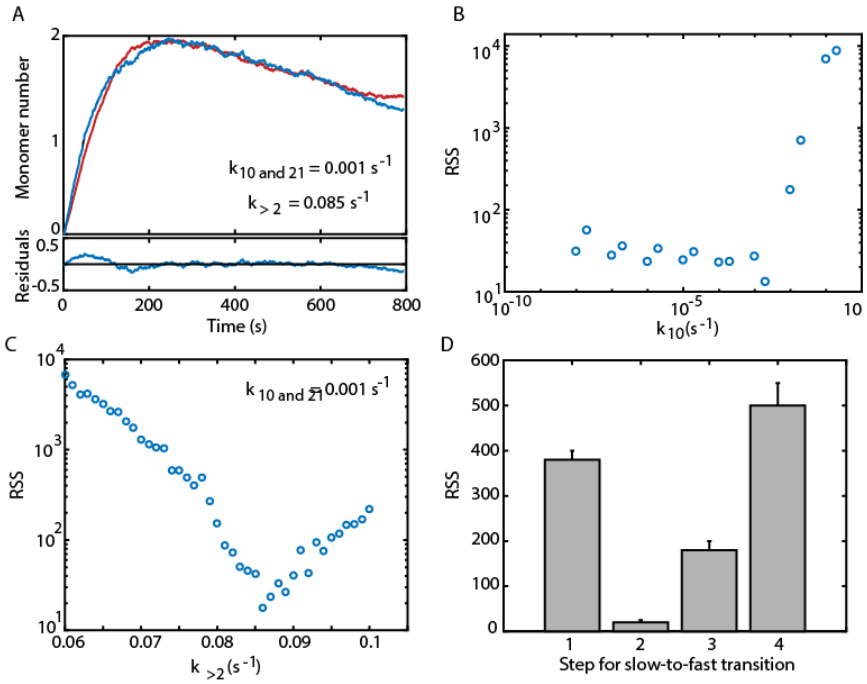

FIGURE 5.32: Off-rate estimation for oligomers with LatA. A: Comparison between the average of all growing oligomer traces (blue) and a simulation using the measured association rates and two different dissociation rates (red). The dissociation rate for the first two monomers was 0.001 s^{-1} and for each subsequent step 0.085 s^{-1}. B: The RSS error was scanned to determine the off-rate of the first steps. It shows an upper limit for the off-rates between 0.001 s^{-1} and 0.01 s^{-1}. C: RSS error scan for the comparison between experiment and simulation for a dissociation rate of 0.001 s^{-1} for the first three steps with a different dissociation rate for the subsequent steps. D: The best off-rate estimate determined from a RSS erroro scan for different transition points.

particular oligomer size (Fig. 5.33). The increase occurs at a dwell-time above 10 s, which is similar to the rate of ATP hydrolysis in growing polymers (Coué and Korn, 1986).

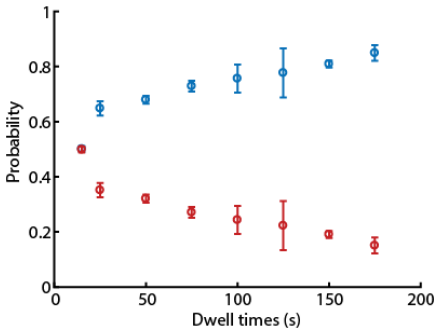

FIGURE 5.33: The probability for a step upwards depends on the dwell time of the previous step. The probability for a subsequent upward step (blue) and a subsequent downward step (red) is plotted against the dwell times of the previous step. The dwell times are binned into 25 s intervals, except for the first bin (15 s). Error bars represent the standard deviation of 2 independent measurements.

5.6.2 Miureanamide A

The effect of MiuA on actin oligomerization was characterized using FCS. 90% labeled actin-atto488 ranging from 10 nM to 500 nM was measured on a confocal microscope without or with 10x excess of MiuA. For measurements below the critical concentration of actin, the countrate without MiuA shows very little spikes, as only unstable and small oligomers are formed (Fig. 5.34 A, C). With 10x excess of MiuA, however, large spikes are visible in the counrate, which indicates the formation of large oligomers below the critical concentration (Fig. 5.34 B, D). The number and intensity of the spikes have been quantified (see chapter 3). For 100 nM actin, the number of spikes increases over the time course of 1 hour, whereas, without MiuA, no change in the number of spikes was visible and generally less spikes occurred (Fig. 5.34 E). Also, the intensity of the spikes showed a time dependency only in the presence of MiuA (Fig. 5.35 D). After 30 minutes, the spikes showed in increased intensity in units of the mode of the countrate of the measurement, indicating stable and growing oligomers.

The formation of small oligomers that are not visible as spikes was analyzed using the autocorrelation function of the countrate. For this analysis, the spikes were omitted. For 50 nM and 100 nM actin-atto488, the autocorrelation function showed a shift towards slower diffusion times (Fig. 5.35). A

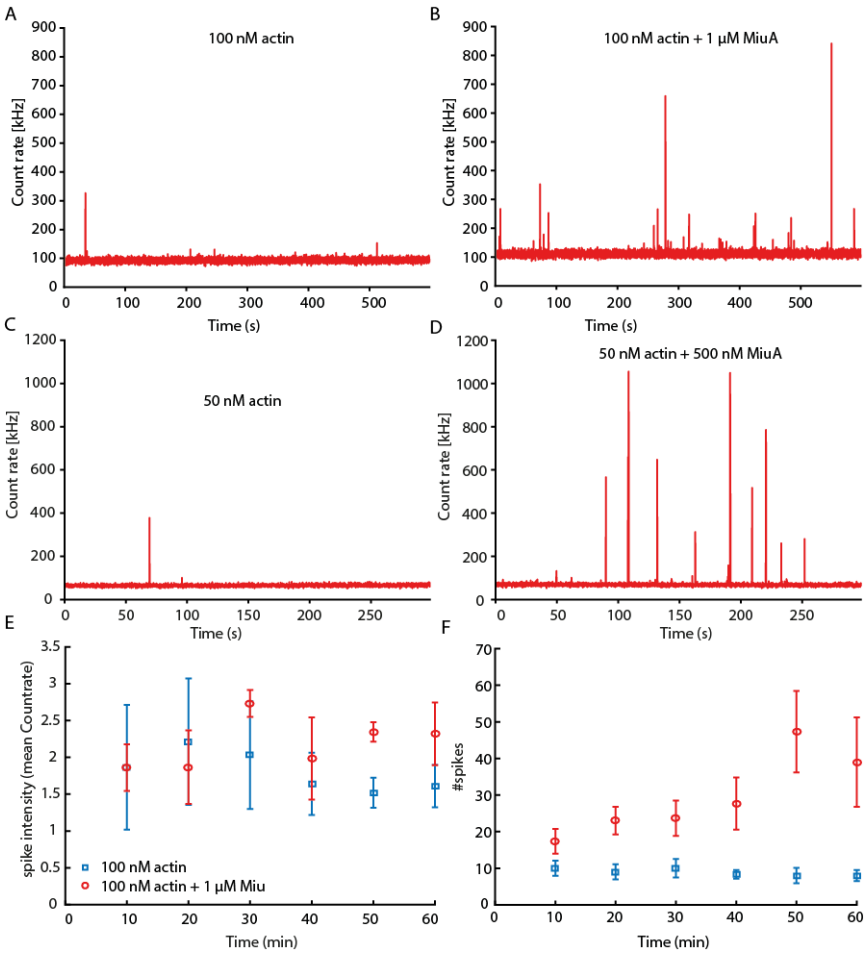

FIGURE 5.34: MiuA induces the formation of actin oligomers and lowers the critical concentration of actin polymerization. A, B: The countrate of 100 nM actin-atto488 after 1 h incubation as a function of time, without (A) and with (B) 10x excess of MiuA. B, C: The countrate as a function of time of 50 nM actin-atto488 after 1 h incubation, without (C) and with (D) 10x excess of MiuA. E: The mean spike intensity averaged over 10 min time intervals during a 1 h measurement. After 30 min of incubation, actin with MiuA shows spikes with a higher intensity than actin without MiuA. The intensity of spikes is given in units of the mode of the countrate of the respective measurement. Blue squares: 100 nM actin-atto488, red circles: 100 nM actin-atto488 and 1 μM MiuA. F: Number of spikes in 10 min time intervals over the course of the 1 h FCS measurement show with MiuA, up to 6 times more spikes are measured during the course of one hour. Errorbars represent the standard error of the mean of three independent measurements.

small shift in the autocorrelation function indicates a significantly bigger hydrodynamic radius, as will be discussed below.

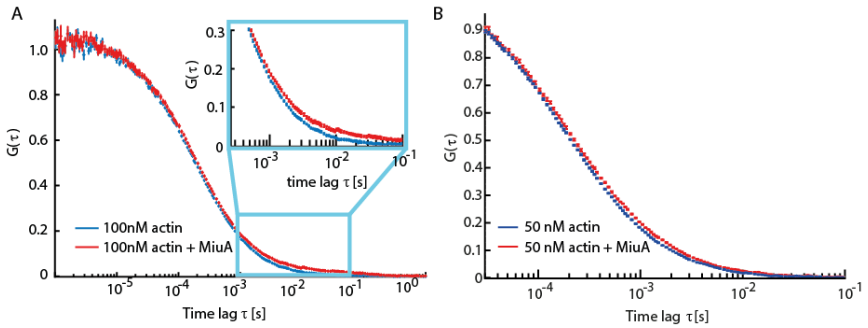

FIGURE 5.35: ACF of 100 nM actin (A) or 50 nM actin (B) with and without MiuA. Inset in A: detail at longer timescales showing the formation of small oligomers with MiuA. For the calculation of the autocorrelation function, the visible spikes were removed from the countrate.

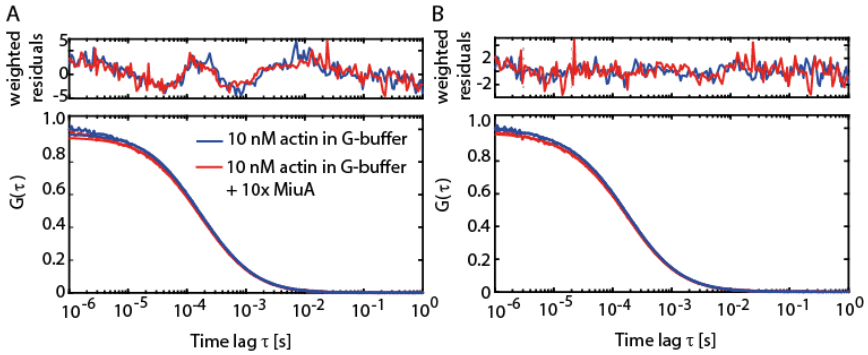

FIGURE 5.36: ACF curves of 10 nM actin-atto488 in G-buffer with and without MiuA. The autocorrelation function was fit using a one-component model (A) or a two-component model (B). The one-component model could not describe the data adequately, whereas a two-component model could describe the data better, but the results of the diffusion coefficients could not be interpreted meaningfully.

For quantification of the shift in the autocorrelation function towards larger diffusion times due to oligomerization, the autocorrelation function was fitted to obtain the diffusion constant of the measurements. It should be noted that the extracted diffusion constants are averaged over many different oligomers existent in solution. To be able to compare the apparent diffusion constant of measurements of oligomerizing actin to the diffusion constant of monomeric actin, a concentration far below the critical concentration of actin in G-buffer was measured (Fig. 5.36). However, a one-component fit of the autocorrelation function would not yield an acceptable fit (Fig. 5.36). However, the value for the diffusion coefficient was at 69 $\mu m^2/s$, which is expected for a protein of this size (He and Niemeyer, 2003). A two-component fit resulted in a good

fit, with a fast component of 115 $\mu m^2/s$ and a slow component of 20 $\mu m^2/s$. The slow component could be explained by the presence of actin oligomers, however, the fast component is too fast for an actin monomer and too slow for the possible presence of free dye. Thus, even though the one-component fit shows nonuniformly distributed residuals, its fit result of 69 $\mu m^2/s$ can be interpreted as an actin monomer, which should be the dominant species at this low concentration. At 10 nM actin in G-buffer, MiuA has no influence on the autocorrelation function (Fig. 5.36).

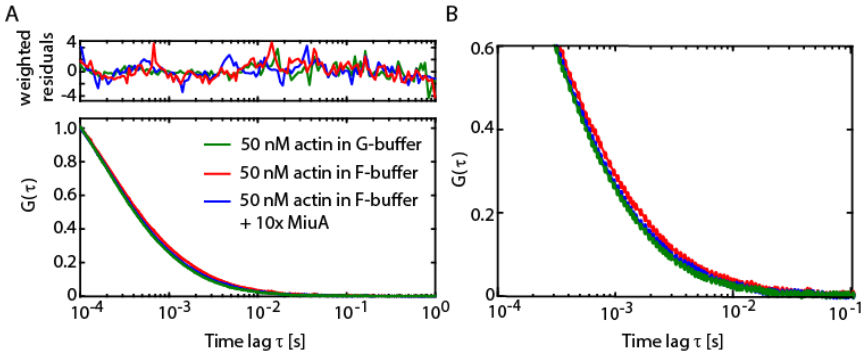

FIGURE 5.37: ACF of 50 nM actin-atto488 with and without MiuA in G-buffer and in F-buffer. A: A one component fit of the autocorrelation function, which could describe the data. The weighted residuals are shown in the upper panel. B: A zoom-in of panel (A) reveals a slight shift towards longer diffusion times under the influence of MiuA.

The measurement of actin in G-buffer was repeated for 50 nM actin and compared to 50 nM actin in F-buffer, i.e. polymerizing conditions without and with MiuA (Fig. 5.37). Here, an acceptable one-component fit of the autocorrelation function could be obtained with a cut-off at 10^{-4} s, which could not be achieved for 10 nM actin. Qualitatively, a slight shift towards longer diffusion times was observed with a 10x excess of MiuA, whereas polymerizing conditions alone did not induce much visible oligomerization (Fig. 5.37 B).

For measurements of 100 nM, 250 nM and 500 nM actin, similar fits could be obtained (Fig. 5.38, table 5.3). Since the diffusing species in solution were a mixture between monomers and oligomers of different sizes, the thus obtained diffusion constants were apparent diffusion constants from a one-component fit like in Chakraborty et al., 2012. The thus obtained apparent diffusion constants are summarized in table 5.3. For calculation of the autocorrelation functions, spikes have been excluded in the analysis to obtain information

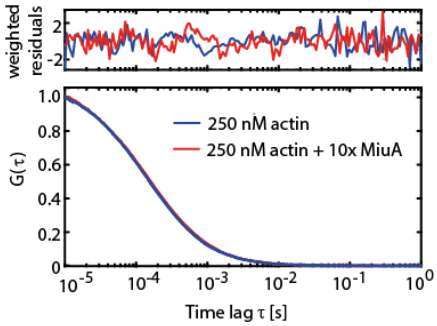

FIGURE 5.38: ACF of 250 nM actin after 10 min after inducing polymerization. A one component fit could describe the data. The weighted residuals are shown in the upper panel.

about the small oligomers, in contrast to the spike analysis, which contains information about larger oligomers (Fig. 5.34).

For 100 nM actin, MiuA induced oligomerization directly after inducing polymerization (table 5.3). After 1 h, however, there was no difference in the extracted diffusion constant, probably because the oligomers have grown in size and are therefore excluded in the analysis. This assumption was supported by the fact that the number of molecules in the observation volume N decreased after 1 h and spikes appeared in the countrate (Fig. 5.34 D). After 1 h, the measurement with MiuA shows quantitatively more spikes with a higher intensity than the measurement without MiuA (Fig. 5.34 E, F). This lowers the concentration of free actin monomers and small oligomers, which results in a lower N.

For 250 nM actin, there is not much difference in the diffusion constants in the first hour of the measurement. Afterwards, the diffusion constant in the presence of MiuA is faster than without MiuA (table 5.3). However, since this concentration is above the critical concentration for actin growth, after 1 h, an equilibrium has been reached with more larger, stabilized oligomers in the presence of MiuA than with actin alone. The larger oligomers are excluded in the analyis. As for 100 nM actin, filament formation lowers the number of free actin molecules N in solution. Due to the reduced concentration of free monomers, the assembling oligomers were smaller in size, resulting in a higher diffusion constant.

For 500 nM actin, actin was first measured without MiuA, then 10x excess of MiuA was added to the same actin after 5 min. The diffusion constant was reduced within 5 min by the addition of MiuA. This indicates that MiuA

TABLE 5.3: Apparent diffusion constants D_{app} and apparent N_{app} of actin with and without 10x excess of MiuA. Errors indicate the standard deviation of 3 independent measurements. The values were obtained using a one-component model considering the triplet state. The triplet state was fitted globally for all measurements of one concentration.

[actin]	time lag	D_{app} ($\mu m^2/s$)		N_{app}	
MiuA		-	+	-	+
100 nM	0	66 ± 1	41.7 ± 0.6	0.35 ± 0.02	0.72 ± 0.08
	1 h	69	64 ± 1.4	0.46	0.22 ± 0.01
250 nM	0	64	63	2.51	2.55
	10 min	66	61	2.35	2.63
	1 h	54	63	3.09	1.89
500 nM	0	51		8.18	
	2 min	50		7.61	
	4 min	68		6.20	
	10 min		44		7.6
	12 min		40		7.1
	15 min		40		6.8

stabilizes small oligomers formed during the assembly of actin, leading to more and larger actin oligomers or filaments, which leads to an increase in the number of omitted spikes.

5.7 Discussion

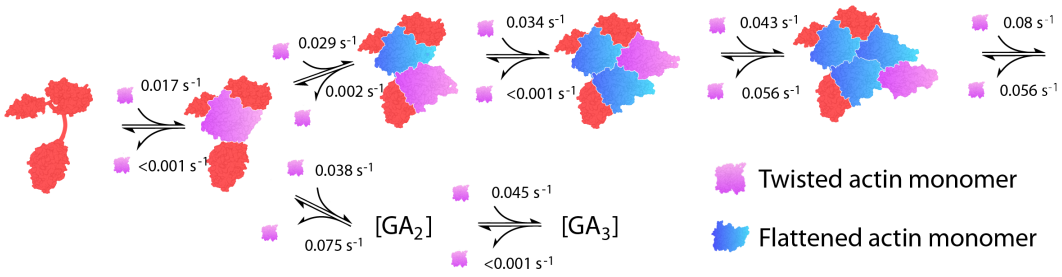

FIGURE 5.39: Gelsolin-mediated actin filament nucleation model. Calcium-activated Gelsolin is colored red. Monomeric twisted actin is depicted in purple whereas flattened actin is depicted in blue. A newly bound actin monomer is twisted and it flattens upon the addition of a subsequent monomer. Two different dimers [GA_2] complexes can form. One of these dimers can lead to successful polymerization (upper pathway), the other one has a high off-rate and is unable to act as a seed for actin nucleation (lower pathway).

Nucleation on Gelsolin ZMW measurements of actin-atto488 nucleating on gelsolin showed that filaments had a very dynamic behavior with many upward and downward steps in the intensity and thus in oligomer size (Fig. 5.9). Furthermore, successfully elongating filaments were not the rule (Fig. 5.1). The reduced fraction of elongating filaments could not be explained by photobleaching or by non-functional protein, as filaments were shown to grow in a photobleaching experiment of stabilized filaments (Fig. 5.5). Even after reaching the nucleus size, filaments did not necessarily grow (Fig. 5.12). The visitation analysis revealed two populations. For one, the average oligomer size was continually growing over time, for the other one it stagnated at about three monomers (Fig. 5.13). A dwell-time analysis of the association rates revealed that the growing population had slower association rates compared to the nongrowing population (Fig. 5.16). An explanation for the instability of the nongrowing population could be found in the dissociation rates, which have been estimated indirectly due to the indistinguishability of dissociation steps and photobleaching steps (Fig. 5.16). The critical concentration calculated from the determined association rate and the estimated dissociation rates for gelsolin-mediated pointed-end filament growth was at 0.7 μM, in agreement with the literature value (Pollard, 1986). The nongrowing population had a faster dissociation rate from four oligomers onwards, and additionally a faster dissociation rate for the dimer, which the growing population did not have (Fig. 5.16).

These results indicate that two dimer conformations can assemble upon the arrival of the second monomer to the gelsolin-actin complex (Fig. 5.39). The faster assembling arrangement allows for incorporation of subsequent monomers, although the assembled complex is unstable and long-term growth inhibited. The other arrangement binds the third monomer more slowly, but the complex is stable and can elongate (Fig. 5.39). The high dissociation rate of the second monomer in the nongrowing population may allow for the conversion of the complex into the more stable arrangement that allows for growth on longer timescales (Fig. 5.5).

This suggests the existence of at least two structurally different GA_2 complexes (Fig. 5.39). It is possible that the non-growing oligomers represent an arrangement similar to those previously reported as AP-dimers, which do not undergo polymerization (see chapter 2) (Hesterkamp, Weeds, and Mannherz, 1993, Qu et al., 2015). The different association rates for the two

populations suggest that the initial arrangement within the GA_2 complex propagates cooperatively within the filament lattice. Long-range cooperativity of conformational changes lasting over 100 monomers in the filament has been suggested before on actin nucleated by gelsolin (Orlova, Prochniewicz, and Egelman, 1995) and on actin filaments bound to laterally binding proteins (Crevenna et al., 2015). The faster association rates of the non-growing population explain how this species dominates in competition for monomeric actin (Fig. 5.39). In bulk experiments, gelsolin was described to not be a true nucleator because of the still-existing lag-phase even with gelsolin present (Coué and Korn, 1985). The non-growing population observed here could explain the lag-phase, as in bulk essays only the filament mass is measured (see chapter 2) and small oligomers cannot be detected.

In conclusion, with the aid of ZMW, gelsolin-mediated actin nucleation was observed directly on the single molecule level. The ZMW measurements revealed two populations, a growing and a non-growing population.

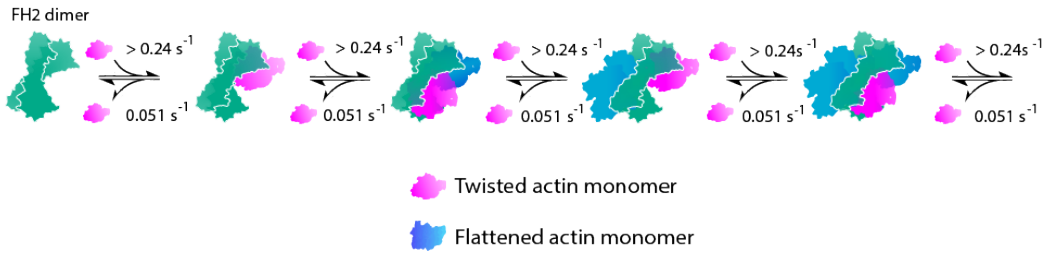

FIGURE 5.40: Actin nucleation model in the presence of cappuccino. Monomeric twisted actin is depicted in purple whereas flattened actin is depicted in blue. The FH2 domain of cappuccino is depicted in green. Actin filament initiation and elongation are well described by a single association and dissociation rate constant.

Nucleation on Cappuccino In contrast to gelsolin-mediated nucleation, oligomers formed in the presence of the FH2 domain of cappuccino showed continuous growth and displayed a high probability that even small oligomers form filaments (Fig. 5.21). The measured association rates were faster than for gelsolin-mediated growth. The kinetics of filament growth could be described by a single association rate and a single dissociation rate (Fig. 5.23). However, the association rate, which then is equivalent to the elongation rate in this model, is slower than expected (Pollard, 1986; Crevenna et al., 2015; Kuhn and Pollard, 2005).

The photobleaching rate of actin-Cy5 showed a double-exponential decay as expected for Cy5 (Füreder-Kitzmüller et al., 2005). The slower rate was

0.025 s^{-1}, which corresponds to 3.5% of the extracted on-rate corrected for the labeling efficiency (0.72 s^{-1}). This corresponds to the highest photobleaching rate used here in the simulations (3% of the on-rate). For the average rate analysis a photobleaching rate of 3% results in a decrease and even a cut off of the extracted rates (chapter 4). This explains the decrease of the average rates for actin-Cy5 growing on cappuccino.

To verify the influence of the sampling rate on the dwell-time analysis as done in the simulations (chapter 4), the sampling rate was increased from 5 Hz to 16.6 Hz. This resulted in an increase of the estimated association rate (0.24 s^{-1} or 0.72 s^{-1} when accounting for the labeling efficiency of 30%, Fig. 5.24). However, the extracted rates are still slower than expected (Pollard, 1986; Crevenna et al., 2015; Kuhn and Pollard, 2005). For association rates on the order of 10 $\mu M^{-1}s^{-1}$ and a labeling efficiency of 30%, the necessary sampling rate for the dwell-time analysis is at 60 s^{-1} (20·0.3·10 s^{-1} = 60 s^{-1}), as the dwell-time analysis yields trustworthy rates at more than 20 times the expected association rate (chapter 4). This suggests that the current time resolution used in these experiments is not sufficient to reliably estimate such fast association rates with the dwell-time analysis. The visitation analysis and the average rates, however, indicate fast actin assembly as expected for a mechanism circumventing the nucleation phase via a strong nucleator (Fig. 5.21, 5.22).

Another reason for the slow association rates could be the geometry of the zero-mode waveguides. In some experiments using ZMW, kinetics have been decreased by up to an order of magnitude (Christensen et al., 2016; Uemura et al., 2010). Uemura et al increased the concentration more than 20x compared to bulk measurements to enhance the arrival rates to the apertures (Uemura et al., 2010).

To quantify the influence of the ZMW geometry on diffusion-limited association rates, I proposed a system with single-stranded DNA oligonucleotide as a tethering anchor at the bottom of the ZMW, and DNA double strands of different sizes with the complementary linker to the tethering DNA strand as the diffusing species. Alternatively, also proteins of different sizes could be used instead of the DNA double strands, to investigate the influence of ZMW on the diffusion of differently sized and shaped molecules. The on and off kinetics of the DNA annealing at the bottom of the ZMW could then be compared for different diffusing species, as well as for different sizes of

the apertures. As a comparison, the annealing kinetics could be measured in TIRFM on a planar surface without the influence of the apertures.

Nucleation on spire In contrast to cappuccino, where dwell time analysis, visitation analysis and average rate analysis indicated continuous growth, actin on spire-ABCD assembled only to smaller oligomers in ZMW (Fig. 5.28). In TIRFM, also mostly single binding events or the assembly of small oligomers was observed. In some cases, however, oligomers that had formed in solution bound to the surface-bound spire-ABCD, which could lead to further growth or shrinkage (Fig. 5.25). These oligomer binding events were not observed in the ZMW. This could be explained by the geometry of the waveguides, which decreases the probability that larger structures diffuse into the wells where they could bind to the tethering protein. An effect of the waveguide geometry on the diffusion behavior of proteins has been observed before (Christensen et al., 2016, Uemura et al., 2010).

This could also be a possible reason for the reduced elongation rates found for actin growing on cappuccino. In solution, small oligomers could bind to the elongating filament, thereby enhancing the elongation rate. This is reduced or not happening in ZMW, therefore the overall rate decreases.

In ZMW and in TIRFM, mostly traces with single monomer binding events have been observed, that lead to small oligomer assembly of up to four monomers. The visitation analysis, average traces and average rates resemble a simulation of hindered growth, where oligomers can assemble up to four monomers and then stop growing (chapter 4). In the simulation, photobleaching and the degree of labeling were included. Thus, the results indicate that spire-ABCD can bind actin monomers, but is insufficient to promote nucleation starting from the monomers alone. This has been suggested before (Dominguez, 2016). However, in solution, spire-ABCD could capture preformed oligomers and stabilize them to enable further growth, as the TIRFM measurements indicate. The step size analysis indicated that trimers and tetramers are more likely to successfully grow further, whereas hexamers are likely to dissociate. This could be explained by the binding of a tetramer to the four WH2 domains of spire, which can then be stabilized or even rearranged for futher growth. The hexamer could bind to spire, but in a way that hinders further growth, perhaps due to steric hindrance.

When oligomer binding was followed by further growth, often a dip in intensity was observed prior to the increase in intensity indicating growth (Fig. 5.25). This could be due to a rearranging or even removal of monomers to achieve the correct conformation for elongation. Another possibility is that the increased excitation intensity in the evanescent field leads to photobleaching of the newly bound monomers. Upon incorporation of new monomers, this effect is surpassed by growth and the intensity increases again.

These results indicate that spire is not sufficient to nucleate actin efficiently on its own, but can enhance primary nucleation by the stabilization of self-assembled oligomers. In cells, spire is likely to cooperate with cappuccino to nucleate actin (Quinlan, 2013), which could explain the low nucleation capacity of spire alone. A different view is that the physiological role of spire is not predominantly actin nucleation, but barbed end capping (Montaville et al., 2014). Further experiments could be done with the spire dimer as a tethering protein in TIRFM or ZMW, which would be expected to show a strong nucleation activity.

The influence of actin binding drugs

Latrunculin A Repetition of the experiments using actin-atto488 growing on gelsolin in the presence of LatA showed some interesting results. The coupling between filament growth and flattening, which is inhibited by LatA (see chapter 2), becomes obvious as the results showed that flattening occurs early during oligomerization and is a requirement for stable growth (Fig. 5.30). Flattening occurs already at an oligomer size of dimers and trimers (Fig. 5.31) and it is required to stabilize the nascent filament lattice (Fig. 5.30).

The increase in the dissociation rate of oligomers by the presence of LatA suggests that flattening must occur quickly upon the addition of a monomer. Since flattening is associated with ATP hydrolysis (Blanchoin and Pollard, 2002, McCullagh, Saunders, and Voth, 2014), this implies that probably only the terminal monomer contains ATP and is thus in the twisted geometry (Fig. 5.39), which agrees with previous estimates that gelsolin-capped filaments hydrolyze ATP rapidly (Coué and Korn, 1986).

The occurrence of flattening already during dimer formation may lead to ATP hydrolysis also taking place within small oligomers. The hydrolysis and flattening required within these oligomers, and not instability of dimers

and trimers, may be the origin of the observed lag phase in bulk assays during filament formation of pure actin solutions. Within this framework, nucleator proteins function by biasing dimer arrangements towards those that can better sustain elongation. The mechanistic difference between strong and weak actin filament nucleators would be the efficiency by which they bias dimer arrangements towards elongation-prone complexes.

Miuraenamide A The results of the FCS measurements of actin assembly with and without MiuA suggest that MiuA favors polymerization by stabilizing the early stage oligomers formed during nucleation within 5 min of incubation. At concentrations above the critical concentration, MiuA induced the formation of larger filaments than observed for actin alone (table 5.3). Below the critical concentration, MiuA induced the formation of filaments large enough to be visible as spikes within 1 h, which indicates a reduction of the critical concentration for actin assembly through the stabilizing effect of MiuA.

The apparent diffusion constants and apparent N have been obtained from a one-component fit of the diffusion part of the autocorrelation function. However, in solution, there is always a mixture of growing and shrinking oligomers of different sizes and monomers. Therefore, the thus obtained apparent values are no absolute values, but provide a more qualitative indication of the occurrence of small oligomers in solution. Using these values, similar measurements could be compared and the influence of MiuA on the formation of oligomers that were small enough to not lead to visible spikes in the countrate could be visualized.

The obtained numbers of molecules in the observation volume N are lower than expected for the measured concentrations. For the measurement of 10 nM actin-atto488, an N of 0.6 with a brightness of 27 kHz has been fitted by a one-component fit. For the higher concentrations, the brightness increased to about 60 kHz. The obtained values of N are therefore comparable between measurements of the same concentration, but are no absolute or globally comparable values.

To have a reference point of the diffusion constant of a monomer, 10 nM actin in G-buffer was measured. However, the resulting autocorrelation function could be fitted only with nonuniformly distributed residuals with a one-component fit. However, the value of the diffusion constant from

the one-component fit was similar to the expected value (He and Niemeyer, 2003). The fit was better for the higher concentrations. A reason could be that, despite the low concentration and nonpolymerizing conditions, small, unstable oligomers could form. The formation of small oligomers, like dimers and trimers, have a larger effect on the relative change in hydrodynamic radius than the attachment of an additional monomer to an already existing filament of several monomers, which in turn affects the diffusion behavior more. Additionally, when larger oligomers exist in solution, the probability that several dye molecules are contained in the oligomers is increased, which increases the effect of the larger oligomers on the autocorrelation function. Therefore, despite being the more complex system, a one-component fit was possible for higher concentrations, as also observed in Chakraborty et al., 2012. Thereby, the fit range reached from 1 μs to 1 ms for actin concentrations of 100 to 500 nM and a possible triplet state of the dye was fitted globally for each concentration. For 50 nM, the fit range had to be cut off at 100 μs to obtain a fit result with uniformly distributed residuals over the entire fit range.

The influence of a change in volume due to oligomerization on the diffusion constant is not very pronounced, as can be seen in the Stokes-Einstein equation:

$$D = \frac{k_B T}{6\pi\eta r} \tag{5.1}$$

where k_B is the Boltzmann constant, T the temperature, η the viscosity of the medium and r the hydrodynamic radius, which is proportional to the cubic root of the volume. Thus, a change in D during oligomerization results in

$$\frac{D_1}{D_n} = n^{1/3} \tag{5.2}$$

with D_n the diffusion constant of the oligomer with n monomers and D_1 the diffusion constant of the monomer. This relationship assumes a spherical shape of the monomers and oligomers with a constant volume per monomer. However, the influence of the molecular shape was found to be minor for another filament-forming protein, the AAA+ ATPase Rubisco activase (Chakraborty et al., 2012). D_1 could not be determined directly. If one assumes, however, a diffusion constant of 69 $\mu m^2/s$ as the highest diffusion constant obtained in these measurements, one can estimate an apparent

oligomer size for the influence of MiuA. The assumed diffusion constant is similar to the calculated diffusion constant of ovalbumin (70 $\mu m^2/s$), which has a similar size (He and Niemeyer, 2003). For 100 nM actin with MiuA, an apparent diffusion constant of 42 $\mu m^2/s$ is obtained, which would correspond to oligomers of 4 to 5 monomers. However, this is a rough estimate and describes only the oligomers small enough to be accounted for in the autocorrelation function, where spikes were excluded. Therefore, much bigger oligomers exist in solution, as can be seen in the spike analysis.

For the study of protein oligomers using FCS, the number and brightness (N & B) analysis is a useful tool to analyze the average oligomer size (Digman et al., 2008). This works well when the brightness of the purely monomeric sample can be obtained, like, for example, for the study of GFP oligomers (Gambin et al., 2016). However, for more complicated systems containing many different, dynamic oligomers, the distribution is difficult to fit and the interpretation of the oligomer size gets unreliable (Gambin et al., 2016). For actin, the difficulty was to measure a purely monomeric sample, as a very low concentration under non-polymerizing conditions still contained oligomers.

A further method often used to study oligomerization in FCS is the photon counting histogram (PCH). However, the same problem occurs as for the N & B analysis: the brightness of the monomeric species is difficult to obtain in the case of actin. Furthermore, the multitude of different oligomer sizes during actin assembly complicates the analysis. PCH histograms for the measured data showed the existence of larger oligomeric species, as did the spike analysis.

Finally, Nikolaus Naredi-Rainer used fluorescence cross-correlation (FCCS) to study actin oligomerization with confocal microscopy (Naredi-Rainer, 2011). The occurrence of a spike in both channels indicates an oligomer constisting of multiple monomers labeled with different dyes.

To summarize, FCS has the advantage of being a solution-based method, i.e. there are no surface or geometry effects as in the use of ZMW. However, highly dynamic systems with oligomers of different, changing sizes become a challenge for a quantitative analysis of the number of monomers and the diffusion constant. Furthermore, for the study of actin assembly, high concentrations are needed to overcome the critical concentration of 200 nM or even 600 nM for the pointed end, whereas typical FCS experiments are performed in the pM to low nM range. Still, using the spike analysis, aggregation of proteins

could be studied using confocal microscopy for oligomers large enough to appear as spikes in the countrate.

Chapter 6

Summary

In this thesis, I applied single-molecule methods for the elucidation of the first steps in protein assembly. Zero-mode waveguides (ZMW), TIRFM and confocal microscopy have been applied to visualize the first steps of actin nucleation. For these measurements, a set-up was built for imaging in TIRF mode as well as in widefield mode for the measurements in ZMW. To be able to measure thousands of apertures at the same time, EMCCD cameras with a large chip were implemented.

Using this set-up, the actin nucleation process was studied with different nucleator proteins as well as under the influence of two different actin binding drugs. For the analysis of single-molecule time traces of protein polymerization, I developed new analysis methods: the visitation analysis and the average rate analysis. These methods could distill much information that remained hidden using a classical dwell-time analysis. Furthermore, I tested the visitation analysis, the average rate analysis and the dwell-time analysis for their robustness towards typical challenges in real data, i.e. the signal-to-noise ratio, the sampling time with respect to the association rates, the photobleaching of fluorophores and the labeling efficiency of the proteins of interest. These results are a useful guide for the planning and interpretation of single-molecule methods for protein assembly.

Using the developed analysis methods on actin growing on different nucleator proteins, a number of interesting results have been obtained. ZMW measurements of actin assembling on gelsolin revealed the existence of two populations, one that elongated into stable filaments and one that did not. The difference between the populations could be attributed to two different dimer formations assembling on gelsolin. In contrast, actin assembling on cappuccino showed unhindered growth with a single association and a single

dissociation rate. ZMW and TIRFM measurements of actin assembling on spire-ABCD provided further evidence that the spire monomer alone is not a sufficient nucleator, but binds to and stabilizes preformed oligomers in solution.

The use of Latrunculin A, an actin binding drug that inhibits the flattening of the actin monomer occurring during polymerization, revealed that this flattening is required for the formation of stable oligomers at a very early stage during actin assembly. Furthermore, it is required to stabilize the nascent filament. These results hint towards a rapid ATP hydrolysis, which is coupled to flattening, at an early stage in actin nucleation.

Confocal microscopy measurements of actin polymerizing in the presence of Miuraenamide A have been analyzed using a spike analysis and the autocorrelation function of the fluorescence intensity fluctuations. The results showed that MiuA stabilizes oligomers and small filaments and lowers the critical concentration of actin polymerization. A part of these results have been published in Wang et al., 2019. Futhermore, for the development of a method for the quantification of protein oligomerization using anisotropy measurements in confocal microscopy, TIRF measurements and analysis of green fluorescent protein (GFP) oligomerization have been performed and published in Heckmeier et al., 2020.

ZMW can be used to measure biological interactions at the single molecule level at biologically relevant concentrations. Together with the developed analysis tools, ZMW, TIRFM and other single molecule methods such as iScat (Andrecka et al., 2016) will help to elucidate the first steps of the assembly process of a multitude of proteins.

List of Abbreviations

ACF	**A**uto**C**orrelation **F**unction
APD	**A**valanche **P**hoto **D**iodes
a.u.	**a**rbitrary **u**nits
DNA	**D**eoxy **R**ibonucleic **A**cid
EMCCD	**E**lectron-**M**ultiplied **C**harge-**C**oupled **D**evice
FCS	**F**luorescence **C**orrelation **S**pectroscopy
GFP	**G**reen **F**luorescent **P**rotein
LatA	**L**atrunculin **A**
LE	**L**abeling **E**fficiency
MiuA	**M**iuraenamide **A**
NA	**N**umerical **A**perture
N & B	**N**umber and **B**rightness
PBS	**P**hosphate **B**uffered **S**aline
PCH	**P**hoton **C**ounting **H**istogram
PEG	**P**oly**E**thylene **G**lycole
PVPA	**P**oly**V**inyl **P**hosphonic **A**cid
RSS	**R**esidual **S**um of **S**quares
SNR	**S**ignal-to-**N**oise **R**atio
TIRFM	**T**otal **I**nternal **R**eflection **M**icroscopy
sCMOS	**s**cientific **C**omplementary **M**etal–**O**xide–**S**emiconductor
WH2	**W**iskott-Aldrich **H**omology domain 2
WASP	**W**iskott- **A**ldrich **S**yndrome **P**rotein
ZMW	**Z**ero-**M**ode **W**aveguides

Bibliography

Aggarwal, T. et al. (2012). "Detection of Steps in Single Molecule Data". In: *Cellular and molecular bioengineering* 5.1, pp. 14–31.

Aitken, C., R. Marshall, and J. Puglisi (2008). "An Oxygen Scavenging System for Improvement of Dye Stability in Single-Molecule Fluorescence Experiments". In: *Biophysical Journal* 94, pp. 1826–1835.

Andrecka, J. et al. (2016). "Label-Free Imaging of Microtubules with Sub-Nm Precision Using Interferometric Scattering Microscopy". In: *Biophys J* 110.1, pp. 214–217.

Arosio, P., T. P. J. Knowles, and S. Linse (2015). "On the lag phase in amyloid fibril formation". In: *Phys. Chem. Chem. Phys.* 17 (12), pp. 7606–7618.

Baum, B. and P. Kunda (2005). "Actin Nucleation: Spire - Actin Nucleator in a Class of Its Own". In: *Current Biology* 15.8, R305–R308.

Blanchoin, L. and T. D. Pollard (2002). "Hydrolysis of ATP by Polymerized Actin Depends on the Bound Divalent Cation but Not Profilin". In: *Biochemistry* 41.2, pp. 597–602.

Blanchoin, L. et al. (2014). "Actin dynamics, architecture, and mechanics in cell motility". In: *Physiol Rev* 94.1, pp. 235–263.

Bor, B. et al. (2012). "Autoinhibition of the formin Cappuccino in the absence of canonical autoinhibitory domains". In: *Mol Biol Cell* 23.19, pp. 3801–3813.

Brangbour, C. et al. (2011). "Force-velocity measurements of a few growing actin filaments". In: *PLoS Biol* 9.4, e1000613.

Bryan, J. (1988). "Gelsolin has three actin-binding sites". In: *The Journal of Cell Biology* 106, pp. 1553–1562.

Bryan, J. and M. Kurth (1984). "Actin-gelsolin interactions. Evidence for two actin-binding sites." In: *Journal of Biological Chemistry* 259.12, pp. 7480–7487.

Bubb, M. R. et al. (2002). "Polylysine induces an antiparallel actin dimer that nucleates filament assembly: crystal structure at 3.5-A resolution". In: *J Biol Chem* 277.23, pp. 20999–1006.

Buell, A. K. et al. (2014). "Solution conditions determine the relative importance of nucleation and growth processes in alpha-synuclein aggregation". In: 111.21, pp. 7671–7676.

Bugyi, B. and M.-F. Carlier (2010). "Control of Actin Filament Treadmilling in Cell Motility". In: *Annual Review of Biophysics* 39.1, pp. 449–470.

Burtnick, L. et al. (1997). "The Crystal Structure of plasma gelsolin: Implications for actin severing, capping, and nucleation". In: *Cell* 90, pp. 661–670.

Burtnick, L. et al. (2004). "Structure of the N-terminal half of gelsolin bound to actin: roles in severing, apoptosis and FAF". In: *EMBO* 23, pp. 2713–2722.

Campellone, K. G. and M. D. Welch (2010). "A Nucleator Arms Race: Cellular Control of Actin Assembly". In: *Nat Rev Mol Cell Biol* 11.4, pp. 237–251.

Chakraborty, M. et al. (2012). "Protein Oligomerization Monitored by Fluorescence Fluctuation Spectroscopy: Self-Assembly of Rubisco Activase". In: *Biophys J* 103.5, pp. 949–958.

Chiti, F. and C. M. Dobson (2006). "Protein Misfolding, Functional Amyloid, and Human Disease". In: *Annual Review of Biochemistry* 75.1, pp. 333–366.

Choe, H. et al. (2002). "The calcium activation of gelsolin: insights from the 3A structure of the G4-G6/actin complex". In: *J Mol Biol* 324.4, pp. 691–702.

Christensen, S. M. et al. (2016). "Monitoring the Waiting Time Sequence of Single Ras GTPase Activation Events Using Liposome Functionalized Zero-Mode Waveguides". In: *Nano Letters* 16.4, pp. 2890–2895.

Cohen, S. I. et al. (2012). "From Macroscopic Measurements to Microscopic Mechanisms of Protein Aggregation". In: *J Mol Biol* 421.2-3, pp. 160–171.

Cooper, J. A., S. B. Walker, and T. D. Pollard (1983). "Pyrene Actin: Documentation of the Validity of a Sensitive Assay for Actin Polymerization". In: *Journal of Muscle Research and Cell Motility* 4.2, pp. 253–262.

Cordes, T., J. Vogelsang, and P. Tinnefeld (2009). "On the Mechanism of Trolox as Antiblinking and Antibleaching Reagent". In: *Journal of the American Chemical Society* 131.14, pp. 5018–5019.

Coué, M. and E. D. Korn (1985). "Interaction of plasma gelsolin with G-actin and F-actin in the presence and absence of calcium ions". In: *Journal of Biological Chemistry* 260.28, pp. 15033–15041.

– (1986). "ATP hydrolysis by the gelsolin-actin complex and at the pointed ends of gelsolin-capped filaments". In: *Journal of Biological Chemistry* 261.4, pp. 1588–1593.

Coué, M. et al. (1987). "Inhibition of actin polymerization by latrunculin A". In: *FEBS letters* 213.2, pp. 316–318.

Cremades, N. et al. (2012). "Direct Observation of the Interconversion of Normal and Toxic Forms of Alpha-Synuclein". In: *Cell* 149.5, pp. 1048–1059.

Crevenna, A. H. et al. (2013). "Electrostatics control actin filament nucleation and elongation kinetics". In: *J Biol Chem* 288.17, pp. 12102–12113.

Crevenna, A. H. et al. (2015). "Side-binding proteins modulate actin filament dynamics". In: *Elife* 4, e04599.

De, S. et al. (2019). "Different Soluble Aggregates of Abeta42 Can Give Rise to Cellular Toxicity through Different Mechanisms". In: *Nat Commun* 10.1, p. 1541.

Dick, M. S. et al. (2016). "Asc Filament Formation Serves as a Signal Amplification Mechanism for Inflammasomes". In: *Nat Commun* 7, p. 11929.

Digman, M. A. et al. (2008). "Mapping the Number of Molecules and Brightness in the Laser Scanning Microscope". In: *Biophysical Journal* 94.6, pp. 2320–2332.

Ditsch, A. and A. Wegner (1994). "Nucleation of Actin Polymerization by Gelsolin". In: *European Journal of Biochemistry* 224.1, pp. 223–227.

Doi, Y. (1992). "Interaction of gelsolin with covalently cross-linked actin dimer". In: *Biochemistry* 31.41, pp. 10061–10069.

Dominguez, R. (2009). "Actin filament nucleation and elongation factors – structure-function relationships". In: *Critical reviews in biochemistry and molecular biology* 44.6, pp. 351–366.

– (2016). "The WH2 Domain and Actin Nucleation: Necessary but Insufficient". In: *Trends Biochem Sci* 41.6, pp. 478–490.

Dominguez, R. and K. C. Holmes (2011). "Actin Structure and Function". In: *Annual review of biophysics* 40, pp. 169–186.

Ducka, A. M. et al. (2010). "Structures of actin-bound Wiskott-Aldrich syndrome protein homology 2 (WH2) domains of Spire and the implication for filament nucleation". In: *Proc Natl Acad Sci U S A* 107.26, pp. 11757–11762.

Floyd, D. L., S. C. Harrison, and A. M. van Oijen (2010). "Analysis of Kinetic Intermediates in Single-Particle Dwell-Time Distributions". In: *Biophysical Journal* 99.2, pp. 360 –366.

Füreder-Kitzmüller, E. et al. (2005). "Non-exponential bleaching of single bioconjugated Cy5 molecules". In: *Chemical Physics Letters* 404.1, pp. 13 –18.

Frieden, C. (1983). "Polymerization of actin: mechanism of the Mg2+-induced process at pH 8 and 20 degrees C". In: *Proc Natl Acad Sci U S A* 80.21, pp. 6513–6517.

Fujii, T. et al. (2010). "Direct visualization of secondary structures of F-actin by electron cryomicroscopy". In: *Nature* 467.7316, pp. 724–728.

Gambin, Y. et al. (2016). "Confocal Spectroscopy to Study Dimerization, Oligomerization and Aggregation of Proteins: A Practical Guide". In: *International Journal of Molecular Sciences* 17.5.

Garoli, D. et al. (2019). "Plasmonic Nanopores for Single-Molecule Detection and Manipulation: Toward Sequencing Applications". In: *Nano Letters* 19.11, pp. 7553–7562.

Giganti, A and E. Friederich (2003). "The actin cytoskeleton as a therapeutic target: state of the art and future directions". In: *JProg Cell Cycle Res.* 5, pp. 511–525.

Graceffa, P. and R. Dominguez (2003). "Crystal Structure of Monomeric Actin in the ATP State: structural basis of nucleotide dependent actin dynamics". In: *Journal of Biological Chemistry* 278, pp. 34172–34180.

Graceffa, P., E. Lee, and W. F. Stafford (2013). "Disulfide cross-linked antiparallel actin dimer". In: *Biochemistry* 52.6, pp. 1082–1088.

Grazi, E., A. Ferri, and S. Cino (1983). "The Polymerization of Actin - a Study of the Nucleation Reaction". In: 213.3, 727–732.

Grintsevich, E. E. et al. (2010). "Antiparallel dimer and actin assembly". In: *Biochemistry* 49.18, pp. 3919–3927.

Guhathakurta, P. et al. (2020). "Actin-binding compounds, previously discovered by FRET-based high-throughput screening, differentially affect skeletal and cardiac muscle". In: *Journal of Biological Chemistry* 295.41, pp. 14100–14110.

He, L. and B. Niemeyer (2003). "A Novel Correlation for Protein Diffusion Coefficients Based on Molecular Weight and Radius of Gyration". In: *Biotechnology Progress* 19.2, pp. 544–548.

Heckmeier, P. J. et al. (2020). "Determining the Stoichiometry of Small Protein Oligomers Using Steady-State Fluorescence Anisotropy". In: *Biophysical Journal* 119.1, pp. 99 –114.

Herschel, J. F. W. (1845). "On a case of superficial colour presented by a homogeneous liquid internally colourless". In: *Philos Trans R Soc London* 135, 143–145.

Hesterkamp, T., A. G. Weeds, and H. G. Mannherz (1993). "The actin monomers in the ternary gelsolin: 2 actin complex are in an antiparallel orientation". In: *European Journal of Biochemistry* 218.2, pp. 507–513.

Horrocks, M. H. et al. (2015). "Fast Flow Microfluidics and Single-Molecule Fluorescence for the Rapid Characterization of Alpha-Synuclein Oligomers". In: *Anal Chem* 87.17, pp. 8818–8826.

Horrocks, M. H. et al. (2016). "Single-Molecule Imaging of Individual Amyloid Protein Aggregates in Human Biofluids". In: *ACS Chem Neurosci* 7.3, pp. 399–406.

Hortschansky, P. et al. (2005). "The aggregation kinetics of Alzheimer's beta-amyloid peptide is controlled by stochastic nucleation". In: *Protein Science* 14.7, pp. 1753–1759.

Howard, J. (2001). *Mechanics of Motor Proteins and the Cytoskeleton*. Sinauer Associates, Publishers. ISBN: 9780878933341.

Hoyer, M. et al. (2018). "Dimer arrangement and monomer flattening determine actin filament formation". In: *bioRxiv*.

Hoyer, Maria (2014). "Statistical Kinetics of Actin Filament Nucleation studied with Zero-Mode Waveguides". MA thesis. Ludwigs-Maximilians-Universität München.

Huxley, H.E. (1963). "Electron microscope studies on the structure of natural and synthetic protein filaments from striated muscle". In: *Journal of Molecular Biology* 7.3, 281–IN30.

Jamora, C. and E. Fuchs (2002). "Intercellular Adhesion, Signalling and the Cytoskeleton". In: *Nature Cell Biology* 4.4, E101–E108.

Johnson, P. (1976). "Thermodynamics of the Polymerization of Protein". In: *Biochemical Society Transactions* 4.6, pp. 1168–1168.

Kabsch, W. et al. (1990). "Atomic structure of the actin:DNase I complex". In: *Nature* 347, pp. 37–44.

Kasai, M., S. Asakura, and F. Oosawa (1962). "The cooperative nature of G-F transformation of actin". In: *Biochimica et Biophysica Acta* 57.1, pp. 22–31.

Kasha, M. (1950). "Characterization of electronic transitions in complex molecules". In: *Disc Faraday Soc* 9, 14–19.

Kelly, J. (1998). "The alternative conformations of amyloidogenic proteins and their multi-step assembly pathways". In: *Current Opinion in Structural Biology* 8.1, pp. 101 –106.

Khaitlina, S. and Hinssen. H. (2002). "Ca-dependent binding of actin to gelsolin". In: *FEBS Letters* 521, pp. 14 –18.

Khaitlina, S. and H. Hinssen (1997). "Conformational changes in actin induced by its interaction with gelsolin". In: *Biophysical Journal* 73, pp. 929–937.

Khaitlina, S., M. Walloscheck, and H. Hinssen (2004). "Calcium-Induced Conformational Changes in the C-Terminal Half of Gelsolin Stabilize Its Interaction with the Actin Monomer". In: *Biochemistry* 43, pp. 12838–12845.

Kim, S. et al. (2007). "l1 Trend Filtering". In: *SIAM Reviews* 51, pp. 339–360.

Kinosian, H. et al. (1998). "Ca2+ Regulation of Gelsolin Activity: Binding and Severing of F-actin". In: *Biophys J.* 75, pp. 3101–3109.

Kirkitadze, M. D., M. M. Condron, and D. B. Teplow (2001). "Identification and Characterization of Key Kinetic Intermediates in Amyloid Beta-Protein Fibrillogenesis". In: *J Mol Biol* 312.5, pp. 1103–1119.

Knowles, T. P., M. Vendruscolo, and C. M. Dobson (2014). "The Amyloid State and Its Association with Protein Misfolding Diseases". In: *Nat Rev Mol Cell Biol* 15.6, pp. 384–396.

Knowles, T. P. J. et al. (2009). "An Analytical Solution to the Kinetics of Breakable Filament Assembly". In: *Science* 326.5959, pp. 1533–1537.

Korlach, J. et al. (2008). "Selective aluminum passivation for targeted immobilization of single DNA polymerase molecules in zero-mode waveguide nanostructures". In: *Proceedings of the National Academy of Sciences* 105, pp. 1176–1181.

Kuhn, J. R. and T. D. Pollard (2005). "Real-time measurements of actin filament polymerization by total internal reflection fluorescence microscopy". In: *Biophys J* 88.2, pp. 1387–1402.

Kuzyk, A., K. T. Laitinen, and P. Törmä (2009). "DNA origami as a nanoscale template for protein assembly". In: *Nanotechnology* 20.23, p. 235305.

Lakowicz, J. R. (2006). *Principles of Fluorescence Spectroscopy*. Springer, Boston, MA. ISBN: 978-0-387-46312-4.

Lambert, C. R. and I. E. Kochevar (1997). "Electron Transfer Quenching of the Rose Bengal Triplet State". In: *Photochemistry and Photobiology* 66.1, pp. 15–25.

Lavergne, T. et al. (2016). "FRET Characterization of Complex Conformational Changes in a Large 16S Ribosomal RNA Fragment Site-Specifically Labeled Using Unnatural Base Pairs". In: *ACS Chemical Biology* 11.5, pp. 1347–1353.

Lee, S. H. and R. Dominguez (2010). "Regulation of Actin Cytoskeleton Dynamics in Cells". In: *Molecules and cells* 29.4, pp. 311–325.

Levene, M. J. et al. (2003). "Zero-Mode Waveguides for Single-Molecule Analysis at High Concentrations". In: *Science* 299, pp. 682–686.

Liang, Y., D. G. Lynn, and K. M. Berland (2009). "Direct Observation of Nucleation and Growth in Amyloid Self-Assembly". In: *JACS*.

Lin, K., M. Mejillano, and H. Yin (2000). "Ca2+ regulation of gelsolin by its carboxyl-terminal tail". In: *Journal of Biological Chemistry*.

Lu, A. et al. (2014). "Unified Polymerization Mechanism for the Assembly of Asc-Dependent Inflammasomes". In: *Cell* 156.6, pp. 1193–1206.

M., Marvin (1961). "Microscopy Apparatus". In: *US Patent* 3,013,467.

Machesky, L. M. and R. H. Insall (1999). "Signaling to Actin Dynamics". In: *The Journal of cell biology* 146.2, pp. 267–272.

Manseau, L., J. Calley, and H. Phan (1996). "Profilin Is Required for Posterior Patterning of the Drosophila Oocyte". In: *Development* 122.7, pp. 2109–2116.

Manseau, L. J. and T. Schuepbach (1989). "cappuccino and spire: two unique maternal-effect loci required for both the anteroposterior and dorsoventral patterns of the Drosophila embryo." In: *Genes and Development* 3.9, pp. 1437–1452.

McCullagh, M., M. G. Saunders, and G. A. Voth (2014). "Unraveling the Mystery of ATP Hydrolysis in Actin Filaments". In: *Journal of the American Chemical Society* 136.37, pp. 13053–13058.

Meisl, G. et al. (2014). "Differences in nucleation behavior underlie the contrasting aggregation kinetics of the Abeta40 and Abetea42 peptides". In: 111.26, pp. 9384–9389.

Meisl, G. et al. (2016). "Molecular Mechanisms of Protein Aggregation from Global Fitting of Kinetic Models". In: *Nat Protoc* 11.2, pp. 252–272.

Michaels, T. C. et al. (2017). "Physical Principles of Filamentous Protein Self-Assembly Kinetics". In: *J Phys Condens Matter* 29.15, p. 153002.

Millonig, R., H. Salvo, and U. Aebi (1988). "Probing actin polymerization by intermolecular cross-linking." In: *Journal of Cell Biology* 106.3, pp. 785–796.

Mockrin, S. C. and E. D. Korn (1983). "Kinetics of polymerization and ATP hydrolysis by covalently crosslinked actin dimer." In: *Journal of Biological Chemistry* 258.5, pp. 3215–3221.

Montaville, P. et al. (2014). "Spire and Formin 2 Synergize and Antagonize in Regulating Actin Assembly in Meiosis by a Ping-Pong Mechanism". In: *PLOS Biology* 12.2, pp. 1–20.

Moran-Mirabal, J. and H. Craighead (2008). "Zero-mode waveguides: Sub-wavelength nanostructures for single molecule studies at high concentrations". In: *Methods* 46, pp. 11–17.

Morton, W. M., K. R. Ayscough, and P. J. McLaughlin (2000). "Latrunculin alters the actin-monomer subunit interface to prevent polymerization". In: *Nat Cell Biol* 2.6, pp. 376–378.

Nag, S. et al. (2013). "Gelsolin: The tail of a molecular gymnast". In: *Cytoskeleton* 70, pp. 360–384.

Naredi-Rainer, Nikolaus (2011). "Advanced Confocal Microscopy: From Setups To Applications". MA thesis. Ludwigs-Maximilians-Universität München.

Narita, A., T. Oda, and Y. Maeda (2011). "Structural basis for the slow dynamics of the actin filament pointed end". In: *Embo j* 30.7, pp. 1230–1237.

Oda, T. et al. (2009). "The nature of the globular- to fibrous-actin transition". In: *Nature* 457.7228, pp. 441–445.

Orlova, A., E. Prochniewicz, and E. H. Egelman (1995). "Structural Dynamics of F-actin: II. Cooperativity in Structural Transitions". In: *J. Mol. Biol.* 245, 598–607.

Otterbein, L. R., P. Graceffa, and R. Dominguez (2001). "The crystal structure of uncomplexed actin in the ADP state". In: *Science* 293.5530, pp. 708–711.

Paunola, E., P. K. Mattila, and P. Lappalainen (2002). "WH2 domain: a small, versatile adapter for actin monomers". In: *FEBS Letters* 513.1, pp. 92–97.

Pettersen, E. F. et al. (2004). "UCSF Chimera - a visualization system for exploratory research and analysis". In: *J Comput Chem* 25.13, pp. 1605–1612.

Pfaendtner, J. et al. (2009). "Nucleotide-dependent conformational states of actin". In: *PNAS* 106, pp. 12723–12728.

Pollard, T. D. (1986). "Rate Constants for the Reactions of ATP- and ADP-Actin with the Ends of Actin Filaments". In:

Pollard, T. D. and G. G. Borisy (2003). "Cellular Motility Driven by Assembly and Disassembly of Actin Filaments". In: *Cell* 112.4, pp. 453–465.

Pollard, T. D. and M. S. Mooseker (1981). "Direct measurement of actin polymerization rate constants by electron microscopy of actin filaments nucleated by isolated microvillus cores". In: *J Cell Biol* 88.3, pp. 654–659.

Pope, B., J. Gooch, and A. Weeds (1997). "Probing the Effects of Calcium on Gelsolin". In: *Biochemistry* 36, pp. 15848–15855.

Pospich, S. et al. (2017). "Near-atomic structure of jasplakinolide-stabilized malaria parasite F-actin reveals the structural basis of filament instability". In: *Proceedings of the National Academy of Sciences* 114.40, pp. 10636–10641.

Powers, E. T. and D. L. Powers (2006). "The Kinetics of Nucleated Polymerizations at High Concentrations: Amyloid Fibril Formation near and above the "Supercritical Concentration"". In: *Biophys J* 91.1, pp. 122–132.

Qu, Z. et al. (2015). "Distinct actin oligomers modulate differently the activity of actin nucleators". In: *FEBS Journal* 282.19, pp. 3824–3840.

Qualmann, B. and M. M. Kessels (2009). "New Players in Actin Polymerization - WH2-Domain-Containing Actin Nucleators". In: *Trends Cell Biol* 19.6, pp. 276–285.

Quinlan, M. E. (2013). "Direct interaction between two actin nucleators is required in Drosophila oogenesis". In: *Development* 140.21, pp. 4417–4425.

Quinlan, M. E. et al. (2005). "Drosophila Spire Is an Actin Nucleation Factor". In: *Nature* 433.7024, pp. 382–388.

Quinlan, M. E. et al. (2007). "Regulatory interactions between two actin nucleators, Spire and Cappuccino". In: *J Cell Biol* 179.1, pp. 117–128.

Ramachandran, G. et al. (2014). "Resonance Raman Spectroscopic Measurements Delineate the Structural Changes That Occur During Tau Fibril Formation". In: *Biochemistry* 53.41, pp. 6550–6565.

Renault, L., B. Bugyi, and M.-F. Carlier (2008). "Spire and Cordon-bleu: multifunctional regulators of actin dynamics". In: *Trends in Cell Biology* 18, pp. 494–504.

Rennebaum, S. and A. Caflisch (2012). "Inhibition of interdomain motion in g-actin by the natural product latrunculin: A molecular dynamics study". In: *Proteins: Structure, Function, and Bioinformatics* 80, pp. 1998–2008.

Rosales-Nieves, A. E. et al. (2006). "Coordination of microtubule and microfilament dynamics by Drosophila Rho1, Spire and Cappuccino". In: *Nat Cell Biol* 8.4, pp. 367–376.

Rould, M. et al. (2006). "Crystal Structures of Expressed Non-polymerizable Monomeric Actin in the ADP and ATP States". In: *Journal of Biological Chemistry* 281, pp. 31909–31919.

Sabaté, R., M. Gallardo, and J. Estelrich (2005). "Temperature dependence of the nucleation constant rate in beta amyloid fibrillogenesis". In: *International Journal of Biological Macromolecules* 35.1, pp. 9–13.

Samiee, K. et al. (2005). "Lambda-Repressor Oligomerization Kinetics at High Concentrations Using Fluorescence Correlation Spectroscopy in Zero-Mode Waveguides". In: *Biophysical Journal* 88, pp. 2145–2153.

Schmoller, K. M. et al. (2011). "Fragmentation Is Crucial for the Steady-State Dynamics of Actin Filaments". In: *Biophysical journal* 101.4, pp. 803–808.

Schoepper, B. and A. Wegner (1991). "Rate constants and equilibrium constants for binding of actin to the 1:1 gelsolin-actin complex". In: *European journal of biochemistry / FEBS* 202.3, pp. 1127–1131.

Schrimpf, W. et al. (2018). "Pam: A Framework for Integrated Analysis of Imaging, Single-Molecule, and Ensemble Fluorescence Data". In: *Biophysical Journal* 114.7, pp. 1518–1528.

Selve, N. and A. Wegner (1987). "pH-dependent rate of formation of the gelsolin-actin complex from gelsolin and monomeric actin". In: *European journal of biochemistry / FEBS* 168.1, pp. 111–115.

Sept, D. and J. A. McCammon (2001). "Thermodynamics and kinetics of actin filament nucleation". In: *Biophysical journal* 81.2, pp. 667–674.

Shammas, S. L. et al. (2015). "A Mechanistic Model of Tau Amyloid Aggregation Based on Direct Observation of Oligomers". In: *Nat Commun* 6, p. 7025.

Spector, I. et al. (1983). "Latrunculins: novel marine toxins that disrupt microfilament organization in cultured cells". In: *Science* 4, pp. 493–495.

Stokes, G. G. (1852). "On the change of refrangibility of light". In: *Phil. Trans. R. Soc.* 142, 463–562.

Szoszkiewicz, R. et al. (2008). "Dwell Time Analysis of a Single-Molecule Mechanochemical Reaction". In: *Langmuir* 24.4, pp. 1356–1364.

Toseland, C. P. (2013). "Fluorescent Labeling and Modification of Proteins". In: *Journal of Chemical Biology* 6.3, pp. 85–95.

Tseng, Q. et al. (2011). "A new micropatterning method of soft substrates reveals that different tumorigenic signals can promote or reduce cell contraction levels". In: *Lab Chip* 11 (13), pp. 2231–2240.

Uemura, S. et al. (2010). "Real-Time Trna Transit on Single Translating Ribosomes at Codon Resolution". In: *Nature* 464.7291, pp. 1012–1017.

Uratani, Y., S. Asakura, and K. Imahori (1972). "A Circular Dichroism Study of Salmonella Flagellin: Evidence for Conformational Change on Polymerization". In: *Journal of Molecular Biology* 67.1, pp. 85–98.

Vizcarra, C. L. et al. (2011). "Structure and function of the interacting domains of Spire and Fmn-family formins". In: *Proceedings of the National Academy of Sciences* 108.29, pp. 11884–11889.

Vorobiev, S. et al. (2003). "The structure of nonvertebrate actin: Implications for the ATP hydrolytic mechanism". In: *PNAS* 100, pp. 5760–5765.

Wang, S. et al. (2019). "Actin stabilizing compounds show specific biological effects due to their binding mode". In: *Scientific Reports* 9.9731.

Wegner, A. (1976). "HEAD TO TAIL POLYMERIZATION OF ACTIN". In: *Journal of molecular biology* 108, pp. 139–150.

– (1982). "Spontaneous fragmentation of actin filaments in physiological conditions". In: *Nature* 296.

Wegner, A. and P. Savko (1982). "Fragmentation of actin filaments". In: *Biochemistry* 21.8, pp. 1909–1913.

Wellington, A. et al. (1999). "Spire contains actin binding domains and is related to ascidian posterior end mark-5". In: *Development* 126.23, pp. 5267–5274.

Wieland, T., H. Faulstich, and L. Fiume (1978). "Amatoxins, Phallotoxins, Phallolysin, and Antamanide: The Biologically Active Components of Poisonous Amanita Mushroom". In: *CRC Critical Reviews in Biochemistry* 5.3, pp. 185–260.

Xu, Y. et al. (2004). "Crystal Structures of a Formin Homology-2 Domain Reveal a Tethered Dimer Architecture". In: *Cell* 116.5, pp. 711–723.

Xue, W.-F., S. W. Homans, and S. E. Radford (2008). "Systematic Analysis of Nucleation-Dependent Polymerization Reveals New Insights into the Mechanism of Amyloid Self-Assembly". In: *PNAS* 105, pp. 8926–8931.

Yin, H. and T. Stossel (1979). "Control of cytoplasmic actin gel-sol transformation by gelsolin, a calcium-dependent regulatory protein". In: *Nature* 281, pp. 583–586.

Yin, H. et al. (1981). "Calcium-control of Actin Filament Length". In: *J. Biol. Chem.* 256, pp. 9693–9697.

Young, G. et al. (2018). "Quantitative mass imaging of single biological macromolecules". In: *Science* 360.6387, pp. 423–427.

Zeth, K. et al. (2011). "Molecular basis of actin nucleation factor cooperativity: crystal structure of the Spir-1 kinase non-catalytic C-lobe domain (KIND)-formin-2 formin SPIR interaction motif (FSI) complex". In: *J Biol Chem.* 286.35, pp. 30732–30739.

Zhai, J. et al. (2012). "Characterization of Early Stage Intermediates in the Nucleation Phase of Abeta Aggregation". In: *Biochemistry* 51.6, pp. 1070–1078.

List of Figures

Acknowledgements

My thanks go to Don, without whom this thesis and the projects I worked on in the past years would not have been possible. Thank you for letting me work quite independently, following my interests. Also, thank you for always letting me attend meetings, seminars and conferences. Alvaro, thank you for getting me interested in actin dynamics and for many discussions and advice. My thanks go to all the students I worked with, namely Radek, Kherim, Markus and Ganesh. I enjoyed spending the time together in the lab and in front of the computer. Many thanks go also to Dr. Moritz Ehrl for keeping everything safely in order.

I thank Ellen, Ganesh, Sushi and Nader for creating a friendly work environment. Especially Ellen kept an open ear and a friendly voice during hard times.

Ein großer Dank geht an meine Eltern, die mich immer gefördert und gefordert haben. Ihr habt eine Umgebung geschaffen, in der ich geistig wachsen konnte, auf wissenschaftlicher und kultureller Ebene. Ihr und die erweiterte Familie haben uns die Möglichkeit gegeben, fest verankert in der europäischen Geschichte und Kultur einen kritischen Geist auszubilden.

David, ich danke dir von Herzen für jede gemeinsame Stunde. Du bist ein wundervoller Papa und ohne unser gutes Teamwork wäre diese Arbeit noch ein paar Jahre später fertig geworden. Sophia, ich bin unendlich dankbar für deine Existenz und dein freundliches und offenes Wesen. Du bist mit deiner unglaublichen Lern- und Übebereitschaft ein Vorbild für jeden Menschen, der etwas erreichen will.